TID-4500, UC-34
Physics

LAWRENCE LIVERMORE LABORATORY
University of California / Livermore, California / 94550

UCRL - 51207

ANOMALOUS RADIAL PLASMA LOSSES IN A Q-MACHINE WITH MIRROR MAGNETIC FIELDS

Richard Manor Searing

(Ph. D. Thesis)

MS. date: April 1972

CONTENTS

ANOMALOUS RADIAL PLASMA LOSSES IN A Q-MACHINE WITH MIRROR MAGNETIC FIELDS

ABSTRACT

Richard Manor Searing

Observations of a potassium ion plasma in a Q-machine with mirror magnetic fields located at the hotplates indicate that a strong localized radial electric field is formed at the hotplate edge, producing both ion confinement and a rotating high-velocity annulus in the column. The plasma equilibrium formed can be adequately described by an isothermal fluid model that includes ion viscosity and the inertia associated with the column rotation.

When the midplane magnetic field B_o on the axis exceeds 300 G for all measured densities, azimuthally propagating waves are observed which are located at the edge of the rotating annulus. These waves are identified as transverse velocity shear excited modes by comparison of the data with the predictions of the "velocity jet" model of Perkins and Jassby with regard to frequency, mode localization, and correlations between the perturbed density and potential. The modes contribute little to the radial losses that are due mainly to resistive diffusion.

When B_o is between 150 and 300 G, an azimuthally propagating $m=1$ mode appears when both the density and rotation speed exceed lower thresholds. Subsequent mode time-growth produces a large plasma loss and self-suppression as the

column plasma density is driven below the threshold level. Comparison of the m=1 mode stability, frequency, and growth-rate with the plasma model of Chu, Hendel, and Politzer indicate that the mode is probably an ion diamagnetic drift wave that is driven unstable by a combination of resistive and centrifugal effects. Detailed studies of the nonlinear development of the mode show that the plasma losses are primarily caused by $\underline{E} \times \underline{B}$ radial convection and are quantitatively consistent with the measured losses from the plasma column.

I. INTRODUCTION

In recent years, the study of enhanced or "anomalous" losses from magnetically confined plasmas has become an important topic of research.[1-18] The major reason for the interest, both theoretical and experimental, is the detrimental effect of enhanced plasma losses on the production and confinement of a thermonuclear plasma in large-scale, controlled fusion experiments.

Theoretical explanations have appeared in the literature for the correlation between self-excited plasma oscillations and enhanced losses,[1-5] but there are few experiments that clearly show this correlation.[7-12] Thomassen found a relation between certain self-excited waves and the enhanced plasma losses in a reflex arc (*P. I. G.*) discharge.[10] Morse followed the development of a flute instability in a hollow arc discharge for which enhanced plasma losses were observed to occur outside of a central inner core.[8] Yoshikawa, in a similar arc discharge, found enhanced plasma losses associated with the development of high frequency plasma turbulence.[6] In most of the experiments with arc discharges, the internal plasma parameters were not measurable with any degree of certainty, and the range of controllable external parameters was limited. Therefore, it has been difficult to convincingly demonstrate that plasma waves are directly responsible for the enhanced plasma losses in the experiments.

The presence of both high frequency turbulence and low frequency plasma waves led to confusion in the interpretation

of the results in arc-produced plasmas.[16, 17] The search for a more suitable plasma for the study of low frequency waves led to the development of methods for continuous, efficient, and relatively quiescent plasma generation.[19-23] One of the most useful and practical methods developed was the production of a low temperature (0.2 eV) plasma by the contact ionization of alkali metal atoms on hotplates in a "Q-machine".[22-23]

The Q-machine plasma is almost fully ionized at 0.2 eV with a time-average density between 10^{10} - $10^{12}/cm^3$, and does not generally indicate a turbulent frequency spectrum.[22] This method of plasma generation forces the internal plasma parameters to approximate closely those for thermal equilibrium with the hotplates and, when compared with arc discharges, the external parameters are controllable over a wide range. When typical experimental data of a low temperature cesium plasma are scaled to the energy and density required for a thermonuclear reaction, the enhanced plasma losses may pose serious design limitations on a practical fusion device.

The Q-machine plasma is, in principle, ideally suited for experimental measurements of the plasma equilibrium in various types of magnetic fields and of the propagation characteristics of low frequency plasma perturbations. Many papers on both of these topics have appeared in the literature,[24-32] but few experiments have attempted to correlate the plasma oscillations with enhanced plasma losses.[14-17] In those experiments that have been made, the results have been interpreted in different ways.

Two examples of different interpretations for the enhanced plasma losses are the experiments of Decker et al.[14] and those of Hendel et al.[15] Decker et al. measured an increase of nearly two orders-of-magnitude in the time-average plasma density whenever the plasma waves were suppressed, but they also observed only a small change in the radial plasma transport across the confining magnetic field. They attributed the enhanced losses to increased hotplate losses due to a change in the potential sheath at the hotplates.

In contrast, Hendel et al. showed that an increase in the radial diffusion rate across the magnetic field was correlated with the onset of collisional drift waves in the plasma. The waves were switched on and off without a change in the sheath conditions at the hotplates by changing the magnetic field; the ExB convection from thermal gradients at the hotplates was negligible.

The main difference between the two experiments was that the measurements of Decker et al. were made in the presence of ion-rich sheaths, while those of Hendel et al. were made with electron-rich sheaths at the hotplates. Large end losses of ions are possible for ion-rich sheaths, while an electron-rich sheath confines the ions in a potential well between the hotplates.

The present experiment is similar to that of Hendel et al. except that the waves are not collisional drift waves and the enhanced losses are due to convection instead of diffusion. A low β potassium ion plasma is magnetically confined in a mirror magnetic field. Measurements of time-average and

time-varying plasma parameters are made both with and without enhanced plasma losses. A clear correlation is established between the nonlinear time-growth of an m=1 azimuthally propagating plasma perturbation and the enhanced plasma losses across the magnetic field. Higher order (m=2 to 4) modes, which do not appear to be related to the m=1 mode, propagate with saturated amplitudes and do not produce any significant increase in the measured plasma losses. The time-growth of the m=1 mode amplitude appears to depend on density, magnetic field, and the $\underline{E}x\underline{B}$ rotation of the plasma column.

The remainder of the paper is organized as follows:

Chapter II describes the experimental apparatus and special measurement techniques. The calibration of the diagnostics is discussed together with the determination of several important constants in the experiment.

Chapter III discusses the type of plasma equilibrium for various experimental conditions. Measurements of the time-average density, floating potential, and radial electric field are studied as a function of column midplane radius, midplane magnetic field, and hotplate temperatures. Studies are made both with and without enhanced radial losses from the plasma.

Chapter IV discusses the types of plasma waves that propagate in the column. Two types of waves are observed, but only one type appears to be correlated with the enhanced plasma losses.

Chapter V studies the correlation between the modes of Chapter IV and enhanced radial plasma losses. The convective

losses due to the waves are evaluated and compared with the experimental losses from the plasma column. The nonlinear spacial distribution during various stages of the loss process are compared with earlier measurements. Measured loss-rates and the measured radial loss-flux are compared with the equation of continuity in the column.

Chapter VI discusses the results and presents the conclusions based on the results of all the measurements.

II. DESCRIPTION OF EXPERIMENT

A. Experimental Apparatus

Figure 1a shows a nearly-to-scale diagram of the experimental apparatus, and Fig. 1b indicates the schematic of the electrical power and control circuits. The vacuum vessel is a 0.5-in. thick Pyrex cylinder having a 12-in. inner diam, is 48-in. in length, and is sealed at each end by a 0.75-in. thick stainless steel flange. The base pressure in the vessel is maintained below 10^{-5} Torr at room temperature. Four diagnostic access ports, each 2-in. in diam, are located symmetrically at the vessel midplane. Access is also possible through vacuum ports in the stainless steel end flanges. To avoid potentially dangerous thermal stresses in the glass shell, the surface temperature is monitored at several points at the midplane and kept below an arbitrary level of 60°C (hot to the touch). Measurements of the temperature distribution at the midplane indicate a fairly uniform heating of the glass surface by radiation from the hotplates.

The plasma is produced by contact ionization of an atomic beam of potassium that is directed at one of two tungsten hotplates, each 2-in. in diam and 0.5-in. thick. The hotplates are separated by 100 cm along the vessel axis, and each hotplate is heated by electron bombardment to a temperature between 2000°K and 2700°K. The individual hotplate temperatures are measured with a calibrated optical pyrometer using the split mirror system shown in Fig. 2. The ionizer hotplate is kept at ground potential, while the second hotplate is insulated from

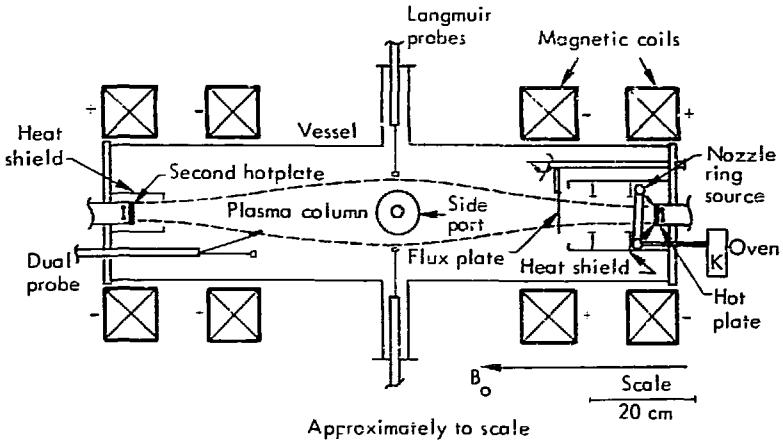

Fig. 1a. Experimental apparatus.

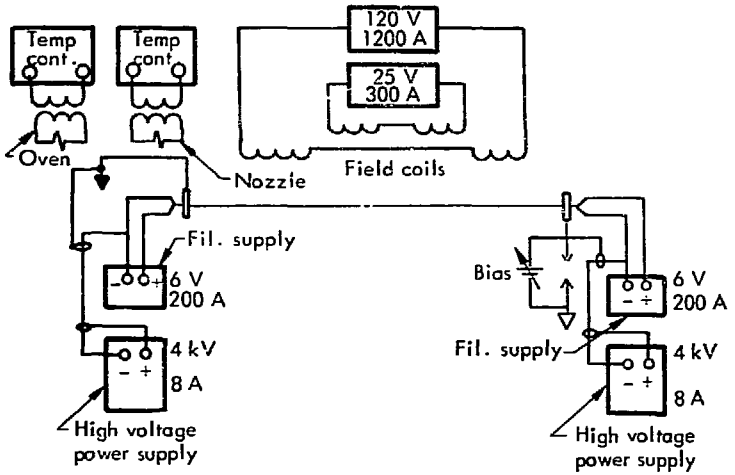

Fig. 1b. Electrical schematic of experiment.

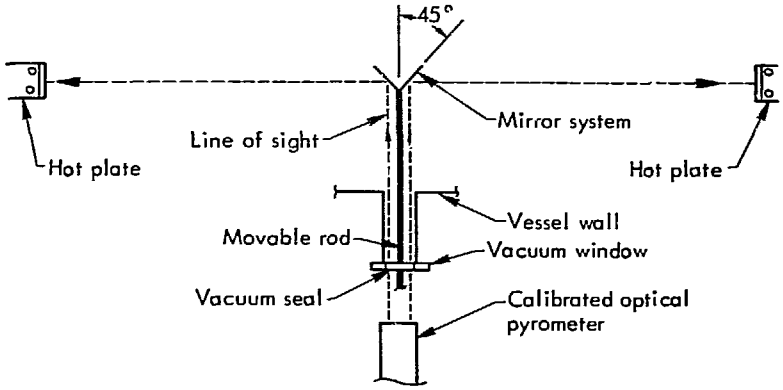

Fig. 2. Split mirror system for monitoring hotplate temperatures.

ground by a resistance greater than 120kΩ during operation of the experiment.

The atomic beam is formed from twenty collimated jets arranged symmetrically around a hollow nozzle ring that is supplied from an electrically-heated, stainless steel oven for the potassium. The nozzle ring is positioned in front of the ionizer hotplate to provide a nearly uniform distribution of neutrals on the surface. The atomic beam flux is held nearly constant by controlling the oven temperature to within ±5°C of the desired temperature setting.

The plasma is magnetically confined in a mirror magnetic field with a variable mirror ratio. Two pairs of water-cooled magnetic coils, each with an inner diam of 14 in. and cross section normal to the current of 24 sq. in., are placed as indicated in Fig. 1a. The current in the outer pair of coils is held constant and is opposed by an adjustable current in the inner pair of coils to produce the mirror magnetic field. The axial magnetic field at the midplane is monitored at the vessel surface by a Hall-effect probe that is calibrated to ±10 G in a field of 500 G. The magnetic field on the axis at the midplane is measured to be approximately 5% less than the value measured at the vessel surface. The maximum axial magnetic field at the hotplates during the experiment is kept below 1000 G to avoid excessive $\underline{I} \times \underline{B}$ stresses on the brittle tungsten hotplate filaments.

B. Experimental Diagnostics

Figure 3 shows the placement of various diagnostic probes. The three similar coaxial Langmuir probes at the midplane are placed normal to the magnetic field and are radially adjustable from r = 0 to 15 cm. The end probe consists of two independent probes, one of which is directional. Each of the two end probes is radially adjustable from r = 0 to 6 cm for an axial range of z = 0 to 40 cm from the midplane toward the second hotplate. The ion flux collector, shown in Fig. 3, is a 3-in. diam tantalum disc that can be positioned in the plasma from outside the vacuum vessel.

Each of the three midplane probes and one of the end probes are constructed with a 0.02-cm^2 tantalum flag suspended at the end of a 15 cm length of ceramically-shielded tantalum wire that forms the center conductor of the probe. The shunt capacitance of each probe to ground is calculated to be approximately 0.4 pf/cm, and the measured resistance to ground is greater than 1000 MΩ.

The directional Langmuir probe is constructed with a 0.01-cm^2 tantalum flag inside a 0.35-cm diam tantalum cap with a narrow gap in one side. The remainder of the probe construction is similar to that for the midplane probes. In order to reach the center conductor, the ions must pass through the narrow gap, and the probe provides a measure of the ion flux in the direction of the gap orientation.

The ion flux collector is mounted on a metal rod that is inserted through a vacuum seal in the end flange with the ionizer

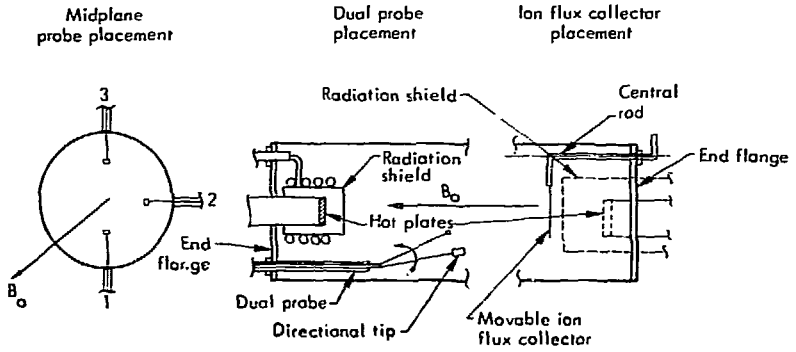

Fig. 3. Langmuir probe placement in the vessel; the dual endprobe has one directional tip for measuring the ion rotational velocity V_{oi}.

hotplate. Rotating the rod from outside the vessel moves the flux collector in and out of the plasma column.

The absolute plasma density is determined from measurements of the ion saturation current I is to the Langmuir probe. Defining r_p = effective probe radius, a_i, a_e = ion, electron gyro-radius, respectively, λ_D = plasma debye length, and λ_c = collisional mean-free-path, the present experiment satisfies the inequalities: $\lambda_D \ll a_e < r_p \ll a_i \sim \lambda_c$. When $r_p \gg \lambda_D$, the effective probe area for both ions and electrons equals the physical area; when $r_p \ll a_i$, the probe does not disturb the ion density distribution, and ion collection theories with $B_o = 0$ are valid for the evaluation of plasma density. Therefore, in the present experiment, the plasma density is calculated from the computer curves of Laframboise[33] for a cylindrical probe in a thermal plasma with $B_o = 0$.

These computer calculations have recently been carefully compared with experimental measurements in a potassium ion plasma by Chen et al.[34] using both spectroscopic and microwave techniques; agreement is obtained to within ±10%. For $r_p/\lambda_D \simeq 60$ to 80, as in the present case, the results also show that the density calculation is relatively insensitive to the actual probe space potential and to the type of probe used in the measurements. Therefore, including a ±5% error in data reduction, the density calibration in the present work is 8.0×10^9 particles/cm^3 per μA of ion current with an estimated error of ±15% in the density.

Relative density measurements are also important in determining plasma characteristics. Azimuthal correlations of

the density fluctuations are obtained from simultaneous recordings on the three midplane Langmuir probes; the data is used to determine the azimuthal mode index m, the direction of the wave propagation in the laboratory, and the phase velocity V_p of the plasma oscillations.

Axial correlations of the density fluctuations are obtained from simultaneous recordings using the non-directional end-probe and one of the midplane probes. The data is a measure of the axial wave number $k_{\parallel}$ of the plasma oscillation and the axial variation of the wave amplitude along the plasma column.

Radial correlations of the density fluctuations are obtained from simultaneous recordings with two midplane probes at different radii. The probes do not perturb either the plasma or each other. The data are used to determine the radial wave number k_r of the plasma oscillations and the radial profile of the wave amplitude.

The frequency spectrum of the plasma fluctuations is recorded with a Techtronix 1L5 spectrum analyser, calibrated for 0 to 25 kHz with a frequency dispersion of 1.0 kHz/cm. The data provide a measure of the relative wave amplitude and the individual mode frequencies in the general plasma fluctuations.

The time-average floating potential ϕ_m of the Langmuir probe is measured across a 30:1 voltage divider with an effective 30 MΩ in series with the probe. The data are used to determine the plasma sheath potential and to study the radial equilibrium in the plasma column. Since the plasma temperature is nearly constant, the slope of the radial profile of ϕ_m provides a measure of the radial electric field in the plasma column.

The fluctuating floating potential $\tilde{\phi}$ is measured with a unity-gain FET (field effect transistor) isolation amplifier that provides an effective input impedance to the probe of greater than 100 MΩ at frequencies less than 1.0 MHz. The phase-shift in the signal, introduced by the amplifier, is typically measured to be less than 2° (instrumentation limit).

Azimuthal, radial, and axial correlations of $\tilde{\phi}$ are obtained with the same techniques used for the density fluctuations. By simultaneously recording the perturbed density $\tilde{n}$ and $\tilde{\phi}$ at the same position, the phase-shift between $\tilde{n}$ and $\tilde{\phi}$ is measured, and the resulting data are important in determining the type of waves propagating in the plasma. The magnitude of $\tilde{\phi}$ is also useful in the identification of the plasma waves.

The evaluation of the absolute plasma potential in the Q-machine plasma is complicated by thermoelectric potentials and different work functions for the hotplates and the probes. Figure 4 shows the potential energy of an electron for both ion-rich and electron-rich sheath conditions at the hotplates. The plasma sheath potential, ϕ_s, is measured between the hotplate and the plasma, ϕ_W is the work function of the hotplate, ϕ_K is the work function of the probe, ϕ_f is the sheath potential for the floating probe, and all potentials in Fig. 4 are defined to be positive in the downward direction. From Fig. 4, the value of ϕ_s is given by the expression

$$\phi_s = |\phi_w| - |\phi_k| + |\phi_f| - |\phi_m| \qquad (1)$$

where all $|\,|$ terms indicate magnitude, and the sign of ϕ_s determines the type of hotplate sheath. For $\phi_s > 0$, the sheath is

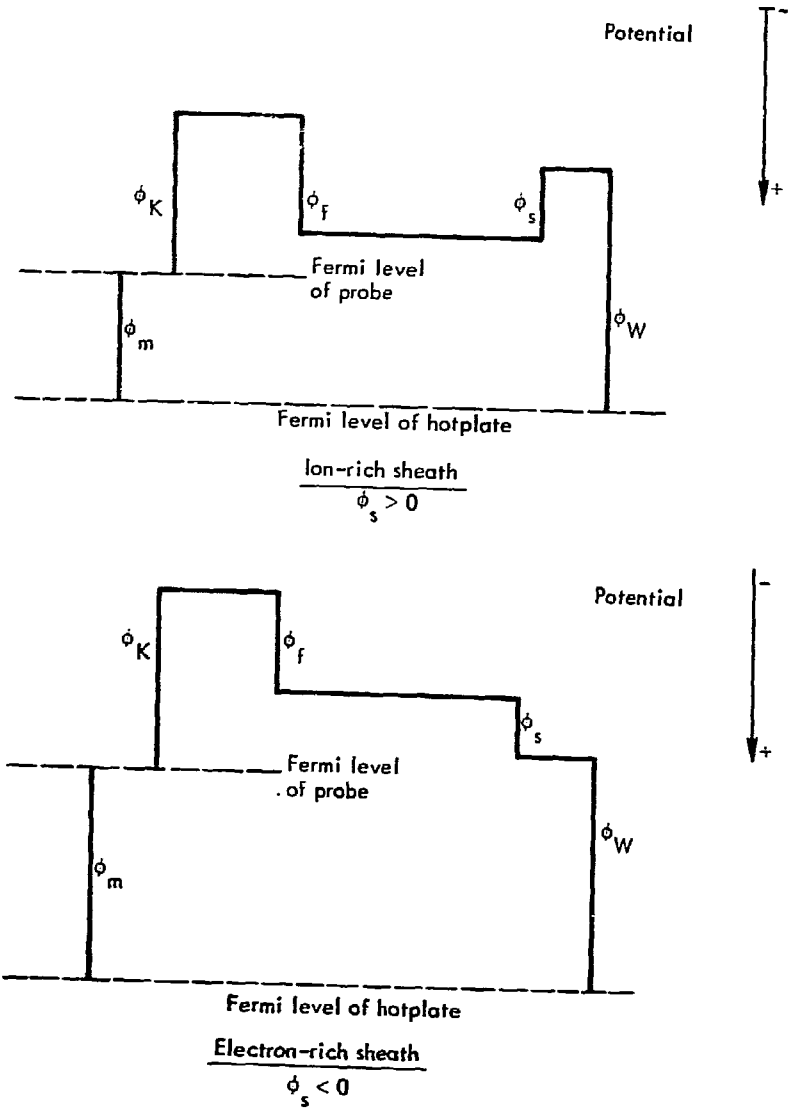

Fig. 4. Electron potential energy diagrams for the two types of sheath conditions at the hotplates.

ion-rich, and electrons are trapped in the potential well between the hotplates; for $\phi_s < 0$, the sheath is electron-rich, and the ions are now confined in the potential well between the hotplates.

With tabulated values for ϕ_W, ϕ_K, an estimated value for ϕ_f, and measured data for ϕ_m, the value of ϕ_s is determined from Eq. 1. However, the proper values of the potentials for use in the present experiment require further discussion.

Experimental values reported in the literature vary widely for both work functions, ϕ_W and ϕ_K.[35-36] For tungsten plates, ϕ_W varies between 4.25 and 5.15 V. The variations occur because both the orientation of the surface crystalline structure and the method of measurement have a strong effect on the results. In his work with cesium-on-tungsten ionization, von Goeler[37] used $\phi_W = 4.54$ V, which appears to be the mean value quoted in the literature.[36] Therefore, $\phi_W = 4.54$ V is adopted for the present experiment.

For unheated tantalum probes in a potassium plasma, the probe is probably coated with potassium, and the value of ϕ_K is expected to be very close to the work function of potassium. In the literature, experimental values listed for ϕ_K vary between 1.6 and 2.35 V[36]; the lower limit is determined by the method of contact potentials, while the upper limit is measured by other means. In the measurements of Chen et al.,[34] $\phi_K \approx 1.8$ V is used. For the present work, the value of ϕ_K is assumed to lie between 1.6 and 2.35 V, with the most probable value near 1.8 V.

The evaluation of ϕ_s in Eq. 1 also requires a value for ϕ_f. Several theoretical studies have shown that ϕ_f is given by an expression of the form[38-40]

$$e\phi_f/KT = \ln(b\sqrt{m_e/m_i}) \qquad (2)$$

with m_e/m_i as the mass ratio of electrons-to-ions and b is a correction factor dependent on experimental conditions. Bohm[38] showed that b depends on the sheath boundary conditions. The work of Bickerton and von Engel[39] indicated that b was a function of the ratio a_e/λ_c, while the calculations of Chen[40] showed that b could be related to the ratio of the probe collection area of the ions to that of the electrons in a magnetic field. The recent computer calculations of Laframboise[33] for cylindrical probes indicate that for $r_p/\lambda_D \geq 10$, $b \simeq 2.5$ and is relatively insensitive to the probe size and shape. Chen et al.[34] found $b \simeq 2.6$ for cylindrical probes with $r_p/\lambda_D \simeq 50$. For the present conditions, $r_p/\lambda_D = 60$ to 80 and b is taken to be 2.5, giving $\phi_f \simeq -1.06$ V at T = 2600°K.

Therefore, the net result of the discussion on the potentials used in Eq. 1 is: $\phi_W = 4.5$ V, $\phi_f = -1.06$ V at T = 2600°K, and ϕ_K somewhere between 1.6 and 2.35 V.

An important plasma parameter that is calculated from measurements of ϕ_m is the time-average radial electric field E_{ro}. In principle, E_{ro} is determined from $-\partial\phi_p/\partial r$ where ϕ_p is the space potential of the plasma. From Fig. 4, $\phi_p \simeq |\phi_f| - |\phi_k| - |\phi_m|$ where ϕ_m is the only term that has a

measurable variation with radius. Therefore, $E_{ro} = -\partial\phi_m/\partial r$ in the experiment.

The directional Langmuir probe previously described is used to obtain a direct measure of the ion rotational velocity V_{oi} in the plasma. The ion saturation current to the probe is measured first with the shield gap orientated in the direction of plasma rotation and then with the probe gap facing in the opposite direction. The value of V_{oi} is determined by[41]

$$V_{oi} = (\Delta I_i/I_i)\sqrt{KT/m_i} \tag{3}$$

where ΔI_i is the difference in the two measured currents with I_i as the current recorded in the direction opposed to the plasma rotation. The value of V_{oi} measured in this manner can be compared with both the $\underline{E}x\underline{B}$ and the diamagnetic drift velocities.

Another plasma parameter of major importance in the evaluation of the plasma losses is the total ion flux emission from the ionizer hotplate. Using the flux collector previously described, the total ion saturation current provides a direct measurement of the neutral beam flux j_o.[9,18] The total ion flux into the plasma is given by sj_o where s is the probability of ionization for either ions or neutrals when striking the hotplate. The measured ion current is related to j_o by[42]

$$I_o/e \simeq 2\pi\int_o^a sj_o(r)rdr \tag{4}$$

For an electron-rich sheath, s is closely approximated by La(T)/(1 + La(T)) where La(T) is the Langmuir-Saha factor.[18,37] Using the first ionization energy of potassium,[35]

4.31 V, with T = 2600°K, La(T) = 1.35 and s = 0.58. For an ion-rich sheath, the ions suffer multiple reflections which, in the approximation limit of an infinite number of reflections, gives $s = H/(1 + H)$ with $H = La(T)\exp(-e\phi_s/KT)$.[18]

The relation between I_o and j_o is seen to depend on the radial profile for $j_o(r)$. If j_o is assumed uniform over the hot-plate surface, $j_o \approx (I_o/e)/(\pi a^2 s)$; if $j_o(r)$ is assumed to be a Gaussian with a scale-length r_o, $j_o \approx (I_o/e)/(\pi r_o^2 s)$. These relations will be useful in the evaluation of the plasma loss measurements in Chapter V.

The plasma electron temperature T_e is measured with the midplane Langmuir probes and corrected for the effects of finite probe size using the computer curves of Laframboise.[33] The total corrected probe current is plotted on semi-log coordinates as a function of the probe bias, and the value of T_e is derived from the straight-line slope near the origin.

The hotplate temperatures are measured with an optical pyrometer that is calibrated against a standard optical source over an equivalent optical path to that used in the experiment. Corrections to the calibration are made for the effects of optical reflection coefficients and transmission through vacuum windows. To avoid making optical measurements in the plasma, the hot-plate temperatures are measured without the plasma and are used to calibrate the hotplate power controls. During experimental operations, the plate temperatures are set from these power calibrations. Repeated settings of the hotplate temperature from the calibration showed an average deviation of ±20°K

from the desired temperature in the plate center. The pyrometer calibration against the standard source is accurate to ±10°K. Including the effects of the optical path and optical corrections leads to an absolute temperature calibration accurate to approximately ±75 to 100°K at the hotplate center.

III. PLASMA EQUILIBRIUM

A. General Description

Early experiments on the magnetic confinement of Q- machine generated plasmas in both uniform and non-uniform magnetic fields indicated that the time-average plasma losses were due to a combination of radial classical diffusion and an anomalously large rate of volume ion recombination.[43-45] The measured recombination rate could not be accounted for by any known process of three-body volume recombination.[21] In order to explain the results of measurements in a cesium plasma, von Goeler devised a simple model of thermal plasma equilibrium that included surface ion recombination at the hotplates.[37] The model predicted an effective wall recombination rate in accord with the experimental results and showed that the neutral beam density should vary quadratically with the density n_o.

Measurements of the plasma losses in Q-machine plasmas using different types of alkali metal ions indicated that the von Goeler relation $j_o \propto n_o^2$ was well satisfied for $n_o > 10^{11}/cm^3$, but at lower densities, the losses showed a $j_o \propto n_o$ variation.[46-47] The linear relation between j_o and n_o was interpreted to show the presence of anomalous loss processes in the plasma, but some recent theoretical considerations indicate that $j_o \propto n_o$ is predicted for incomplete thermalization of a nearly collisionless plasma in the presence of electron-rich sheaths.[18] However, the measurements undertaken to verify the theory still indicated

the presence of anomalous losses that could not be accounted for by the theoretical model.

A recent experiment with a rotating hotplate filament assembly has demonstrated that a marked increase in n_o may be achieved in certain cases whenever the filament rotation rate exceeds approximately 10 Hz.[42] The explanation advanced for the increase in n_o is a reduction in the radial $\underline{E}x\underline{B}$ convection due to the non-uniform hotplate heating in the absence of the filament rotation. For some experimental conditions, the reduction in the losses is sufficient to produce $j_o \propto n_o^2$, while for other conditions, anomalous losses are still sufficient to produce $j_o \propto n_o$ in the plasma.

In the present experiment, the plasma equilibrium is formed in a regime where the scale-length R of $n_o(r)$ may be comparable in magnitude with both a_i and λ_c in the column. In the collisional limit, $a_i >> \lambda_c$, the guiding-center density is equal to the ion particle density and the ions experience only the local electric field in the plasma.[48] As the collision rate decreases, the ion particle density along the orbit may differ significantly from the density of the guiding centers, and the ions are able to sample more of the non-uniform electric field over the orbit cross section. In the collisionless limit $a_i << \lambda_c$, Schmidt[48] and Stringer[49] have calculated second-order corrections in the ratio a_i/R for both the particle density and the mean electric field experienced by the ions. These corrections depend on the averaging of the spacially inhomogeneous quantities over many periods of the ion gyromotion so that any process,

such as particle collisions, which interrupts the ion orbits, will destroy the effect of the finite Larmor radius averaging. When $a_i \sim \lambda_c$, the guiding center theory provides a reasonable first approximation for the calculation of equilibrium for comparison with the measured data.

The type of equilibrium that is formed in the rotating plasma of this experiment is important to any investigation of enhanced or anomalous plasma losses. It is necessary to obtain at least a qualitative understanding of the origin of the equilibrium losses before any meaningful evaluation of any transient losses becomes feasible. The remainder of this chapter is organized as follows. Section IIIB discusses measurements of both the hotplate temperature and the plasma electron temperature. Section IIIC discusses the equilibrium measurements of the density, potential, radial electric field, and the ion rotational velocity in conjunction with a two-dimensional fluid model of the plasma equilibrium. Section IIID discusses the evaluation of various equilibrium loss processes in the plasma in conjunction with measurements of the total plasma losses from the column.

B. Temperature Measurements

Since any temperature asymmetry at the hotplates can produce a potentially large $\underline{E}x\underline{B}$ radial convection of plasma across B_o, a highly symmetrical distribution of the hotplate temperature is desirable for the study of the possible origins of anomalous losses. Several authors[28,50-51] have shown that

thermal gradients in a Q-machine plasma produce electric fields proportional to $\phi_W(\nabla T/T)$, where ∇ is the gradient operator and $\phi_W = 4.54$ V in the present work. Therefore, small thermal gradients at the hotplates can create relatively large electric fields in the plasma column, and the resulting $\underline{E}\underline{x}\underline{B}$ drift across B_o may be an important factor in the loss of ions from the plasma column.

For nearly symmetrical temperature and density distributions in the plasma, a radial temperature gradient produces an $\underline{E}\underline{x}\underline{B}$ plasma rotation that is important in determining the direction of propagation of any waves in the column[28,51] and may be important in determining the stability of the plasma equilibrium. However, other effects such as plasma viscosity, ion inertia, and column boundary conditions must be included in any analysis of the column equilibrium.

In the absence of plasma in the vessel, optical measurements of the hotplate temperature T are recorded as described in Chapter II. Figure 5 shows constant-temperature contours for each hotplate and at two different central temperatures, T = 2400°K and T = 2600°K. For a central T = 2600°K, the ionizer hotplate shows a maximum estimated azimuthal temperature gradient of 5°K/radian, corresponding to $|E_\theta| = 4.5$ mV/cm at r = 2 cm. The resulting radial $\underline{E}\underline{x}\underline{B}$ velocity is $V_E = 3.0 \times 10^3$ cm/sec which is much less than the ion thermal velocity $V_{Ti} = 10^5$ cm/sec. However, because the isotherms from the azimuthal temperature gradient are

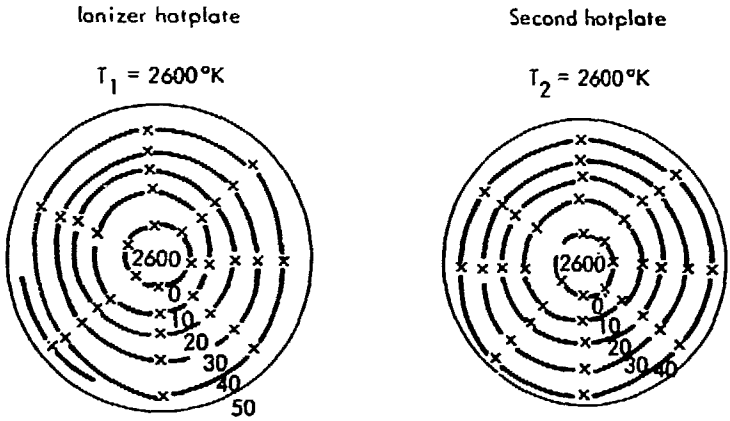

Fig. 5a. Constant-temperature contours on the ionizer hotplate for central temperatures of T = 2400°K and 2600°K.

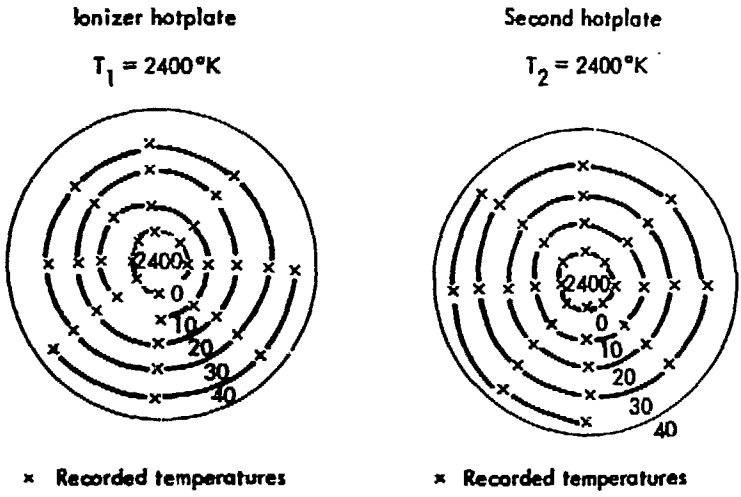

Fig. 5b. Constant-temperature contours on the second hotplate for central temperatures of T = 2400°K and 2600°K.

closed within the hotplate cross section, the net radial plasma loss is zero, and the plasma can only circulate within the column.[30]

Figure 5 also shows that T(r) increases with radius from the plate center to the edge with a maximum radial temperature gradient of 50°K/cm at T = 2600°K on the ionizer hotplate, corresponding to $|E_{ro} \sim 0.09$ V/cm and a rotational doppler frequency of $f_D \sim 5.0$ kHz at r = 2 cm and $B_o = 150$ G. The corresponding ion cyclotron frequency at $B_o = 150$ G is $f_{ci} = 6.0$ kHz, so that f_D and f_{ci} are of comparable magnitude in the plasma column. The direction of the column rotation indicated by the sign of f_D in the column depends on the sign of E_{ro} which remains to be determined. Similar results to those just discussed are calculated from the data at T = 2400°K for the ionizer hotplate and from the data for the second hotplate.

The plasma electron temperature T_e is measured as described in Chapter II at the vessel midplane and compared with the corresponding hotplate temperature (equal T on both hotplates). Figure 6a shows the current-voltage plots for three values of B_o. At $B_o = 150$ G, the measured $T_e = 3140° \pm 50°$K; at $B_o = 600$ G, the apparent electron temperature increases to $T_e = 3500° \pm 75$ to 100°K at the plate center. The indicated difference between the measured values of T_e and T could be caused by potassium contamination of the probe. The results of Chen et al.[34] in a potassium ion plasma indicated that probe contamination causes a decrease in the slope of the measured probe curves near the transition region,

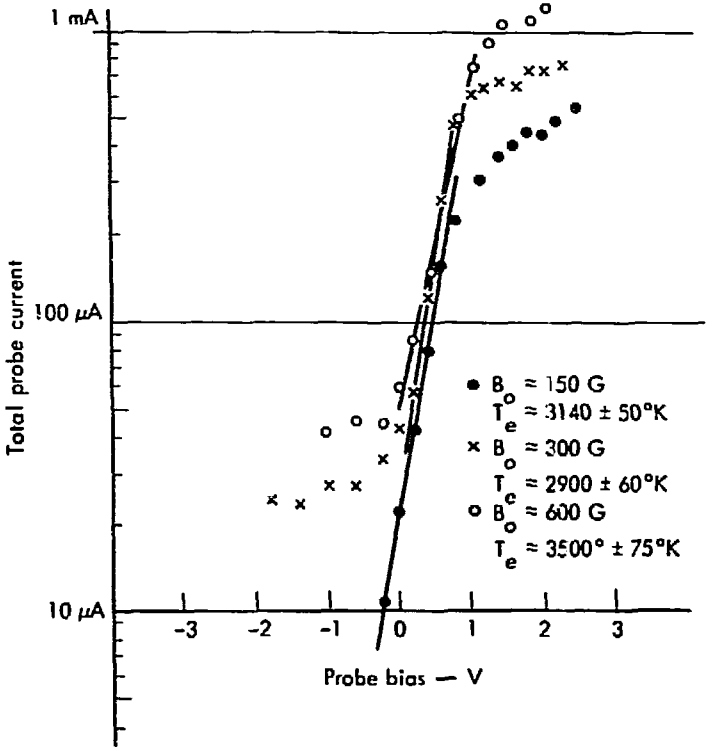

Fig. 6a. Measured T_e for B_o = 150, 300, and 600 G with T = 2600°K on both hotplates and T_o ≈ 300°C.

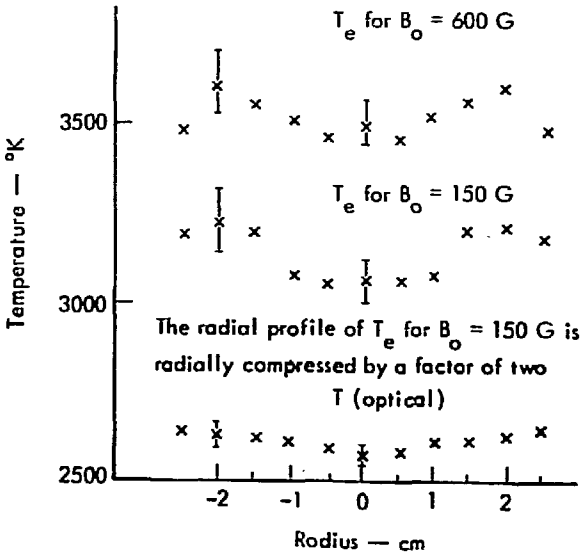

Fig. 6b. Comparison of the measured radial profiles with T_e and T at B_o = 150 G and 300 G with T_o = 300°C.

leading to a spuriously high value for T_e.[34] Due to the method of plasma generation in a Q-machine with equal temperatures on both hotplates, significant thermal gradients between the hotplates are not expected[52]; any local temperature variations along the magnetic field should be eliminated in less than 1 msec. Therefore, the difference between T_e and T on the same field line is improbable in the present experiment, and within experimental error, $T_e \approx T$.

Figure 6b shows a comparison of the radial profiles of T_e at the midplane for two values of B_o with the radial profile of T at the ionizer hotplate. The radial coordinate of the profile for B_o = 150 G is compressed by 50% in order to allow comparison with the T_e profile at B_o = 600 G and the profile of T. At the midplane, T_e increases with radius out to the effective edge of the hotplate and then appears to decrease. The corresponding profile of T shows a nearly linear increase with radius out to the hotplate edge. Simple estimates of the thermal diffusion across B_o indicate that T_e at the midplane should not significantly decrease until a distance of several times a_i from the effective hotplate edge.[53] However, the potential discontinuity near the hotplate edge plays an important role in interpreting the data presented in the next section.

C. Density and Potential Measurements

The plasma equilibrium is to be determined from essentially four basic measurements: Figure 7a shows radial profiles of ϕ_m as a function of B_o. Using the relation,

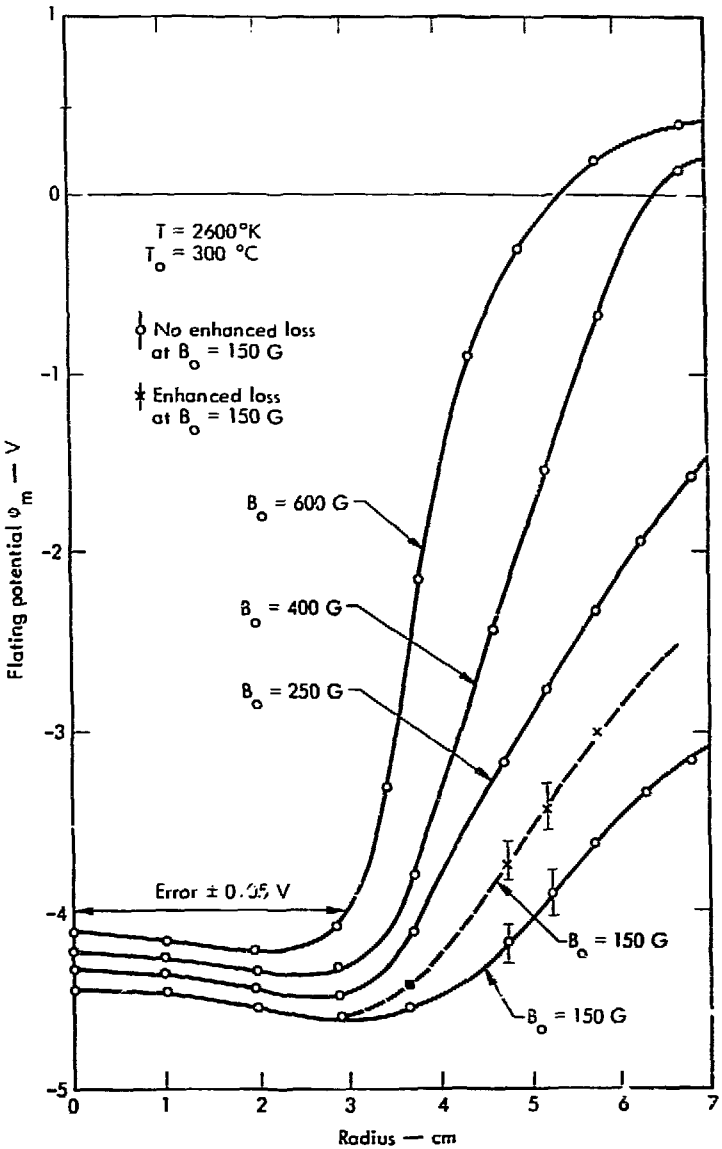

Fig. 7a. Measured radial profiles of ϕ_m as a function of B_o for T = 2600°K and T_o = 300°C; two profiles, with and without anomalous radial losses, are shown for B_o = 150 G.

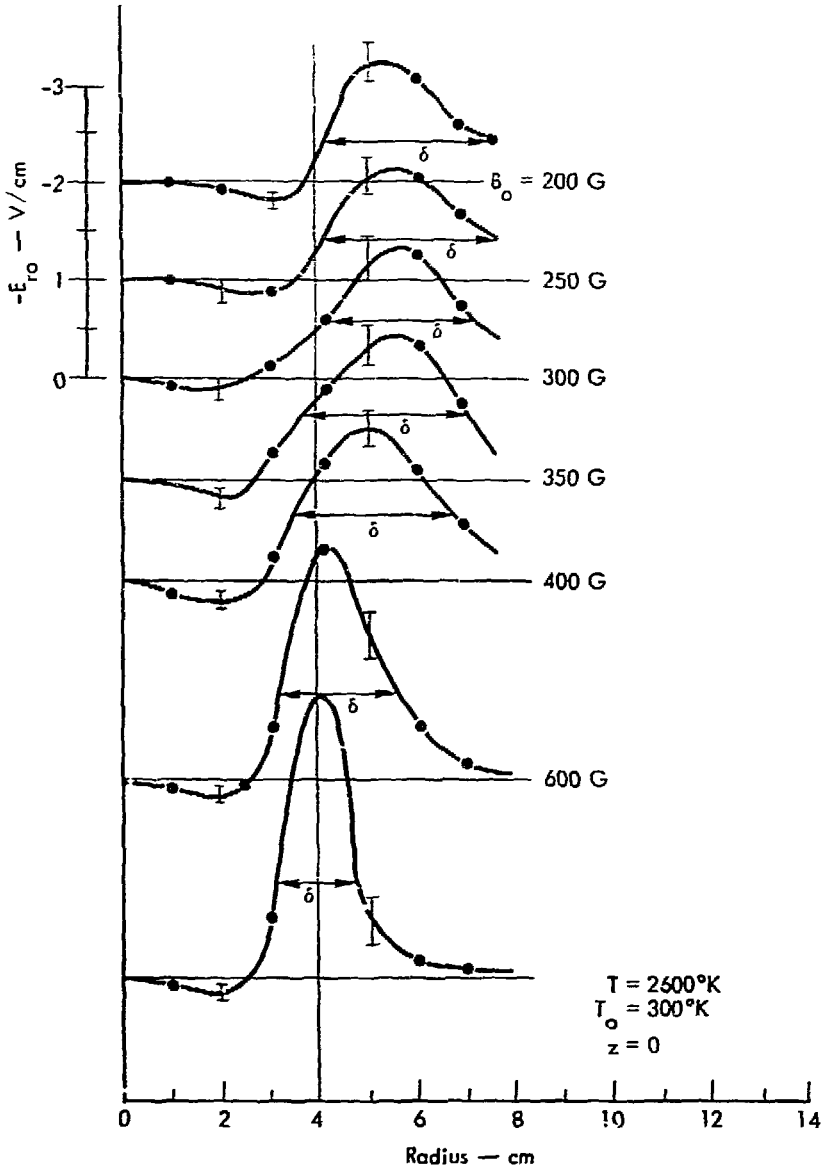

Fig. 7b. Calculated radial profiles of $-E_{ro}$ from the data in Fig. 7a.

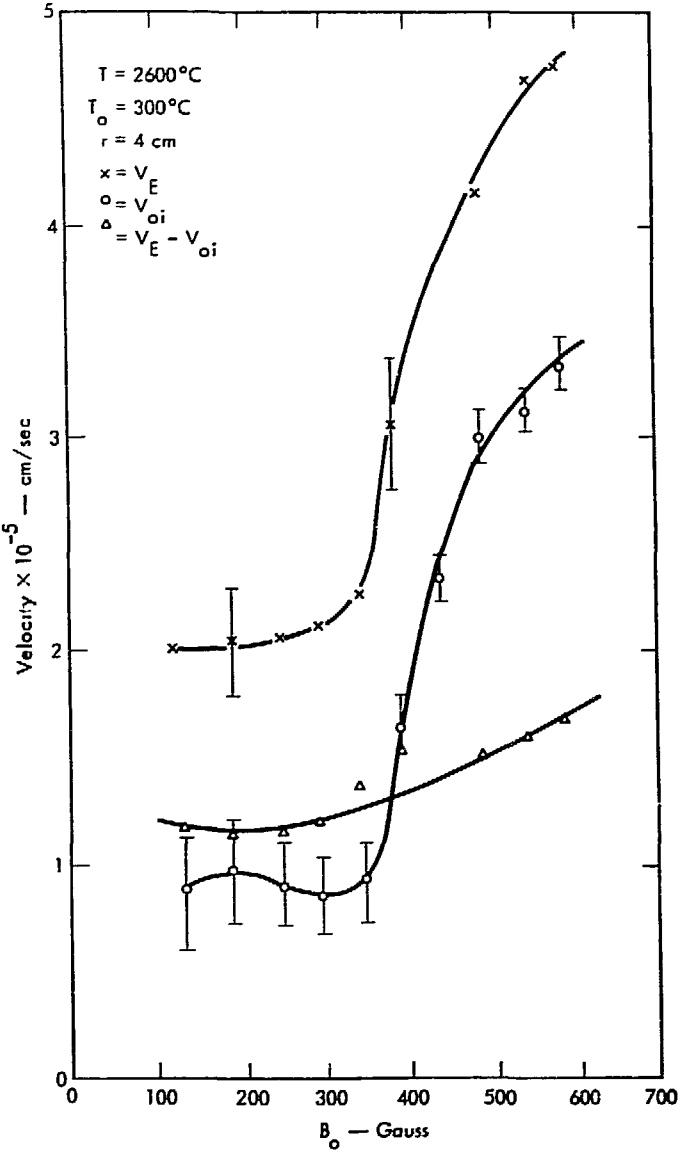

Fig. 7c. Comparison between the measured V_{oi} at r = 4 cm and the value of V_E calculated from the data in Fig. 7b; the difference V_E-V_{oi} is also shown.

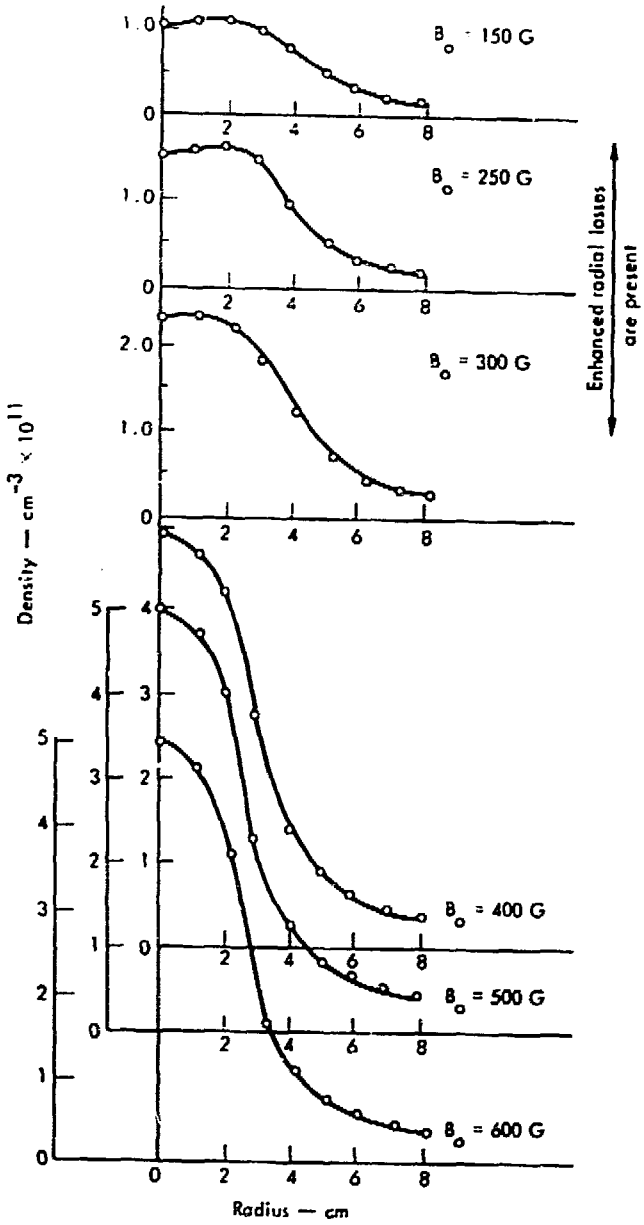

Fig. 7d. Measured radial profiles of n_o as a function of B_o for T = 2600°K and T_o = 300°C; the profile at B_o = 150 G is with anomalous losses.

$E_{ro} = -\partial\phi_m/\partial r$. Fig. 7b shows the corresponding radial profiles of $-E_{ro}$. Using the directional Langmuir probe described in Chapter II and the relation, $V_E = -E_{ro}/B_o$, Fig. 7c shows V_{oi} and V_E as a function of B_o at r = 4 cm in the plasma column; Fig. 7c also shows the difference $V_E - V_{oi}$ as a function of B_o. Finally Fig. 7d shows radial profiles of n_o as a function of B_o. All of the data in Fig. 7 is recorded for T = 2600° ± 75 to 100°K at the hotplate center and T_o = 300° ± 5°C at the bottom of the potassium oven. The remainder of this section is devoted to the interpretation of the results shown in Figs. 7a, b, c, d and the formulation of a qualitative model of the plasma equilibrium in the column.

The discussion in Section IIIB of this chapter indicates that plasma models which are valid for a_i, $a_e << R$ should give a good first-approximation to the analysis of a collision-dominated plasma with $a_e << R - a_i$. When the net current between the hotplates is zero in a Maxwellian plasma at a temperature T, the total flux balance at the ionizer hotplate gives the relation[37,40]

$$\exp(e\phi_s/KT) = [j_{er}/Ri(T)]\left[\frac{1 + sj_o/j_{er}}{1 + sj_{ir}/Ri(T)}\right] \qquad (5)$$

where j_{er}, j_{ir} is the random electron, ion flux, respectively; s, j_o, and ϕ_s are defined in Chapter II, and Ri(T) is the electron emission flux given by[37]

$$Ri(T) = (A/e)\,T^2 \exp(-e\phi_W/KT) \qquad (6)$$

with A as the effective electron emission coefficient of the hotplate. For a typical vacuum-annealed tungsten surface, A varies between 60 and 100 amps/cm^2-deg^2; quantum theory predicts a maximum A = 120.6 amps/cm^2-deg^2 for any pure metal.[35]

In the present work, $Ri(T) \gg j_{ir}$ and $j_{er} \gg j_o$ so that the second bracketed term in Eq. 5 is very close to unity. Therefore, ϕ_s is essentially determined by the electron flux balance at the hotplate. When $Ri(T) \langle j_{er}, \phi_s \rangle 0$ and the sheath is ion-rich with the electrons confined in a potential well between the hotplates; the ions are unrestrained by the sheath. When the inequality is reversed, $\phi_s < 0$ and the sheath is now electron-rich. The ions are confined in a potential well between the hotplates, and the electrons are unrestrained by the sheath.

The type of sheath that exists at the hotplates may be determined from the data in Fig. 7a at r = 0. Since the actual value of the potassium work function in the experiment is unknown, the data are evaluated at three selected values within the tabulated range of ϕ_k. This value, ϕ_k = 1.6 V, was measured by the method of contact potentials,[35] ϕ_K = 1.8 V was used in the work of Chen et al.,[34] and ϕ_k = 2.1 V represents the most probable value of the potassium work function in the tabulated data.[35]

The sheath potential ϕ_s is evaluated from the data at r = 0 in Fig. 7a by using Eq. 1 with ϕ_W = 4.5 V, ϕ_f = -1.06 V at T = 2600°K, and the three choices for ϕ_K; the ratio $e\phi_s/KT$ is plotted in Fig. 8a as a function of the measured n_{oo} (n_o at r=0)

in Fig. 7d; each point represents a different value of B_o in all three cases shown. For all the data points shown in Fig. 8a, $\phi_s < 0$, and the hotplate sheaths are electron-rich. Therefore, the equilibrium plasma in the present experiment is formed in the presence of electron-rich sheath potentials on the hotplates.

A quantitative comparison between Eq. 5 and the data in Fig. 8a is possible only with some assumptions for the parameters ϕ_W, A, and T. The value of ϕ_W was discussed in Chapter II, and the value $\phi_W = 4.54$ V appears to be a commonly accepted result.[37] Tabulated values of A vary between 60 and 100 amps/cm^2-deg^2 for a clean tungsten surface.[35] Measured values of T can vary by ±100°K, as discussed in Chapter II. Therefore, Eq. 5 is evaluated for both T = 2600°K and T = 2700°K with selected values of A = 60 and 120 amps/cm^2-deg^2 for each temperature, and the results plotted in Fig. 8a for comparison with the measured data. The estimated probable error at selected points is also shown. Within the assumptions discussed, the results in Fig. 8a show that a value of ϕ_K between 1.6 and 1.8 V provides reasonable agreement between the data and the predictions of Eq. 5, and the functional dependence of ϕ_s on n_{oo} is correctly predicted.

The radial profiles of ϕ_m in Fig. 7a are next studied for $r \neq 0$ in two separate regions, $r < a$ and $r > a$ where a is the effective hotplate radius at the midplane in the mirror magnetic field. For $r < a$, $\phi_m(r)$ shows a decrease with radius for all values of B_o shown. The decrease in ϕ_m can be numerically predicted from a combination of Eqs. 1, 5, and 6. Neglecting

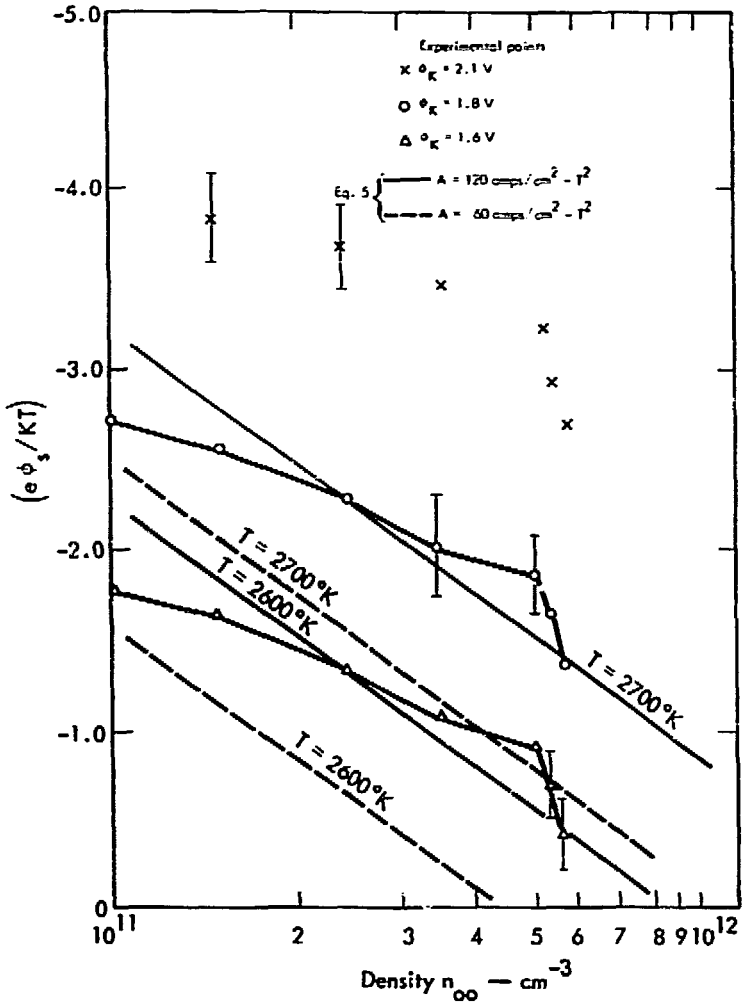

Fig. 8a. Comparison between the prediction of Eq. 5, with A = 60 or 120 A/cm^2-T^2, and Eq. 1 with measured ϕ_m and ϕ_K = 1.6, 1.8, and 2.1 V; T = 2600°K and T_o = 300°C. The sheath is electron-rich.

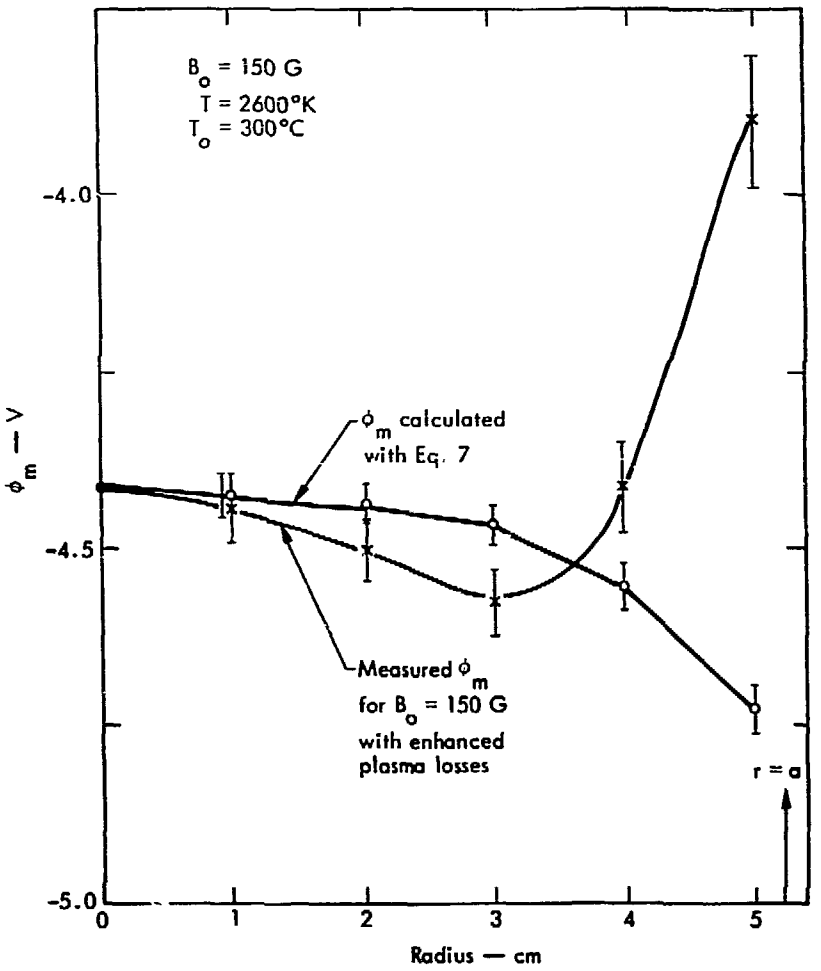

Fig. 8b. Comparison between predicted $\phi_m(r)$ from Eq. 7 and data for B_o = 150 G, r < a, T = 2600°K, and T_o = 300°C in the plasma.

the small radial dependence of both ϕ_W and ϕ_f (see Chapter II) and considering both T and n_o as functions of radius, $\phi_m(r)$ is given by

$$\phi_m(r) = (KT/e)\{\ln[n_o(r)] - 1.5\ln[T(r)] + C_o\} \qquad (7)$$

where C_o is a constant, independent of the radius. Using $\phi_W = 4.54$ V, $A = 60$ amps/cm^2-deg^2, $\phi_f = -1.06$ V at T = 2600°K, $\phi_m = -4.4$ V at r = 0, and $n_{oo} \approx 10^{11}/cm^3$ in the presence of anomalous plasma losses, C_o at $B_o = 150$ G is calculated to be, $C_o = -36.55$. Substituting this value of C_o and data from Figs. 5b and 7a in Eq. 7, $\phi_m(r)$ is calculated and plotted in Fig. 8b as a function of radius. The curve for ϕ_m at $B_o = 150$ G in the presence of enhanced losses is repeated in Fig. 8b for comparison with the prediction of Eq. 7. Within the assumptions involved, Eq. 7 is in good agreement with the measured $\phi_m(r)$ at $B_o = 150$ G out to r = 4 cm; beyond this point, the effect of the region for r > a becomes the dominant factor determining $\phi_m(r)$. Since the curves of ϕ_m at all values of B_o in Fig. 7a show the same type of radial variation for r < a, the results for $B_o = 150$ G in Fig. 8b should be valid for other values of B_o. Therefore, the decrease of ϕ_m with radius in Fig. 7a is accounted for by the prediction of Eq. 7 in both form and magnitude for r < a in the plasma column.

For r > a, Fig. 7a shows that $\phi_m(r)$ rises sharply a distance of a few centimeters to produce an ion-confining potential well in the plasma column. This rapid increase in ϕ_m is caused by an abrupt change in the endplate work function

at r = a. Inside the column, the magnetic field lines terminate on a hot emissive tungsten surface that is in strong contrast to the cold non-emissive surface for r > a. In addition, the cold surface is probably coated with potassium, so that the potential difference in the column approaches a few volts with the column interior more negative than the exterior. The resulting E_{ro} is directed into the plasma, and the plasma current flows in the direction of E_{ro}.

The magnitude of E_{ro} indicated in Fig. 7b should completely confine the ions to the column, but the measurements shown in Fig. 7d show that a substantial number of ions escape from the column for the whole range of B_o. A quantitative comparison is shown in Fig. 9 between the calculated density distribution $n_o(r) \propto \exp(-e\phi_s/KT)$, using the measured ϕ_s, and the measured n_o radial profile at B_o = 150 G (with enhanced radial losses). The profiles clearly indicate that some mechanism is overcoming the strong E_{ro} and allowing the ions to flow out of the potential well.

The strong value of E_{ro} at the column edge produces an ExB electron drift that is transmitted to the more massive ions through coulomb collisions. Therefore, the plasma rotation provides a possible source for the energy required for the escaping ions. Figure 7c shows that the measured V_{oi} at r = 4 cm is always less than the corresponding V_E for the entire range of B_o, and the ratio V_{oi}/V_E increases toward unity as B_o increases. Since a_i/R decreases with increasing B_o, the finite Larmor radius correction to the E_{ro} experienced by the

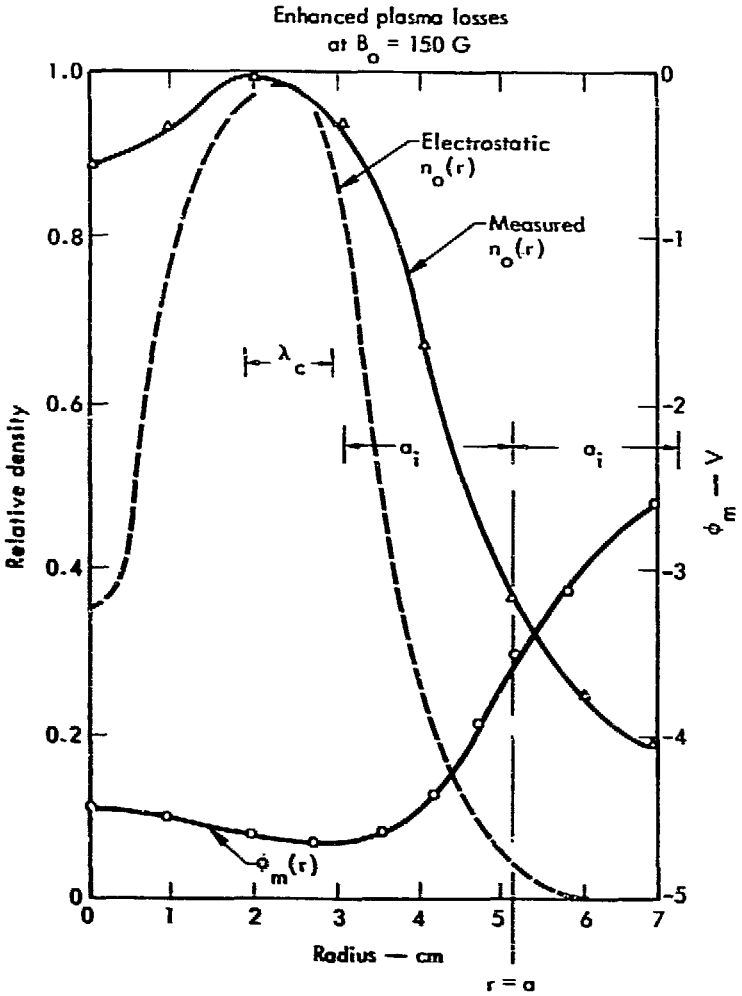

Fig. 9. Comparison between the measured $n_o(r)$ and the corresponding Boltzmann distribution for T = 2600°K, T_o = 300°C, and B_o = 150 G. The corresponding $\phi_m(r)$ is also shown for comparison.

ions decreases, and the predicted V_{oi} approaches V_E, in agreement with the results in Fig. 7c. The velocity difference $V_E - V_{oi}$ is also plotted in Fig. 7c and indicates an azimuthally circulating current j_θ in the direction opposing the $\underline{E}x\underline{B}$ plasma rotation. The current j_θ appears to be nearly independent of B_o for the range of B_o shown in Fig. 7c.

On the basis of the data in Fig. 7, a two-dimensional fluid model of the plasma equilibrium is constructed and includes the effects of both ion inertia and viscosity; the coupling of the ions and electrons through coulomb collisions is represented by a plasma resistivity. Both the electron inertia and viscosity are neglected in comparison with the ion terms. The resulting single-fluid equations are written in the form[53]

$$\rho \underline{u} \cdot \nabla \underline{u} + \nabla p_i + \nabla p_e = \rho \mu_i \nabla^2 \underline{u} + \underline{j} x \underline{B}_o \tag{8}$$

$$\underline{E} + \underline{u} x \underline{b}_o - \frac{\nabla p_i}{n_o e} = \eta \underline{j} + (\rho / n_o e)(\underline{u} \cdot \nabla \underline{u} - \mu_i \nabla^2 \underline{u}) \tag{9}$$

where $\underline{u} \simeq \underline{u}_i$ is the mass flow velocity, $\rho \simeq n_o m_i$ is the mass density, $p_i = p_e \simeq n_o KT$ is the pressure, μ_i is the ion viscosity, $\underline{j}$ is the current, $\underline{E}$ is the electric field, η is the plasma resistivity, ∇ is the gradient operator, and ∇^2 is $\nabla \cdot \nabla$ in cylindrical coordinates.

The approximate ion viscous forces in the above equations are based upon the Navier-Stokes model of an incompressible viscous fluid and strictly apply to a plasma with $\nabla \cdot \underline{u} = 0$[54];

since the plasma density varies, the validity of this assumption is questionable. However, if the additional assumption $u_r < u_\theta$ is made, the compressibility condition introduces only small corrections to the viscous terms in the equations. For the present calculations μ_i is approximated by the form, $(p_i/\nu_{ii})\left(1 + \lambda_c^2/a_i^2\right)$, with ν_{ii} as the collision rate between the ions.[55] Since the plasma is highly ionized at T = 2600°K, the plasma resistivity is approximated by the Spitzer[53] result for a fully ionized gas, $\eta \simeq 1.29 \times 10^4\, T^{-3/2} \ln(\Lambda)$ where $\ln(\Lambda)$ is the coulomb logarithm; at T = 2600°K, $\eta \simeq 0.84$ ohm-cm.

Equation 8 is separated into the radial and azimuthal components, and each is solved for the current. Under the condition that $u_r \ll u_\theta \cong V_{oi}$, the radial current is given by

$$j_r \simeq \rho\mu_i \nabla_r^2 V_{oi}/B_o \tag{10}$$

where $\nabla_r^2 = (\nabla \cdot \nabla)_r$. The azimuthal current is given by

$$j_\theta \simeq 2(\partial p_i/\partial r)/B_o - \rho V_{oi}^2/rB_o \tag{11}$$

Assuming that $V_{oi}(r) \propto V_E(r)$ for all radii at a given B_o, the results in Fig. 7c are proportional to the radial profiles of V_{oi} in the plasma. Near the center of the high velocity region, $\nabla_r^2 V_{oi} \propto \nabla_r^2 E_{rc} < 0$, and j_r flows into the plasma, in agreement with the requirement that E_{ro} confines the ions within the column. In the region of the maximum V_{oi}, the centrifugal force dominates over

the pressure term in Eq. 11, and j_θ flows in the direction opposing the plasma rotation.

In Fig. 7b, the requirement that $\nabla_r^2 V_{oi} \propto \nabla_r^2 E_{ro} < 0$ defines an effective width δ for the region of large V_{oi} in the plasma. Replacing the term $\nabla_r^2 V_{oi}$ by the approximation, $-V_{oi}/\delta^2$ in Eq. 10 gives an estimate of the j_r flowing into the plasma. For $B_o \simeq 600$ G in Fig. 7b, $\delta \simeq 2$ cm, $a_i \simeq 0.5$ cm, and $V_{oi} \simeq 3.0 \times 10^5$ cm/sec; using Fig. 7d to estimate n_o, $j_r \simeq -0.1$ mA/cm^2. Considering the current continuity in the high velocity layer, the axial $j_z \simeq (2rL/a^2) j_r \simeq +.0$ mA/cm^2; multiplying j_z by η and L(column length) leads to an estimate of approximately 1.0 V for the voltage drop along B_o. When $B_o < 600$ G, the potential drop along B_o is less than 1.0 V. Thus, for the range $150 \text{ G} \lesssim B_o < 600$ G, more than 50% of available thermoelectric potential should appear across the velocity shear region in the plasma column.

The value of E_{ro} in the column is calculated from the radial component of Eq. 9 in the form

$$E_{ro} = -V_{oi}B_o + (dp_i/dr)/n_o e + \eta j_r - \rho V_{oi}^2/n_o e r \qquad (12)$$

In the velocity shear region, $\eta j_r \propto \sqrt{(m_e/m_i)}$ and $\partial p_i/\partial r \propto V_{Ti}^2$ are both negligible in comparison with the terms in V_{oi}, and Eq. 12 may be solved for V_{oi} in terms of V_E. Using data from Fig. 7b and including the small corrections due to $\partial p_i/\partial r$ with data from Fig. 7d, V_{oi} is calculated at the radial position of the maximum $|E_{ro}|$ and plotted as a function of B_o in Fig. 10.

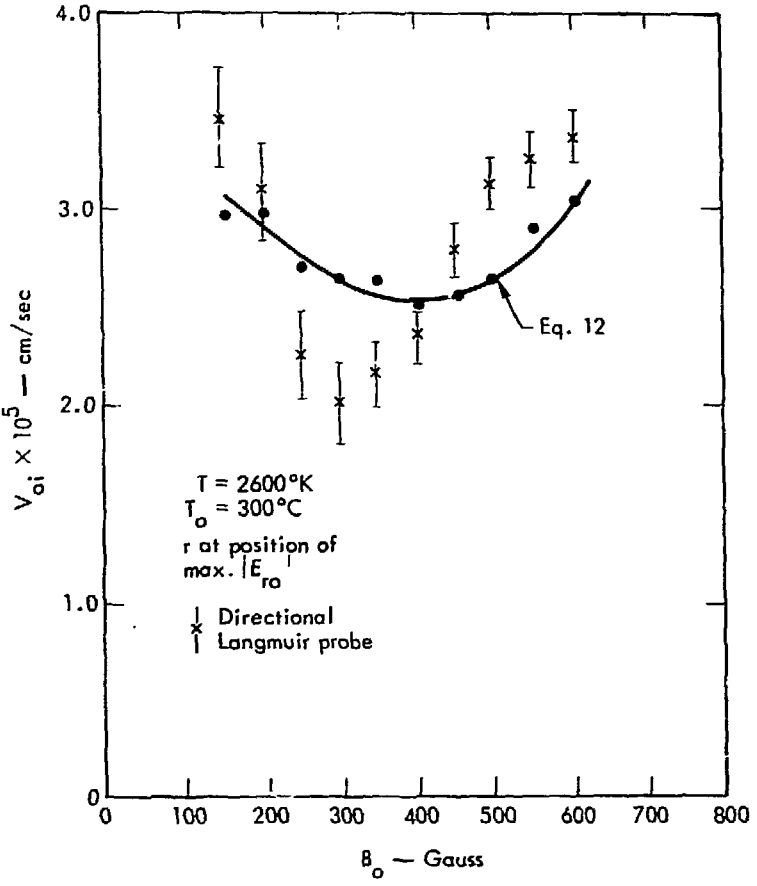

Fig. 10. Comparison between the prediction of Eq. 12 and the measured V_{oi} at the maximum $|E_{ro}|$ in Fig. 7b as a function of B_o; T_o = 300°C and T = 2600°K.

Measured data for V_{oi} as a function of B_o is available only at r = 4 cm in the column. Using Eq. 12 to compute the ratio V_{oi}/V_E at B_o = 150 G, the ratio is found to be 0.4 at r = 5 cm, as compared with 0.46 at r = 4 cm. Similar results are found for other values of B_o. Therefore, since the ratio V_{oi}/V_E remains nearly constant between r = 4 to 5 cm for all B_o of interest, the measured V_{oi} data at r = 4 cm is converted for comparison with the computed V_{oi} by $V_{oi} \simeq qV_E$ where q can be determined as a function of B_o from Fig. 7c. The results are compared in Fig. 10 and show that the measured data for E_{ro} and V_{oi} in the column are compatible, and that Eq. 12 gives a good estimate of the V_{oi} in the high velocity region of the column.

The radial velocity u_r in the column is found by substituting for j_θ in the azimuthal component of Eq. 9

$$u_r(1 + V_{oi}/r\Omega_i) \simeq \left(\eta/B_o^2\right)\left(\rho V_{oi}^2/r - 2\partial p_i/\partial r\right) + (\mu_i/\Omega_i)\nabla_r^2 V_{oi} \qquad (13)$$

where $\Omega_i = eB_o/m_i$ and $V_{oi}/r\Omega_i$ represents a term caused by the Coriolis force. Inside the high velocity region, u_r is given by the difference between the velocities due to the ion rotational inertia and the ion viscous friction. The ions can escape from the plasma column when $u_r > 0$; using the approximation that $\nabla_r^2 V_{oi} \simeq -V_{oi}/\delta^2$ in Eq. 13, the condition that $u_r > 0$ reduces to the inequality

$$(\delta/\lambda_c)^2 \geq \sqrt{(m_i/m_e)}\,(r\Omega_i/V_{oi})\left(1 + \lambda_c^2/a_i^2\right)^{-1} \qquad (14)$$

which indicates that ions can escape from the potential well when both the velocity shear is large and the collisions between the ions and the electrons are frequent. The physical description of the ion escape mechanism is as follows: The thermoelectric potential at r = a drives an electron current through the slower and more massive ions. The electrons exert a frictional force on the ions through coulomb collisions that raises the ions potential energy and drives them out of the confining potential well. During this process, heat is dissipated, but because of heat conduction to the end surfaces, both the ion and electron temperatures are presumed to remain constant, as suggested by diffusion calculations and indicated by Langmuir probe measurements. If the ratio (δ/λ_c) is smaller than the limit in Eq. 14, the ions fall back into the potential well and approach the Boltzmann distribution shown in Fig. 9; under such conditions, the losses are evaporative in nature, and only those ions with sufficient kinetic energy can escape from the potential well.

Using the data in Fig. 7d to estimate λ_c, the data in Fig. 7b to evaluate δ, and the data for V_{oi} in Fig. 7c, the ratio (δ/λ_c) is evaluated experimentally and compared in Fig. 11 with the prediction of Eq. 14 as a function of B_o. The measured ratio is always less than the prediction of Eq. 14 for all B_o shown, but the two values show closer agreement at smaller B_o. This latter result may be due to the presence of anomalous radial losses that act to increase the value of δ for $B_o < 300$ G. Considering the inherent assumptions in Eq. 14 and the possible experimental errors in the measurement of both δ and λ_c, the results in Fig. 11 indicate that

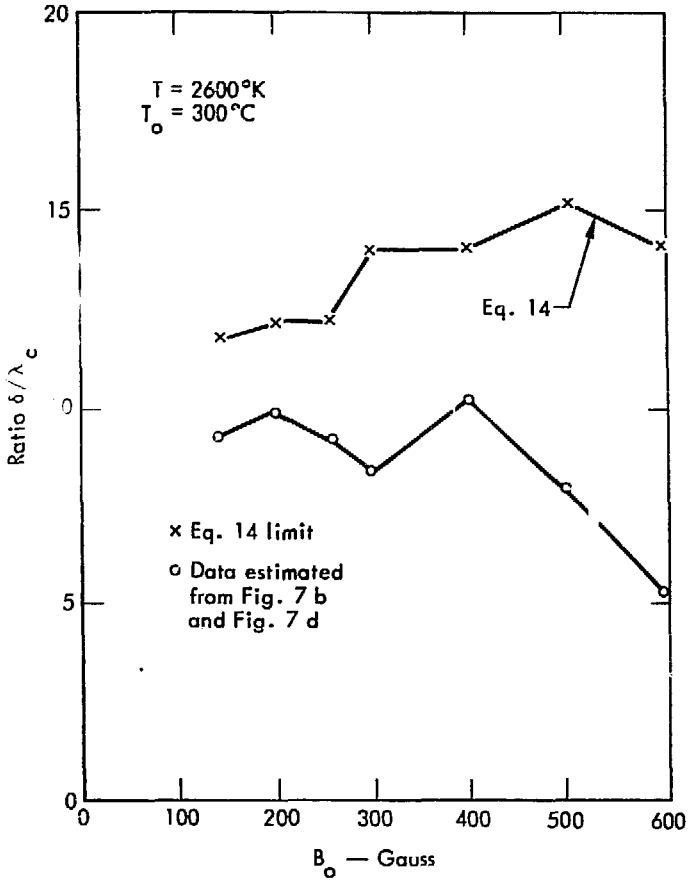

Fig. 11. Comparison between the predicted δ/λ_c from Eq. 14 and the measured data as a function of B_o in the column.

Eqs. 8 and 9 provide a good qualitative description of the ion confinement.

The above plasma model must also satisfy the density continuity equation which relates the n_o variation to the previously calculated velocity components. Since the derivation of Eq. 14 neglected the radial variation of n_o in comparison with the inertial and viscous forces in the velocity shear layer, the radial scale-length R of the $n_o(r)$ profiles is not necessarily the same as δ in the column. In the steady-state, the continuity relation $\nabla \cdot (n_o \underline{u}) = S$ in cylindrical coordinates becomes[53]

$$\partial(n_o u_r)/\partial r + n_o u_r/r + \partial(n_o u_z)/\partial z = S \qquad (15)$$

where the azimuthal dependence is neglected, and the value of u_r is given by Eq. 13. Outside of the high-velocity shear layer, $V_{oi} < V_{Ti}$, and the dominant term in Eq. 13 is $2\left(\eta/B_o^2\right)(\partial p_i/\partial r)$ which represents the classical resistive diffusion flux $n_o u_r \simeq -D\partial n_o/\partial r$ with $D = 2\eta KTn_o/B_o^2$.[53] Inside the shear layer, u_r is effectively the difference between the inertial and viscous drift.

The Eq. 15 may be reduced to a one-dimensional differential equation by replacing the longitudinal derivative by an effective loss rate. For $r > a$, the primary loss of ions occurs at the cold end plate, and an estimate of the loss rate ν_i is the reciprocal of the time necessary for the ions to transit the length of the column; $\nu_i \simeq V_{Ti}/L$. For $r < a$, the endplate loss is recombination at the hotplates, and the effective loss rate is approximated by $-\alpha n_o$ where α is the hotplate recombination coefficient. Employing

these two-ion loss-terms, Eq. 15 reduces to different forms in different radial regions of the column. For $r < a$, the previous results showed $V_{oi} < V_{Ti}$, and the flux is given by radial diffusion. If the ion source is assumed to be uniform at the hotplate and the losses due to ion recombination at the hotplates, Eq. 15 reduces to the form

$$r < a; \qquad n_o^2 '' + n_o^2 '/r - (2\alpha/D_o)n_o^2 = \text{constant} \tag{16}$$

where ' indicates the radial derivative and $D_o = D/n_o$ is independent of density. For $r > a$, the losses are due the ion sink at the cold endplate, u_r is again determined by diffusion, and there is no ion source. Under such conditions, Eq. 15 reduces to the form

$$r > a: \qquad n_o^2 '' + n_o^2 '/r - (2\nu_i/D_o)n_o = 0 \tag{17}$$

In the high-velocity region, $V_{oi} > V_{Ti}$, and u_r is determined by the difference in the centrigal force and viscous friction on the ions. In general, Eq. 15 becomes

$$(n_o u_r)' + (n_o u_r)/r - \alpha n_o^2 = \text{constant} \tag{18}$$

where u_r is given by Eq. 13. Of the above three equations, only Eq. 16 is solvable in terms of Bessel functions[21-22]; Eqs. 17 and 18 are both non-linear in the general case.

If the above set of equations could be solved analytically, the match of radial flux components on the inner side of the high velocity region would determine the value of α in the plasma, while matching flux components on the outer edge of the high-velocity region would determine the value of ν_i, provided that all other parameters are known. However, since an estimate of ν_i is already available, the radial scale-length of the density for $r > a$ could be numerically determined.

In order to solve for the radial scale-length at the column edge, the cylindrical surface at $r = a$ is approximated by a plane surface, and Eq. 17 is replaced by an equation whose solution is proportional to $\exp(-r/R)$ where $R^2 = D/\nu_i$. At $B_o = 150$ G, $D \simeq 3.0 \times 10^3$ cm^2/sec and $\nu_i \simeq 10^3$/sec; the resulting $R \simeq 1.7$ cm $\leq a_i$ is in accord with the results in Fig. 9. An approximate flux match is obtained by assuming the $n_o = n_i$ is constant for $r < a$ and setting $n_1 u_r \simeq -Dn_o'$ at $r = a$. The resulting equation is

$$n_1 u_r(a) = n(a)\sqrt{(\nu_i D)} \tag{19}$$

If u_r is taken to equal just the centrifugal component in Eq. 13 at $B_o = 150$ G, $u_r \simeq 10^3$ cm/sec, and the resultant $n/n_1 \simeq 0.6$. Comparing with the data in Fig. 9, $n(a) \simeq 4.0 \times 10^{10}$/cm^3 and n_{oo} $\simeq 10^{11}$/cm^3 so the $n/n_1 \simeq 0.4$, in good agreement with the prediction of Eq. 19. Considering that u_r is reduced by the presence of the ion viscosity in Eq. 13, the predicted ratio of n/n_1 is reduced below 0.6 in even closer agreement with the measured data. Therefore, the radial profile of n_o in Fig. 9 can be qualitatively

explained, and the quantitative agreement is excellent in view of the assumptions made.

D. Steady-State Plasma Loss Measurements

The previous section has introduced a plasma model which shows how the ions may escape from the potential well in the column. This present section is devoted to a study of the various possible loss processes that create a $u_r > 0$ and a quantitative comparison, where possible, with the total measured losses from the plasma.

The type of dominant loss mechanism that determines the plasma equilibrium may be qualitatively studied from the variation of the column density with magnetic field. Figure 12 shows a plot of n_{oo} as a function of B_o in the column. For $B_o < 300$ G, the result shows that $n_{oo} \propto B_o$ which has been interpreted to be characteristic of the presence of enhanced losses from the plasma. For $B_o > 500$ G, the density is nearly independent of B_o. Earlier work[45] has shown that a density independent of B_o is characteristic of hotplate ion recombination that does not depend on the value of B_o. For the intermediate range, 300 G $< B_o <$ 500 G, the results in Fig. 12 show that $n_{oo} \propto B_o^2$ which is consistent with the predicted losses due to classical resistive diffusion[38] across B_o. Therefore, the results shown in Fig. 12 indicate that at least three different loss processes are important to the plasma losses from the column within the experimental range of B_o.

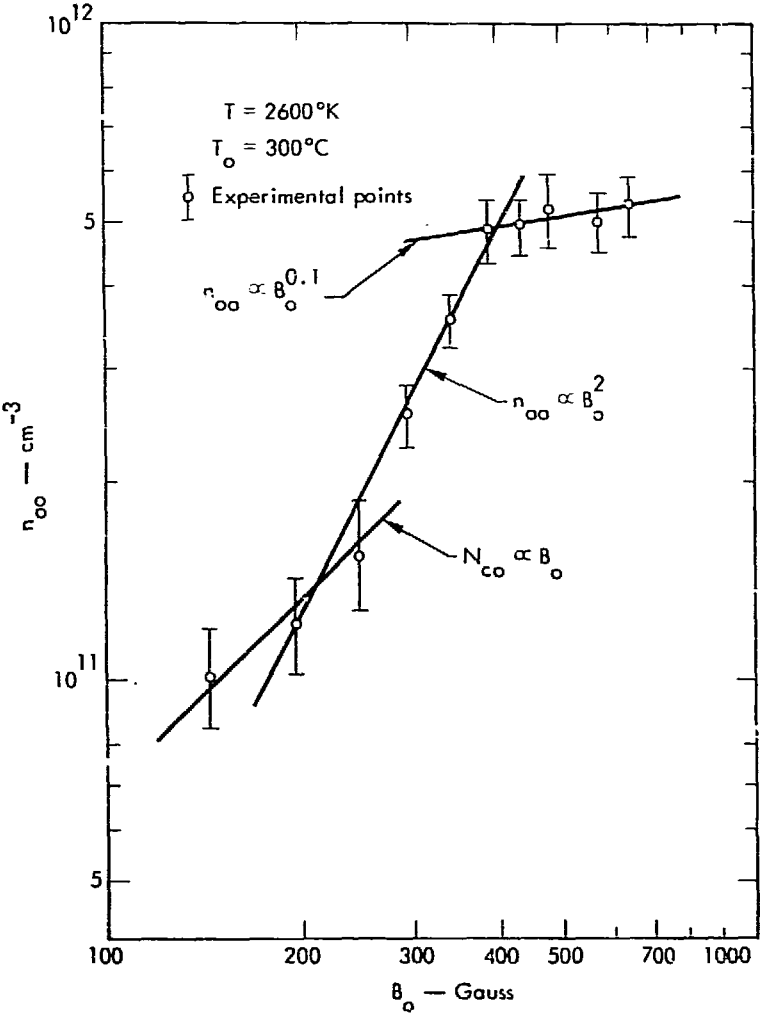

Fig. 12. Measured variation of n_{oo} as a function for B_o; the functional dependence on B_o indicates different types of losses are present.

In order to verify the above results, the total plasma loss is estimated from measurements of the total ion saturation current from the ionizer hotplate. As described in Chapter II, the total current I_o is recorded as a function of the midplane density n_{oo} for several different values of B_o between 150 and 600 G. Figure 13a shows the results for T = 2600°K and T_o = 300°C. For $n_{oo} > 10^{11}/cm^3$ ($B_o > 300$ G), the slope of the lines indicates that $j_o \propto n_{oo}^2$, while at lower densities ($B_o < 300$ G), the slope decreases and appears to indicate that $j_o \propto n_{oo}$. Earlier measurements of the losses in Q-machine plasma showed the same type of behavior and were interpreted to indicate the presence of enhanced plasma losses whenever $j_o \propto n_{oo}$.[18,46,47] Therefore, both Figs. 12 and 13a may be interpreted as an indication of enhanced plasma losses from the column for B_o between 150 G to 300 G.

Considering the hotplate losses in the presence of electron-rich sheaths, the equilibrium theory of von Goeler predicts[37]

$$sj_o \simeq \left(V_{Ti} V_{Te} s n_o^2\right) / [8Ri(T)La(T)] \qquad (20)$$

where all parameters are defined earlier. For a uniform distribution of j_o on the hotplate, Chapter II shows that $I_o/e \simeq \pi a^2 sj_o$, and this relation is plotted as the dashed line in Fig. 13a for comparison with the measured data. For $B_o > 300$ G, the data is close to the prediction of Eq. 20 in both slope and magnitude. Therefore, both Figs. 12 and 13a show that enhanced losses are probably absent from the plasma column at the larger values of B_o, in accord with measurements. The data in Fig. 13a also shows that based on Eq. 20, the plasma sheaths are electron-rich

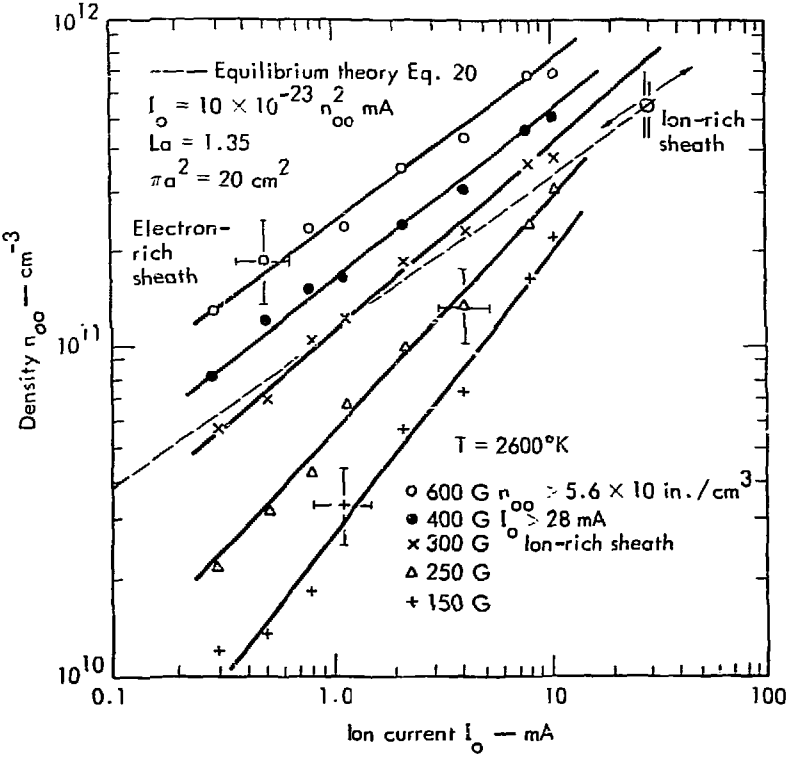

Fig. 13a. Measured dependence of n_{oo} as a function of I_o and B_o; the predicted n_{oo} from Eq. 20 is shown for comparison and indicates the hotplate sheaths are electron-rich for all data shown.

for all values of B_o shown. This last result agrees with the data shown in Fig. 8a which were discussed earlier.

An independent experimental check of the slopes indicated in Fig. 13a is provided by recording the variation of n_{oo} as a function of T_o^{-1}. Chapter II indicated that $I_o \propto j_o$ can be shown to be linearly proportional to the potassium vapor pressure P_v in the reservoir. Statistical mechanics shows that $\log(P_v) \approx -C/T_o$ + constant and this has been experimentally verified; for T_o between 400° and 700°K in potassium vapor, the measurements indicate that $C \simeq 3900/K°$.[56] Figure 13b shows a plot of $\log(n_{oo})$ as a function of T_o^{-1} for three values of B_o. The nearly linear variation shows that $\log(n_{oo}) \propto -C'/T_o$, and the data can be used to derive an empirical relation between n_{oo} and P_v. Since $I_o \propto P_v$, the data in Fig. 13a also determine a relation between n_{oo} and P_v which may be compared with the relationship determined from Fig. 13b. Defining the slope x by $\log(n_{oo}) \propto x\log(P_v)$, the slope in Fig. 13b is given by $x \simeq C'/C$. For B_o = 150 G, the measured value of $C' \simeq 2500/K°$ yields the prediction $x \simeq 0.65$; the corresponding slope in Fig. 13a is $x \simeq 0.75$, and the two results show good agreement. For B_o = 600 G, $C' \simeq 1950/K°$ and $x \simeq 0.5$ which is close to the value $x \simeq 0.4$ shown in Fig. 13a. Therefore, the two independent measurements in Fig. 13 both predict a significant difference in the slope of the $n_{oo} \propto j_o^x$ relation. For B_o < 300 G, $x \simeq 0.75$ which is closer to unity than the $x \simeq 0.5$ found for B_o > 300 G. The results again indicate that enhanced plasma losses are present for B_o < 300 G and are in agreement with the measurements in Fig. 12.

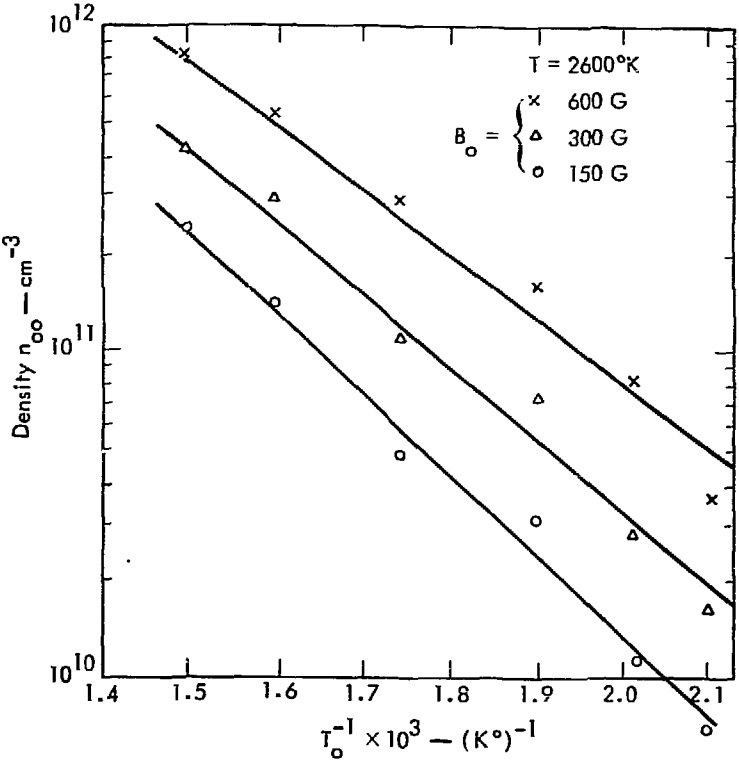

Fig. 13b. Measured variation of n_{oo} with changes in T_o^{-1}; the data provides a numerical check on the results in Fig. 13a.

Using the measurements in Fig. 13a, I_o/e provides a reasonable estimate of the total particle full-rate from the source hotplate; at B_o = 150 G, $I_o/e \simeq 4.0 \times 10^{15}$/sec for n_{oo} = 10^{11}/cm^3; while at B_o = 400 G, $I_o/e \simeq 6.0 \times 10^{16}$/sec for n_{oo} = 5.0×10^{11}/cm^3. When the wave amplitude is small at B_o = 150 G, the column density is observed to be increasing, while at B_o = 400 G, the column density remains constant except for the low-level density waves. Thus, the plasma "equilibrium" at B_o = 150 G is significantly different in nature from the equilibrium formed at B_o = 400 G. Since earlier measurements (see Figs. 12 and 13a) indicate than anomalous plasma losses occur only when $B_o < 300$ G, the case for B_o = 150 G is chosen as typical of this type of quasi-equilibrium state. In the absence of anomalous plasma losses for $B_o > 300$ G, the case with B_o = 400 G is taken as a typical example of the more conventional type of plasma equilibrium.

A semi-quantitative study of the quasi-equilibrium state at B_o = 150 G is possible through the use of the integrated form of the equation of continuity

$$\partial N/\partial t + 2\pi r \int_o^L F_c(r,z)dz + 2\pi \int_o^r F_r(r)rdr = I_o(r)/e \qquad (21)$$

where $N = 2\pi\int_o^L\int_o^r r\bar{n}(r,z)rdrdz$ is the total number of particles in the plasma column with $\bar{n}$ as the column density in the absence of plasma waves, F_c is the loss-flux from classical diffusion across B_o, F_r is the ion recombination flux at the hotplates and is approximated by the classical relation given in Eq. 20, and a measure I_o from the full hotplate is given in Fig. 13a.

Equation 21 may be greatly simplified if a first approximation is made in which $\bar{n}$, F_c, and F_r are replaced by mean values that are independent of the coordinates r and z; the resulting equation is written in the following normalized form:

$$(\partial\langle\bar{n}\rangle/\partial t)/\langle\bar{n}\rangle + 2\langle F_c\rangle/r\langle\bar{n}\rangle + \langle F_r\rangle/4L\langle\bar{n}\rangle = (I_o/e)/\pi a^2 L\langle\bar{n}\rangle \qquad (22)$$

where the brackets $\langle\rangle$ denote the mean quantities in the plasma, and the factor of 1/4 in the $\langle F_r\rangle$ term accounts for the fact that at B_o = 150 G, a field line is twice as far from the column axis at the midplane as at the hotplates. Figure 14a shows calculated radial profiles of the terms in $\langle F_c\rangle$, $\langle F_r\rangle$, and I_o for $r < a \simeq 5.1$ cm at the midplane; the losses are all calculated for the time $t = t_o$ indicated on the density waveform at $r \simeq 3$ cm. The indicated loss from classical diffusion is substantially larger than the ion recombination loss at the hotplates.

Using data in Fig. 14a, the predicted normalized loss-rate from Eq. 22 is calculated and plotted as a function of radius in Fig. 14b; measured loss-rates are calculated from the slope at $t = t_o$ of density waveforms similar to that shown in Fig. 14a and plotted in Fig. 14b for comparison with the predicted values. The results indicate that the theory given by Eq. 22 is in qualitative accord with the measured data, and the quasi-equilibrium state of the plasma at B_o = 150 G is a combination of the losses from classical diffusion and ion surface recombination at the hotplates.

For the case when B_o = 400 G, the column density does not change with time except for the low-level fluctuations that are present. Under these conditions, Eq. 21 is still valid, but the term $\partial N/\partial t$ is zero. Therefore, the plasma equilibrium is a

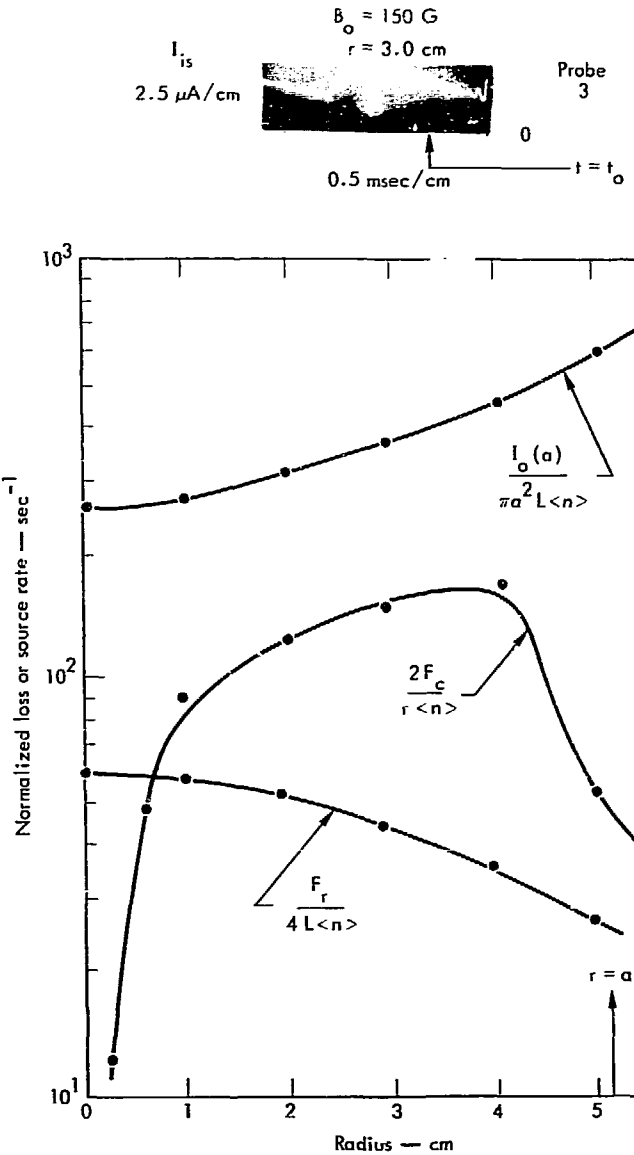

Fig. 14a. Experimental radial profiles of the individual loss terms that are defined by Eq. 22 at $t \simeq t_o$ and $B_o \simeq 150$ G.

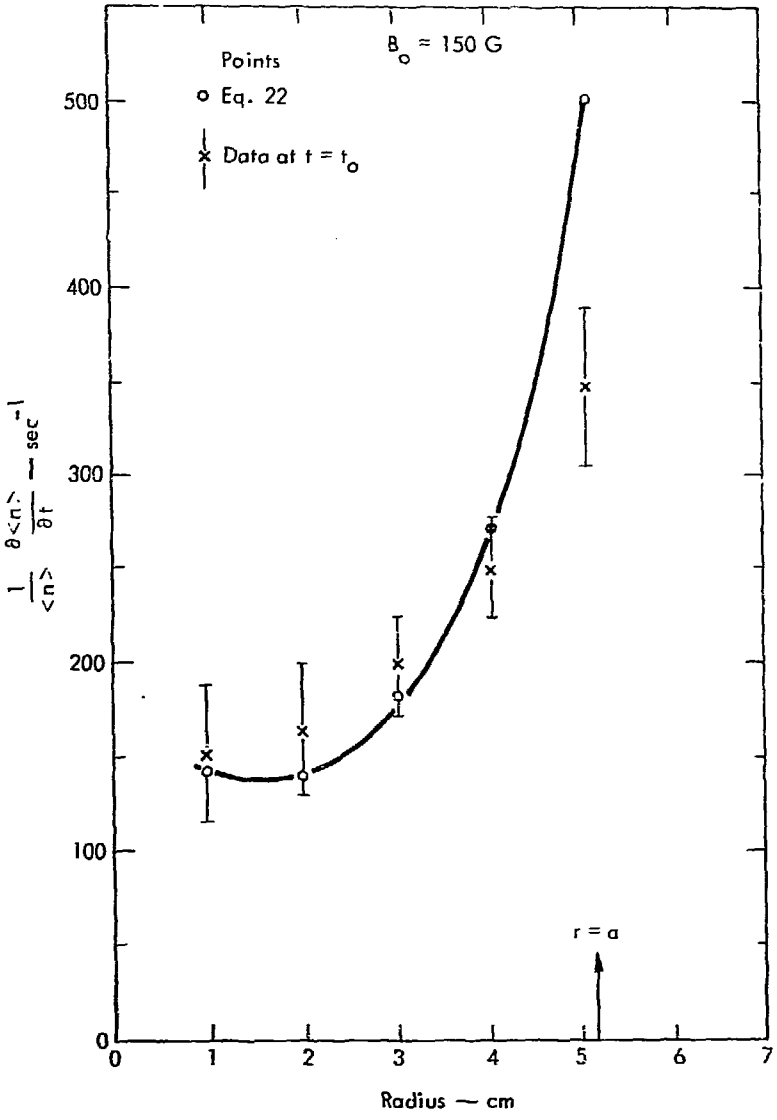

Fig. 14b. Comparison between the predicted loss-rate from Eq. 22 and the measured loss-rate, at $t = t_o$ in Fig. 14a, for B_o = 150 G.

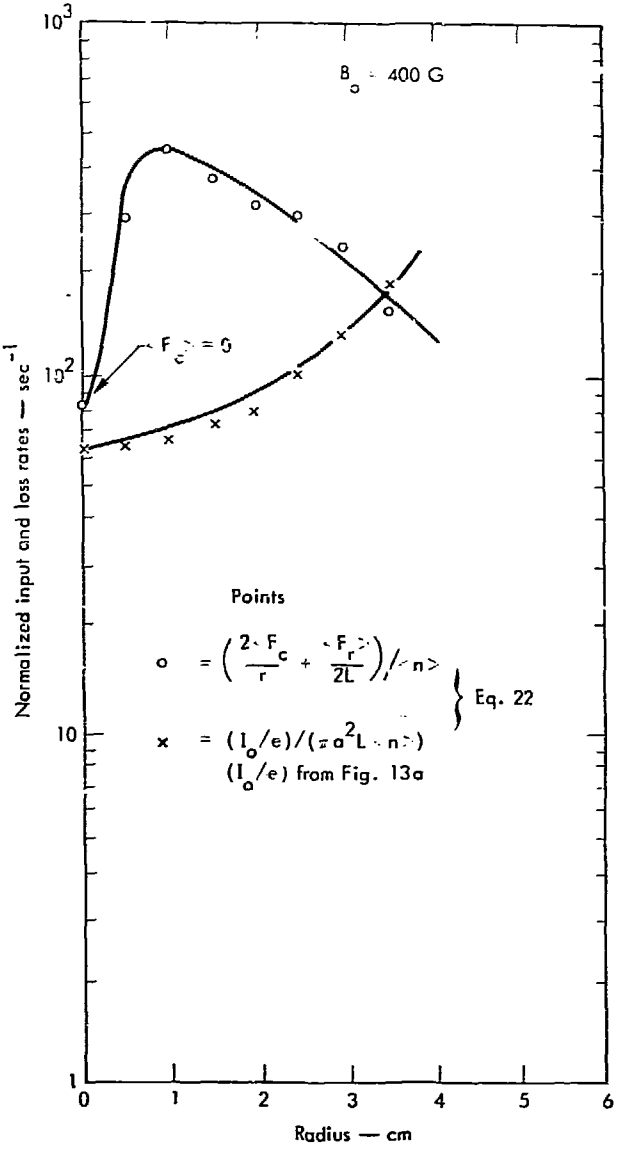

Fig. 14c. Comparison between the radial profiles of the total measured loss-rate and the plasma fill-rate I_o/e for B_o = 400 G; the time variation of the density is zero for this comparison.

balance of the diffusion and recombination losses against the input of ions from the source hotplate. Making the same assumptions as for the case at B_o = 150 G, the Eq. 21 again reduces to Eq. 22 with $\partial\langle\bar{n}\rangle/\partial t = 0$. The factor multiplying $\langle F_r \rangle$ is now taken to be 1/2 in accord with the higher value of B_o with respect to the magnetic field at the hotplates. Figure 14c shows the computed radial profile of the sum of the two loss terms in comparison with the normalized input-rate to the column; the loss calculations do not refer to a specific time as for the case at B_o = 150 G. The calculations indicate that the predicted losses greatly exceed the input in the column center, but near $r \simeq a$, the input and loss rates are in balance. This result indicates that the particles are lost most rapidly near the column axis and replaced near the column edge. A quantitative balance could be achieved if the radial density profile were flatter in the column center and the input particle rate were doubled; both of these possibilities are within the range of experimental error present in the measurements. Therefore, choosing the best combination of the probable errors in the input and loss terms, the continuity equation in the form of Eq. 22 with $\partial\langle\bar{n}\rangle/\partial t = 0$ is able to qualitatively explain the plasma equilibrium in the column for B_o = 400 G.

The use of the continuity equation with the radial flux determined by classical diffusion neglects the radial flux due to the centrifugal drift and the ion viscosity in the high-velocity region near the column edge. Since the discussion in Section C of this chapter showed that the thickness δ of the high-velocity region is

determined primarily by the balance between the viscous and centrifugal forces (see Eq. 14), the net radial flux out of the column is determined by the classical diffusion term in Eq. 13, and the use of Eq. 21 for the entire plasma column is justified.

This present section has dealt with the flux balance in the column under steady or quasi-steady conditions. However, anomalous radial losses of a periodic nature are clearly observed for $B_o < 300$ G and are believed to be caused by $\underline{E}x\underline{B}$ radial convection by unstable plasma perturbations that propagate azimuthally around the column. The origin and characteristics of these waves is the subject of the next chapter.

IV. MEASUREMENTS OF PLASMA OSCILLATIONS

A. General

The measurements presented in Chapter III are concerned with the equilibrium condition of the plasma column, and the results consistently indicate the presence of enhanced or anomalous plasma losses for B_o between 150 to 300 G. For this range of B_o, the dominant plasma waves are azimuthally propagating perturbations that may exhibit non-linear and periodic time-growth for special conditions. The enhanced plasma losses are believed to be closely connected with the non-linear time-growth of the waves. For $B_o \geq 300$ G, the losses are independent of time and may be accounted for by the purely classical processes, discussed in Chapter III. For this higher range of B_o, the dominant plasma waves are harmonically related perturbations that propagate azimuthally with a saturated amplitude and do not exhibit any long-term time-growth. Measurements of the wave characteristics for each range of B_o indicate that the plasma waves probably arise from entirely different sources of instability in the column.

Plasma waves were detected in the earliest experiments with Q-machines and their origin has been the subject of controversy. D'Angelo and Motley[24] detected waves that they identified as electrostatic ion cyclotron waves; Decker[25] and Lashinsky[26] measured low-amplitude waves that each identified as the electron-drift mode; and Buchelnikova[27] identified the waves in her experiment as the "universal" or collisionless

drift mode predicted by Rudakov and Sagdeev.[2] Grieger[50] pointed out that all of the above experiments neglected the effects of an equilibrium electric field that can reverse the observed direction of wave propagation in the plasma column. Hartman and Munger[28] showed that when the $\underline{E}\times\underline{B}$ drift opposed the diamagnetic drift, the observed wave propagation in the laboratory was reversed from the direction of propagation in the plasma rest-frame. Including the electric field drift, later experiments[29, 30] showed that the waves were probably collisional drift waves. The first conclusive experimental evidence for the propagation of the collisional drift waves was given by Hendel et al.[15] which compared theory and experiment under controlled conditions.

Experiments of Hartman and Munger using an internally generated radial electric field showed that plasma waves could arise from large radial velocity shear in the column.[30] Recent work by Kent et al.[57] and by Perkins and Jassby[32] shows that oscillations observed to occur near the hotplate edge are probably due to a modified form of the hydrodynamic Kelvin-Helmholtz instability. Other instabilities that can arise in a rotating plasma column include the ion-cyclotron drift mode, the gravitational interchange mode due to magnetic field curvature, and the centrifugally driven interchange mode.[58]

The wave measurements are conducted for the following range of time-average plasma parameters: densities n_o between 10^{10} and $10^{12}/cm^3$, hotplate temperatures T (both plates equal) between 2300° and 2700°K, potassium oven temperatures T_o between 200° and 400°C, and midplane magnetic fields B_o between

150 and 650 G. However, the majority of the measurements are made for $T_e \sim 2600$ K and $T_o \sim 300$°C because of the repeatability of the results. The waves are studied in two groups that are distinguished by the range of B_o in which they are predominant.

B. Group I Oscillations

The group I waves consist of the three harmonically related, low-level saturated modes that are predominant for $B_o > 300$ G. In the general case, all three modes propagate simultaneously in time with different amplitudes, but sometimes only a single nearly sinusoidal wave (in time) is observed. Note: In all oscilloscope traces shown in the present paper, time goes from right to left on the abcissa. Figure 15a shows the frequency spectrum of the group I waves, and Fig. 15b shows the corresponding azimuthal density correlations of the individual modes. Assuming a density perturbation proportional to $\exp(im\theta)$, the data in Fig. 15 shows an m=2 mode with a measured frequency $f_2 = 13$ kHz; an m=3 mode with $f_3 = 19$ kHz; and an m=4 mode with $f_4 = 25$ kHz. Thus, the modes are separated by approximately 6 kHz, and the predicted m=1 should be at $f_1 = 6$ kHz; the m=1 mode is not observed in the group I waves. All modes are observed to propagate in the direction of the $\underline{E}x\underline{B}$ drift in the column, but this must be corrected for the plasma column rotation.

Since $f_m \propto V_p$, the measured phase velocity V_p is also modified by the column rotation. Figure 16a presents the radial profile of V_p at the peak amplitude of the m=2 mode at $B_o = 300$ G; Fig. 16b shows similar results for $B_o = 600$ G. Since $a_e \ll R$ in the plasma, the electron drift velocity V_e is well approximated by

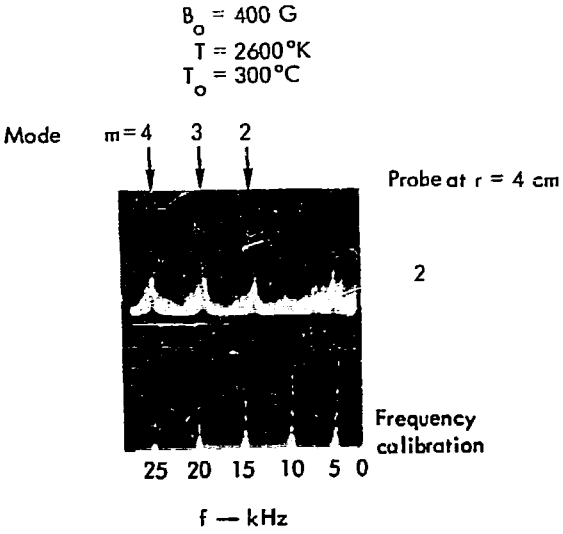

Fig. 15a. Frequency spectrum of the group I oscillations for $B_o \simeq 400$ G, $T \simeq 2600°K$, $T_o \simeq 300°C$, and probe at $r \simeq 4$ cm in the plasma.

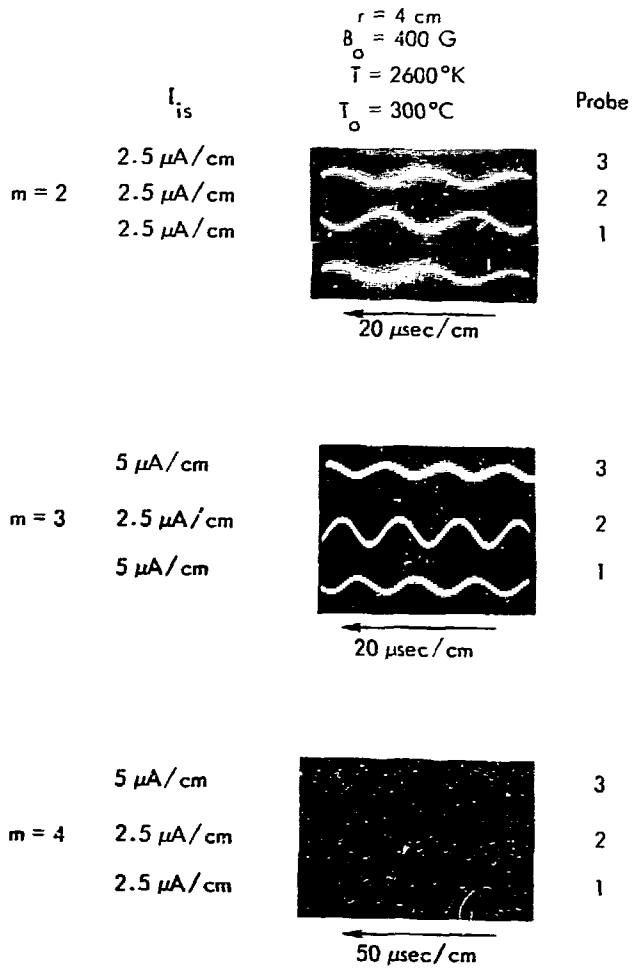

Fig. 15b. Associated azimuthal density correlations for the modes indicated in Fig. 15a; the probes are located as in Fig. 3.

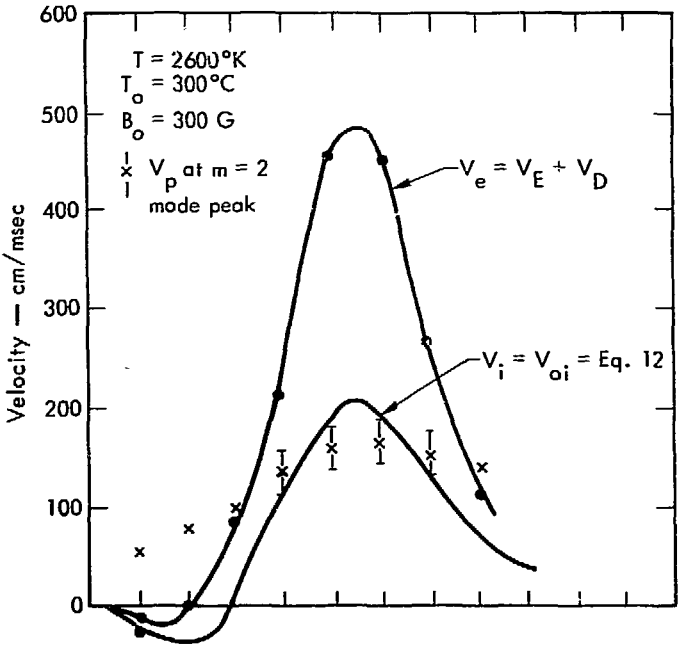

Fig. 16a. Comparison between the m=2 mode radial profiles of V_p and the calculated profiles of V_e and V_i for $B_o \approx 300$ G, $T_o = 300°C$, and $T \approx 2600°K$; V_p is computed from azimuthal correlation data, $V_e = V_E - V_D$, and $V_i \approx V_{oi}$ is computed from Eq. 12.

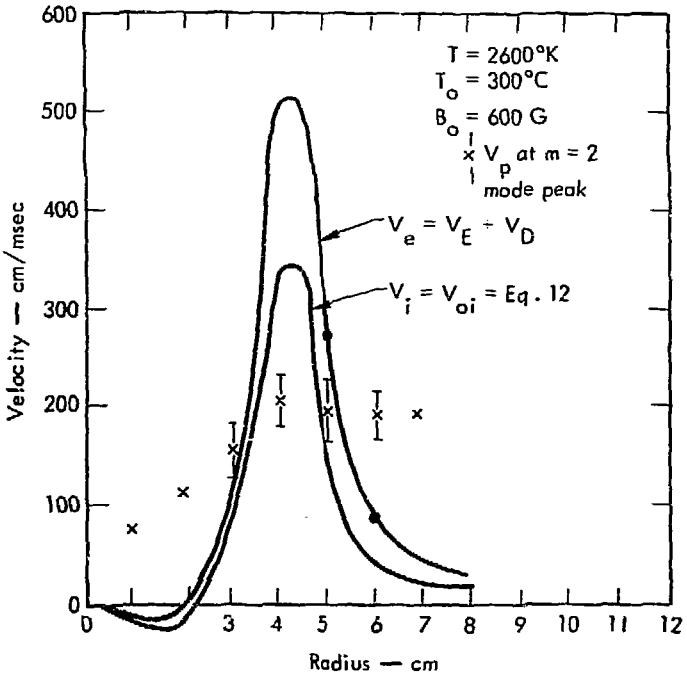

Fig. 16b. Repeat of the measurements in Fig. 16a for B_o = 600 G.

$V_e \simeq V_E + V_D$. For the ions, $a_i \sim R$, and the ion drift velocity is approximated by V_{oi}. Using the results in Fig. 10, V_{oi} is calculated from Eq. 12 and plotted on Fig. 15 together with V_e for comparison with the recorded values of V_p in the plasma. At both values of B_o shown, the m=2 waves are nowhere synchronous with the electrons, but the oscillations appear to propagate nearly synchronously with the ions for the range $r \simeq 3$ to 5 cm within the plasma column. This result eliminates the electron drift oscillations as the source of the observed modes. Since the plasma is also collision dominated, the last result also eliminates the "universal" instability as the source of the waves.[15]

Figure 17 shows the axial density correlation for both B_o = 300 G and B_o = 600 G. From the lack of phase shift between the fixed midplane probe and the probe at 40 cm toward the second hotplate, the upper limit on $k_\parallel$ is approximately $\pi/10L$. This is reduced to $\pi/5L$ by the minimum-detectable phase shift and the probable error in the probe positioning. However, a plot of relative wave amplitude $\tilde{n}/n_o$ along the vessel axis shows that approximately a quarter-wavelength fits between the hotplates, and $k_\parallel = \pi/2L \pm \pi/5L$ which indicates a possibly line-tied flute mode instead of a drift wave. Drift waves usually show a half-wavelength between the hotplates.[15]

Further evidence that the waves are flutes is provided by correlation measurements between the wave amplitude $\tilde{n}$ and the perturbed potential $\tilde{\phi}$. Figure 18 shows the $\tilde{n}$ - $\tilde{\phi}$ correlations for B_o = 400 G at r = 4 cm and B_o = 600 G at r = 4 cm. According to Chen,[59] the indicated phase shift of nearly 180° is typical of a flute mode rather than a drift mode. In addition, computing the

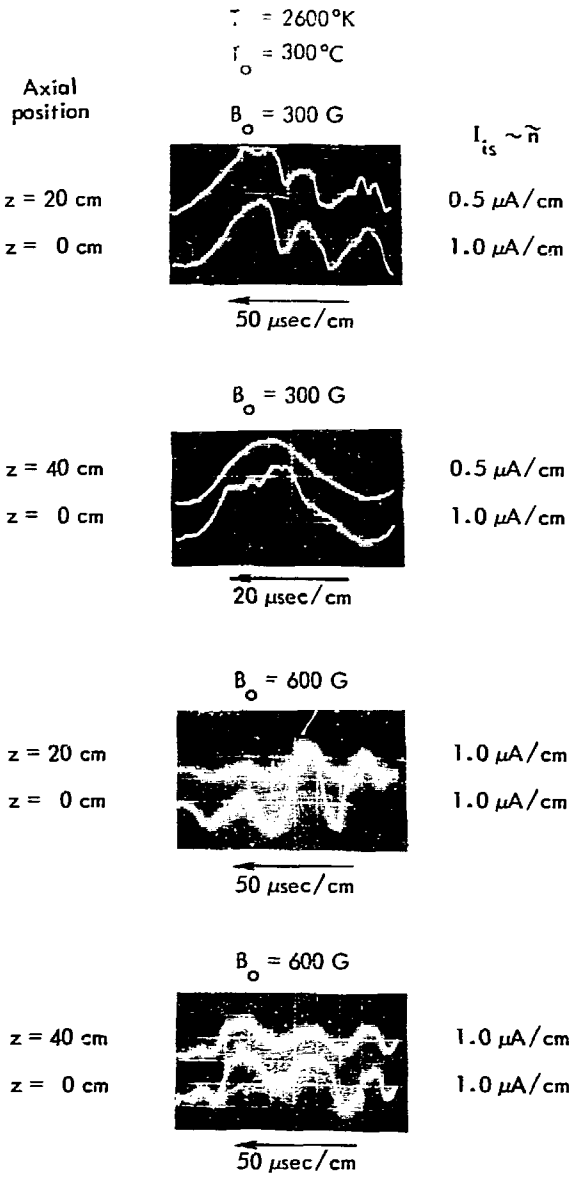

Fig. 17. Axial density correlations at z = 0, 20, and 40 cm for $B_o \simeq 300$ G and for $B_o \simeq 600$ G; traveling waves are absent from the column.

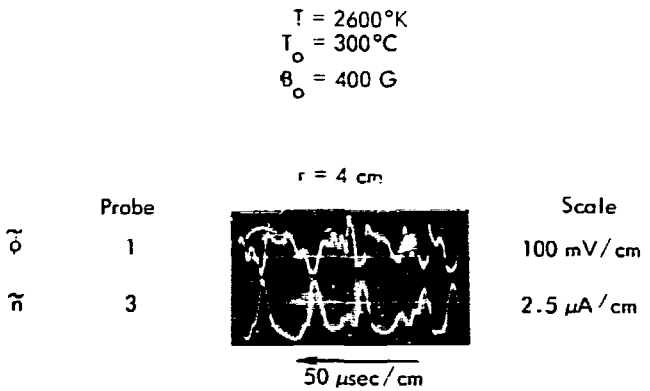

Fig. 18. Correlations between $\tilde{n}$ and $\tilde{\phi}$ at r = 4 cm, T = 2600°K, and T_o = 300°C for B_o = 300 G and for B_o = 600 G; the waves are 180° out of phase.

experimental ratios $\tilde{n}/n_o$ and $e\tilde{\phi}/KT$ shows that $\tilde{n}/n_o \ll e\tilde{\phi}/KT$ which is not indicative of a drift wave. A phase shift of 180° between $\tilde{n}$ and $\tilde{\phi}$ could indicate either an ion cyclotron drift wave with $k_{||} = 0$[30] or a Kelvin-Helmholtz instability.[32] Physical considerations show that when ν_{ii} becomes comparable to the wave growth-rate γ, the resonance required for the ion cyclotron drift mode cannot be maintained, and the mode is probably absent in the present experiment.

In the theory of Perkins and Jassby,[32] the Kelvin-Helmholtz waves require that the potential perturbation show a rapid 180° phase shift with radius within the shear layer. In the present work, the radial change in the phase of $\tilde{\phi}$ is not available. However, the radial correlations of $\tilde{n}$ show that the phase of $\tilde{n}/n_o$ remains nearly constant within the shear layer at $B_o = 600$ G, and therefore the radial variation of the $\tilde{n}$ - $\tilde{\phi}$ correlations should show the 180° phase shift. Figure 19 shows the $\tilde{n}$ - $\tilde{\phi}$ correlation at r = 3 cm (inner side of the shear layer) and r = 5 cm (outer edge of shear layer) for $B_o = 600$ G and indicates that $\tilde{\phi}$ undergoes a sign change within the velocity shear layer, in accord with the Perkins-Jassby theory for the Kelvin-Helmholtz instability. The fact that $\tilde{n}/n_o$ does not show a phase change with radius in the shear layer is also in accord with this theory. Therefore, it appears that the observed waves are probably due to the velocity shear at the edge of the hotplate.

If the observed plasma waves are caused by a form of the Kelvin-Helmholtz instability, the maximum wave amplitude should occur close to the maximum value of $\partial V_{oi}/\partial r$ in the column. Figure 20a shows radial profiles of the computed quantities $\partial V_E/\partial r$

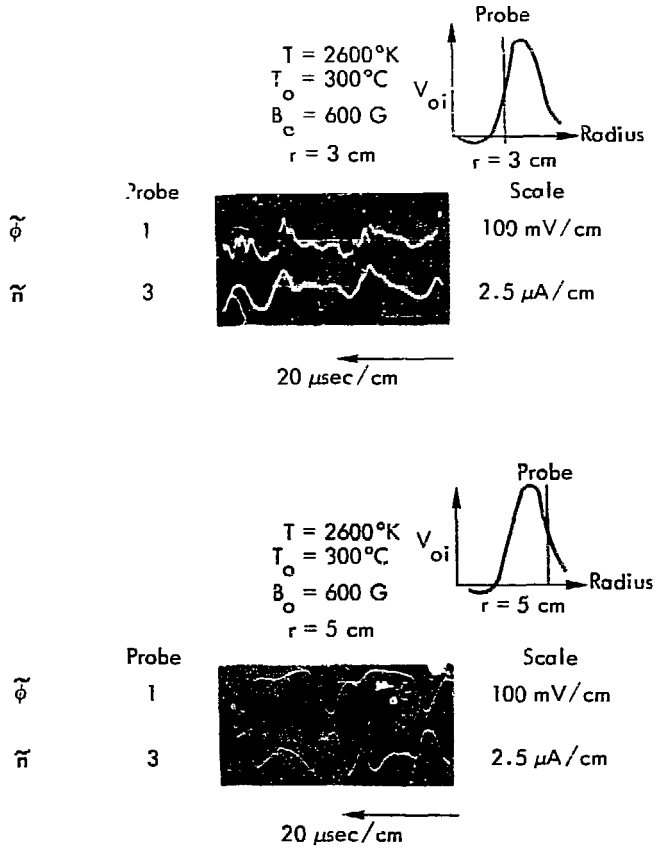

Fig. 19. Comparison of the phase relation between $\tilde{n}$ and $\tilde{\phi}$ with the probe at the inner and outer boundaries of the high-velocity annulus. For $B_o \approx 600$ G, the phase changes by 180° from r = 3 cm to r = 5 cm.

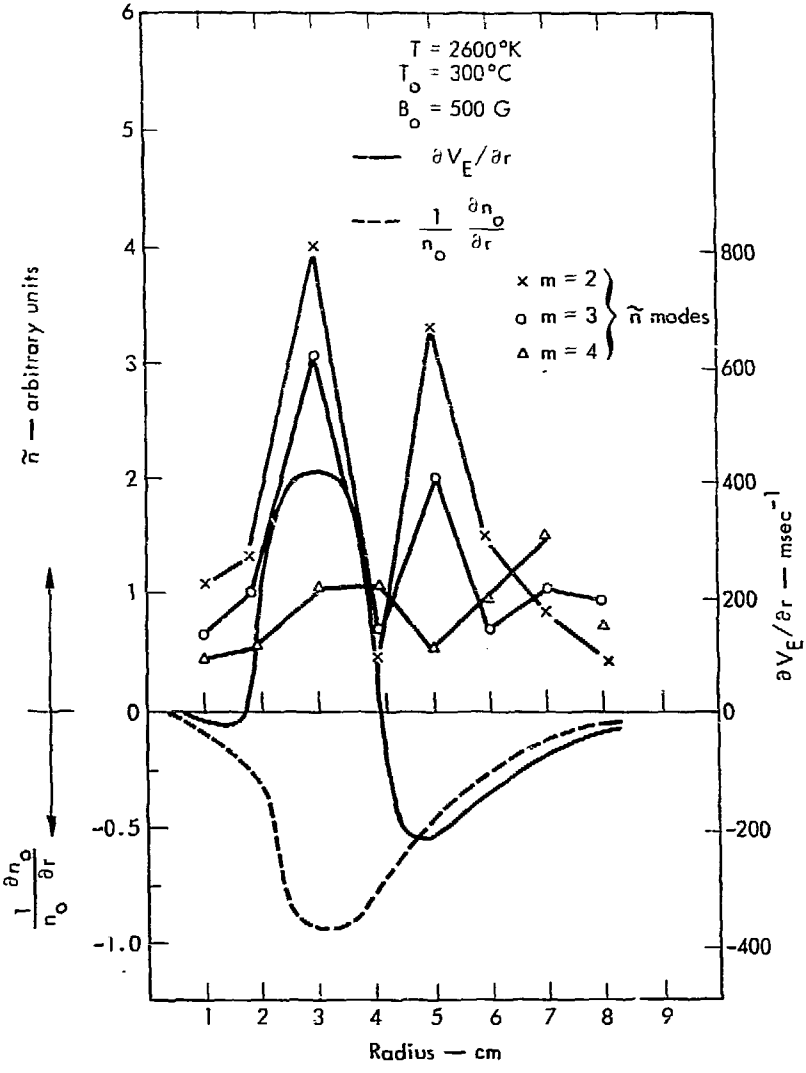

Fig. 20a. Radial profiles of $\tilde{n}$, $\partial n_o/n_o \partial r$, and $\partial V_E/\partial r$ for $B_o \simeq 500$ G, $T_o \simeq 300°C$, and $T \simeq 2600°K$; the two maxima of $\tilde{n}$ coincide with the maxima of $\partial V_E/\partial r$ in the column.

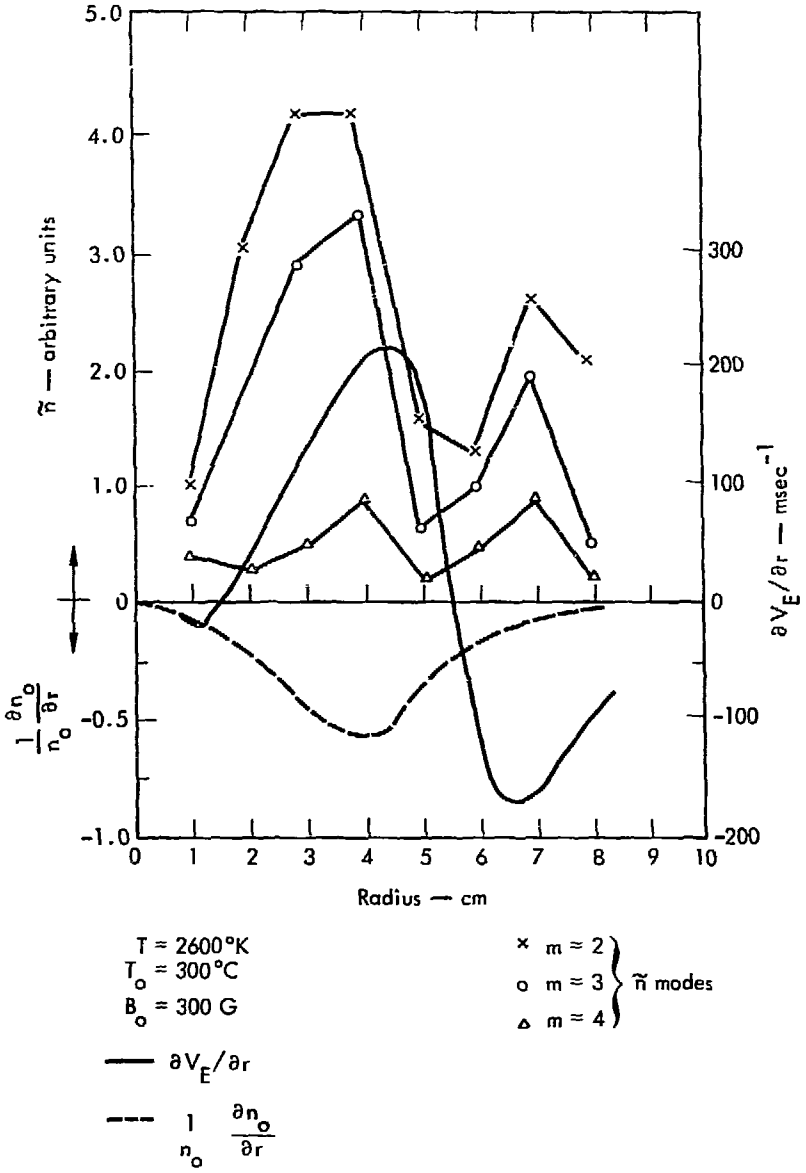

Fig. 20b. Repeat of the measurements in Fig. 16b for B_o = 300 G; the maxima of $\tilde{n}$ coincide with those for $\partial V_E/\partial r$.

and $-\partial n_o/n_o\partial r$, together with measured data of $\tilde{n}$ for m=2, 3, and 4 modes at B_o = 300 G. The same plot is repeated for B_o = 500 G in Fig. 20b. On either radial edge of the velocity shear layer at both B_o = 300 G and 500 G, the wave amplitude $\tilde{n}$ appears to peak near the radial position where the magnitude of $\partial V_E/\partial r$ is a maximum. On the inner edge, the position of the maximum radial density gradient coincides with that for the maximum velocity shear, and the waves could be excited by either the Kelvin-Helmholtz instability or the interchange instability. However, on the outer edge of the high-velocity region in the plasma, the waves appear to be excited and localized only by the transverse velocity shear. Therefore, it is highly probable that the waves which are localized at the inner edge of the velocity layer are also caused by the velocity shear and not by the radial density gradient, so that the origin of the waves clearly involves the study of a Kelvin-Helmholtz type of instability in the plasma.

The recent work by Perkins and Jassby presents detailed calculations of the transverse velocity shear instabilities in a rotating plasma column. Their general model assumes a low-β isothermal, cylindrically symmetric plasma confined in a uniform magnetic field. Finite Larmor radius terms are neglected, as well as radial classical diffusion and ion motion parallel to B_o. The velocity V_E is assumed to be less or comparable in magnitude with the ion thermal velocity V_{Ti}, the effect of $k_{\parallel} \neq 0$ is included, and ion viscosity is considered as a perturbation.

This model is generally applicable to the present work; the magnetic field may be considered as nearly uniform, radial diffusion is negligible in establishing the plasma equilibrium in

the high-velocity layer, but $V_{E} > V_{Ti}$ in this layer. However, the discussion in Chapter III showed that the balance between the ion viscous shear and the centrifugal force in the plasma establishes the thickness δ of the high-velocity region so that the steady losses from the column are still effectively controlled by classical diffusion. Therefore, the calculations made by Perkins and Jassby should lead to qualitative understanding of the velocity shear in the present experiment.

The particular plasma model of interest assumes a Gaussian "jet" profile for $\omega_E = -mE_{ro}/rB_o$ in the column and a density $n_o \propto \exp(-r^2/r_o^2)$. Figure 21a shows the comparison between the model and the experimental data for $B_o = 600$ G. The "jet" velocity profile is characteristic of a localized potential drop in the plasma and is well suited for the present experiment. In order to derive simple analytical expressions for the wave stability, Perkins and Jassby extend the hydrodynamical calculations of Drazin and Howard[61] to the case of the low-β plasma. The calculations are simplified for the conditions $R > r/m$ and $\Sigma r^2/a_i^2 m^2 \omega E \ll 1$[32] where $\Sigma \propto k_\parallel^2$; the first condition states that the transverse wavelength is less that the radial density scale-length in the column, while the second inequality excludes resistive drift waves as a source of the observed oscillations and appears to be satisfied for all m-numbers in the present experiment. The elimination of the resistive drift waves is in accord with the measurements of V_p, $k_\parallel$, and the $\tilde{n}$-$\tilde{\phi}$ correlations that were discussed earlier.

For the plasma model illustrated in Fig. 21a and the above conditions, Perkins and Jassby derive a quadratic dispersion relation whose coefficients are given in their Eqs. 36-38. Using

$T = 2600°K$

$T_o = 300°C$

$B_o = 600$ G

$\exp(-(r-c)^2/2d^2)$
$c = 4$ cm, $d = 0.71$ cm

× Measured $n_o(r)$
o Measured $V_{oi}(r)/r$

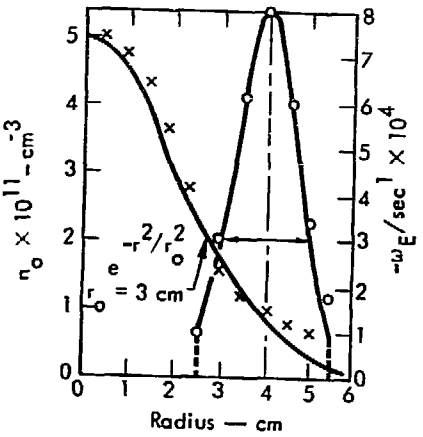

Fig. 21a. Experimental radial profiles of n_o and $-\omega_E$ and their theoretical approximations for application of the Perkins-Jassby theory. $B_o = 600$ G, $T_o = 300°C$, and $T \simeq 2600°K$.

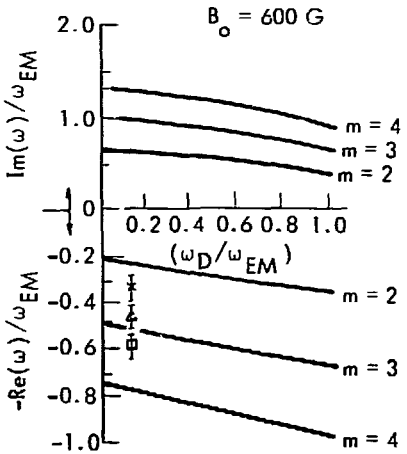

Fig. 21b. Calculated normalized frequencies and growth-rates for the velocity shear waves in the model of Fig. 21a; measured frequencies for the m=2, 3, and 4 modes at $B_o \approx 600$ G are shown.

these coefficients with $\Sigma \propto k_{\parallel}^2 = 0$, stable plasma oscillations satisfy the inequality

$$(in/r)\left[W_1 - mr\omega_D/(m^2 - 1)\right]^2 > 2(1 - 1/m^2)^{-1}\left[1 + r^2/r_o^2(m^2 - 1)\right] \times (W_2 - \omega_D W_1) \quad (23)$$

where $W_1 = \int_{r_a}^{r_b} \omega_E dr$ gives the effective ion rotational velocity in the high-velocity region, $W_2 = \int_{r_a}^{r_b} \omega_E^2 dr$ is proportional to the mean ion rotational inertia in the "jet" velocity profile, $\omega_D = mV_D/r$ is the electron diamagnetic frequency (assumed to be constant in the high-velocity region), and r_a, r_b are the radial limits of the shear region. The term $\left[W_1 - mr\omega_D/(m^2 - 1)\right]^2$ is proportional to the rotational kinetic energy in the column, while the term $(W_2 - \omega_D W_1)$ is proportional to the centrifugal forces in the high-velocity annulus. Therefore, Eq. 23 states that only those modes whose ratio of centrifugal force to rotational kinetic energy is sufficiently large, are driven unstable by the velocity shear.

Consideration of the full dispersion relation with m=1 shows that Eq. 23 breaks down; for $k_{\parallel} \neq 0$, the m=1 mode is either stable or not propagating while for $k_{\parallel} = 0$, the m=1 mode does not propagate in the column. Therefore, the observed absence of the m=1 mode from the group I waves in the present experiment is in accord with the above theory.

Based upon the conditions $m \neq 1$, $r \sim r_o$, $W_2 > \omega_D W_1$, and the inequality $W_1 \ll V_D$ which is not satisfied in the present work, Perkins and Jassby derived their[32] Eq. 39 and concluded that the short wavelength modes are unstable, but the long

wavelength modes are stabilized by finite Larmor radius effects outside the shear layer. These predictions are just the reverse of the experimental observations in the present work.

The discrepancy appears to be the simplification of Eq. 23, based upon the inequality $W_1 \ll V_D$. For the conditions $m \neq 1$, $r \sim r_o$, $W_2 > \omega_D W_1$, and $W_1 \gg V_D$, Eq. 23 is reduced to the approximate inequality, $m/r > 2W_2/W_1^2$ which states that the long wavelength modes are unstable while the short wavelength modes remain stable, in agreement with the experimental observations. Therefore, for the present experimental conditions, the theory leading to Eq. 23 can account for both the absence of the m=1 mode and the presence of the lower m-number modes.

For the numerical model illustrated in Fig. 21a, the integrals W_1 and W_2 are evaluated from tabulated values of the standard Error Function.[35] Using r_a = 2.5 cm, r_b = 5.5 cm, d = 2 cm, and c = 4 cm in Fig. 21a, Eq. 23 predicts that all modes with $m/r > 1.1$ are stable; thus at r = 4 cm, all modes with $m > 4.4$ are stable. With the approximations used in the model, this numerical result is probably fortuitous, but the result shows remarkable agreement with the measured results. An occasional indication of the m=5 mode is observed at the column edge, but generally all modes above m=4 are absent in the experiment. Therefore, the stability conditions given by the Perkins and Jassby plasma model are in complete accord with the observed plasma waves.

For the unstable modes, the real eigen-frequencies are computed from the expression ($k_\parallel = 0$)[32]

$$\mathrm{Re}(\omega) \approx \left[(m^2 - 1)W_1 r^2 - m\omega_D r\right](2m/r)\Gamma^{-1}(r, r_o) \qquad (24)$$

where $\Gamma(r, r_o) = \left[1 + r^2/r_o^2(m^2 - 1)\right]$ and all of the parameters have been previously defined. The corresponding imaginary eigen-frequencies are computed approximately from[32]

$$\left[\mathrm{Im}(\omega)\right]^2 \approx \left(\frac{m^2 - 1}{4m^2}\right)\left[\frac{2m}{r} W_2 \Gamma - \left(\frac{m^2 - 1}{r^2}\right)W_1^2\right]\Gamma^{-2}(r, r_o) \qquad (25)$$

Figure 21b shows a plot of Eqs. 24 and 25 as a function of the ratio ω_D/ω_{EM} where ω_{EM} is the maximum value of ω_E in Fig. 21a. Measured values of f_m as a function of B_o at radii within the velocity profile are shown in Fig. 22. In order to compare theory and experiment at B_o = 600 G, f_m must be converted to the wave frequency ω in the plasma rest-frame by the relation $\omega = 2\pi f_m - mV_{oi}/r$. The result at B_o = 600 G is plotted in normalized form in Fig. 21b for m=2, 3, 4 with a $\omega_D/\omega_{EM} = 0.125$. The error bars represent the error in both f_m and V_{oi} in the column, and the results indicate qualitative agreement between the theoretical model in Fig. 21a and the measured frequencies at B_o = 600 G. Since non-linear plasma processes balance the growth-rate of the waves and produce a saturated amplitude for all of the modes,[62] no experimental measurements of the linear growth-rates are available to compare with the computed values in Fig. 21b.

According to the work of Perkins and Jassby, the Kelvin-Helmholtz instability has the following characteristics for a thin velocity shear layer. The wave amplitude maximum occurs

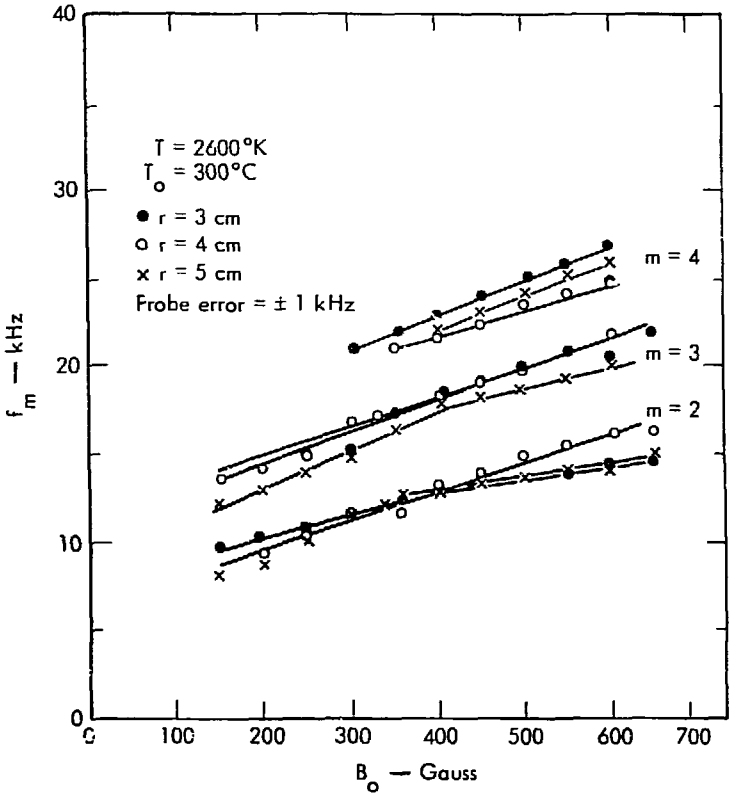

Fig. 22. Measured frequency f_m as a function of B_o at r = 3, 4, and 5 cm for the m=2, 3, and 4 modes at T ≈ 2600°K and T_o ≈ 300°C; for all of the modes, f_m increases with B_o in the column.

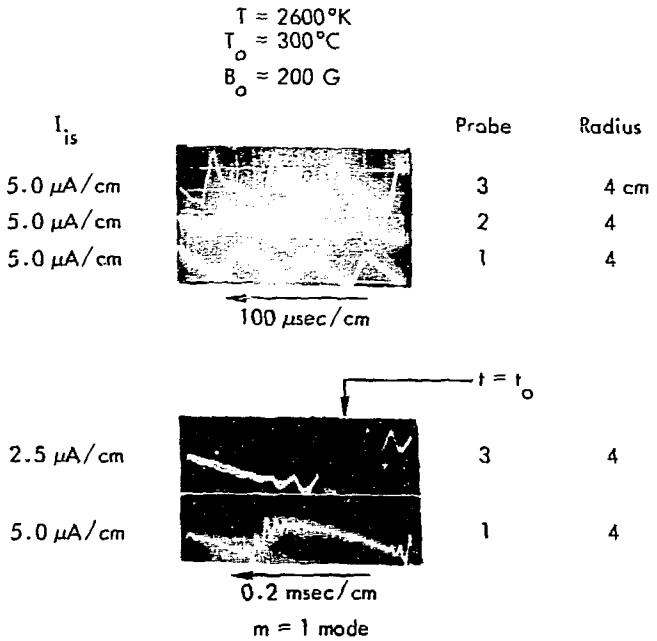

Fig. 23a. Typical waveforms for the unstable m=1 mode for the group II oscillations; $t \approx t_o$ is the time used in several later evaluations of the wave parameters.

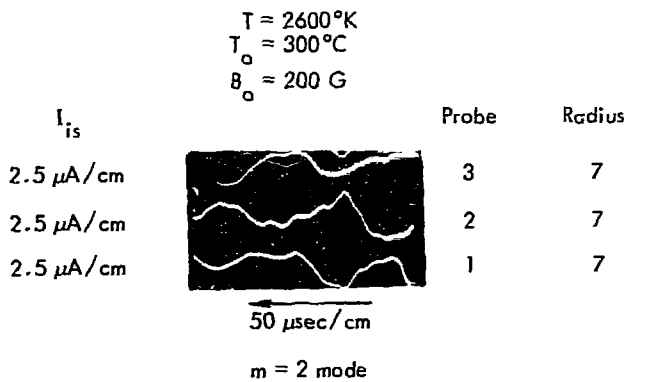

Fig. 23b. The rarely observed form of the m=2 mode of the group II waves; the wave propagates only with a saturated amplitude on the outer edge of the plasma column.

in the velocity shear region, and the parallel wavelength is long or infinite. The potential perturbation $\tilde{\phi}$ undergoes a rapid change of phase wherever $\mathrm{Re}(\omega) \simeq \omega_E$ in the column. For $k_\parallel = 0$, $\tilde{n}/n_o$ indicates no phase shift within the velocity shear region and satisfies $\tilde{n}/n_o \ll e\tilde{\phi}/KT$. The frequency lies between ω_D and ω_{EM} and is well above ω_D. The results presented in this section for the group I waves are in accord with all of the above points and indicate that the group I waves in the present experiment are due to a Kelvin-Helmholtz instability at the effective edge of the rotating plasma column.

C. Group II Oscillations

The second group of plasma waves in the experiment consists of two apparently unrelated modes. The m=1 mode is present for the whole experimental range of B_o, but it shows a periodic time-growth only for B_o between 150 G and 300 G and for sufficiently large densities. Since large enhanced radial plasma losses are recorded only during the time-growth of the m=1 waves, this mode appears to be correlated with the loss of plasma from the column. Figure 23a shows the periodic time-growth and the waveform of a typical m=1 density fluctuation. In the absence of the periodic time-growth, the m=1 mode propagates in the form of a low-level saturated amplitude oscillation.

The second wave in group II is an m=2 mode that does not appear to be a harmonic of the m=1 mode or related to the m=2 waves in the last section. The m=2 mode occurs most strongly at the column edge for $B_o \gtrsim 500$ G and does not show any periodic time-growth. Figure 23b shows a good example where the m=2

mode is clearly observed in the density fluctuations; the frequency is lower than the m=1 mode for the same conditions. Since the m=2 mode does not exhibit the periodic time-growth of the m=1 mode, it is not correlated with the enhanced radial losses from the column and is therefore ignored in the remainder of this section. The fact that the m=2 mode amplitude shows two maxima near the column edge indicates that it is probably some type of edge oscillation, possibly related to the group I waves.

The clearest experimental evidence that the m=1 mode is different from the group I shear waves is given by the phase relationship between the $\tilde{n}$ and $\tilde{\phi}$ fluctuations. Figure 24 shows correlations between $\tilde{n}$ and $\tilde{\phi}$ for the m=1 mode between $B_o \simeq 150$ to 350 G. The data indicate that $\tilde{n}$ leads $\tilde{\phi}$ in time by a phase angle close to $\psi \simeq 20°$. According to Chen,[59] a value of ψ-near $0°$ is characteristic of either a weakly unstable gravitational flute wave or an electron drift wave. These two possibilities are separable from measurements of $k_{\parallel}$ and the direction of wave propagation in the plasma.

Figure 25a shows radial profiles of the measured phase velocity V_p and computed values for V_e and V_i for the m=1 mode at $B_o = 200$ G. Both V_e and V_i are computed in the same manner as for the group I modes at the time $t \simeq t_o$ shown in Fig. 23a; the measured V_p are computed for the same instant of time. Figure 25b shows the same type of data recorded at $t \simeq t_o$ for $B_o = 250$ G. The results in both cases indicate that the waves appear to propagate in near synchronism with the ion diamagnetic drift velocity in the plasma. Therefore, the electron drift instability cannot be the origin of the m=1 waves in the present experiment.[15]

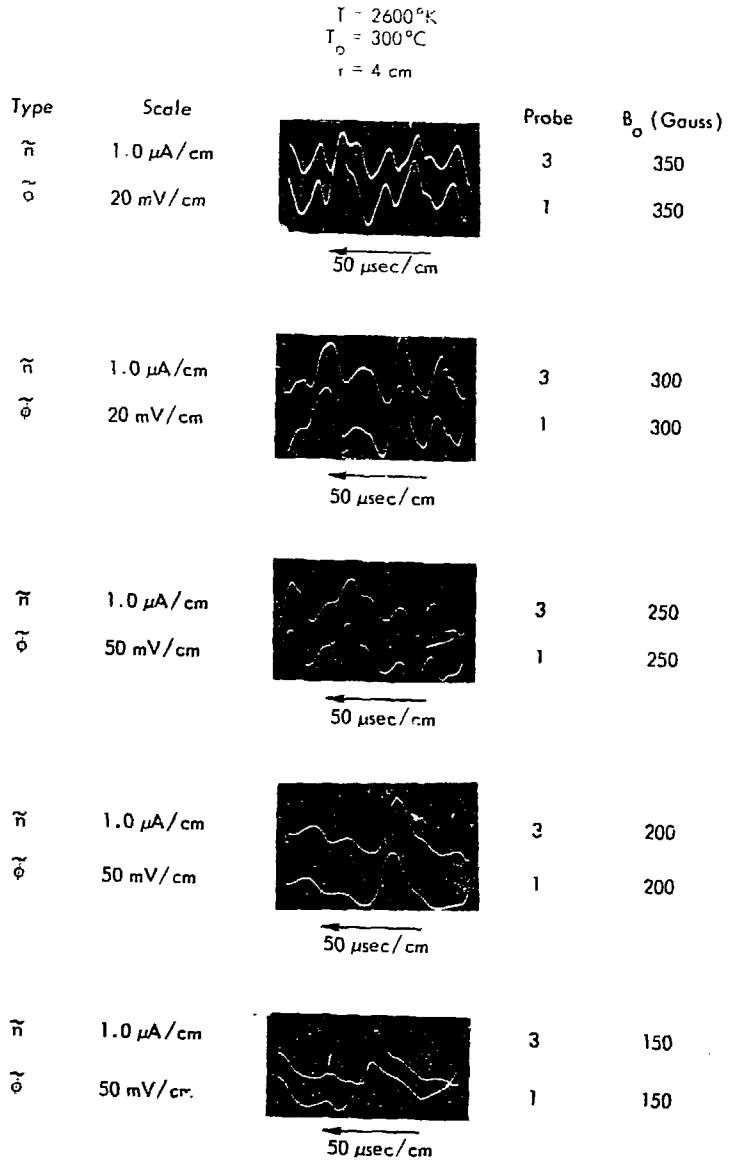

Fig. 24. Correlations between the $\tilde{n}$ and $\tilde{\phi}$ waveforms for the m=1 mode as a function of B_o; the phase shift shows $\tilde{n}$ leading $\tilde{\phi}$ in time by a small angle near 20°.

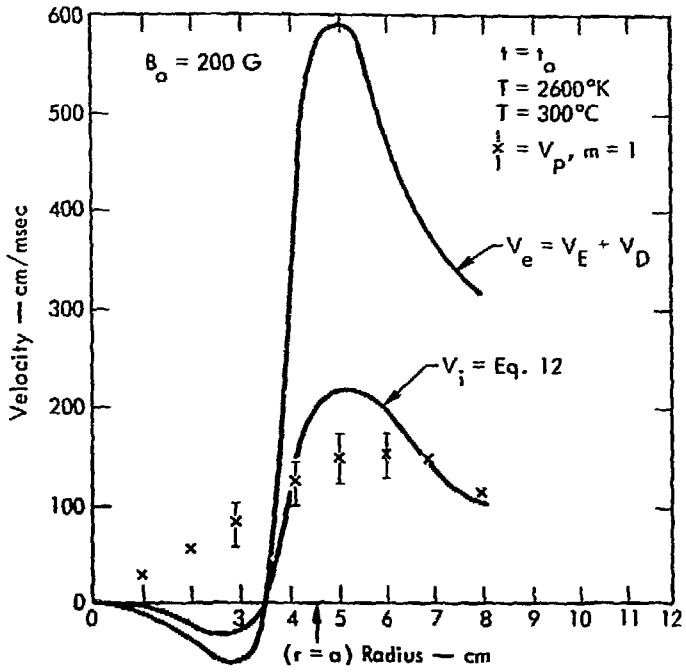

Fig. 25a. Radial profiles of V_p, V_e, and $V_i = V_{oi}$ for the m=1 mode with B_o = 200 G, T_o = 300°C, and T = 2600°K; V_p is determined from azimuthal correlation data, $V_e = V_E - V_D$, and V_{oi} is computed from Eq. 12.

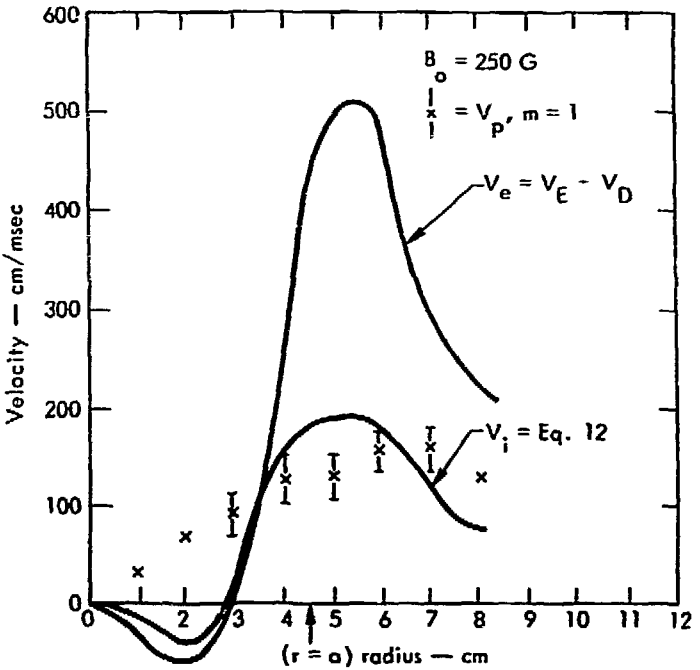

Fig. 25b. Repeat of the measurements in Fig. 25a with B_o = 250 G.

The most unstable form of the gravitational interchange instability is a flute wave, but it can also exist with $k_{\parallel} \neq 0$.[63] An experimental determination of $k_{\parallel}$ is made in a mirror magnetic field by recording both the relative wave amplitude and phase along the same magnetic field line. For the present m=1 mode, the phase change along the field line is less than or equal to minimum-detectable phase shift in the experiment, or $k_{\parallel} \lesssim \pi/5L$; the amplitude variation is a standing wave along the column. Figure 26 shows the $\tilde{n}/n_o$ standing wave for both B_o = 200 G and B_o = 250 G; the results in both cases indicate a $\lambda_{\parallel}$ of nearly 6L, or $k_{\parallel} \lesssim \pi/3L$ with an error of $\pm \pi/5L$. Therefore, the m=1 mode is probably a flute mode with $\lambda_{\parallel}$ reduced by partial line-tying at the hotplates; drift waves usually show $k_{\parallel} \lesssim \pi/L$.[15]

The interchange mode in the presence of a radial density gradient is localized near the maximum value of n_o'/n_o in the column. Figure 27 shows radial profiles of n_o'/n_o and $\tilde{n}$ for both B_o = 200 G and 250 G at the time $t = t_o$ in Fig. 23a, the radial position of the maximum value of $\partial V_{oi}/\partial r$ is shown for both values of B_o. In contrast to the group I waves, the m=1 mode shows only a single amplitude maximum that is nearly coincident with the position of the maximum n_o'/n_o in the column. In addition, a comparison of the ratios $\tilde{n}/n_o$ and $e\tilde{\phi}/KT$ shows comparable magnitudes at both values of B_o. Therefore, from the work of Perkins and Jassby,[32] cited in the last section, it appears that the m=1 mode is not caused by a Kelvin-Helmholtz instability in the present experiment.

An estimate of the radial wave number k_r of the m=1 mode is obtained by fitting the Bessel function $J_1(k_r r)$ to the data as

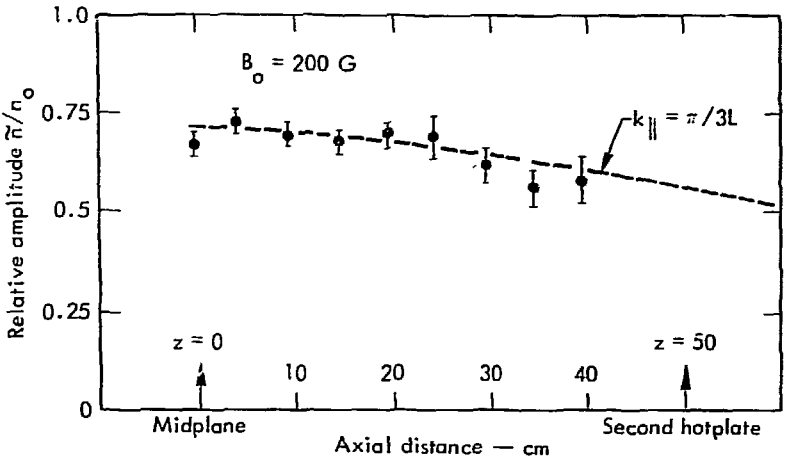

Fig. 26a. Measured relative amplitude $\tilde{n}/n_o$ for the m=1 mode as a function of the distance along the column axis; the data indicates that $k_\parallel = \pi/3L$ for B_o = 200 G in the column.

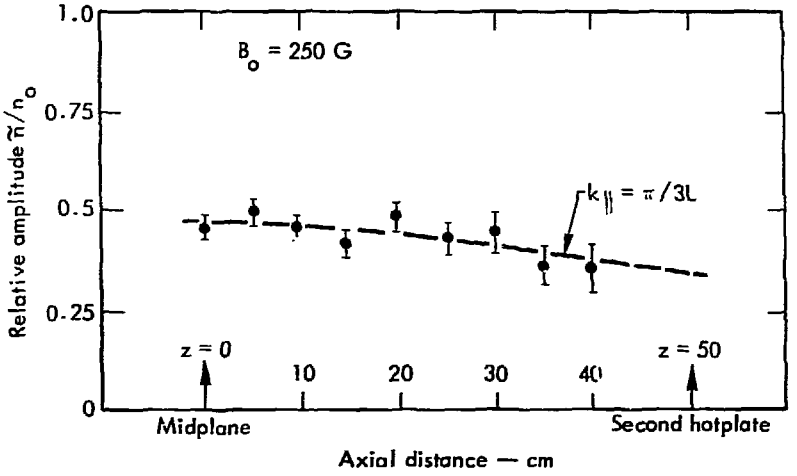

Fig. 26b. Repeat of the measurements in Fig. 26a with B_o = 250 G; the data again indicates that $k_\parallel = \pi/3L$.

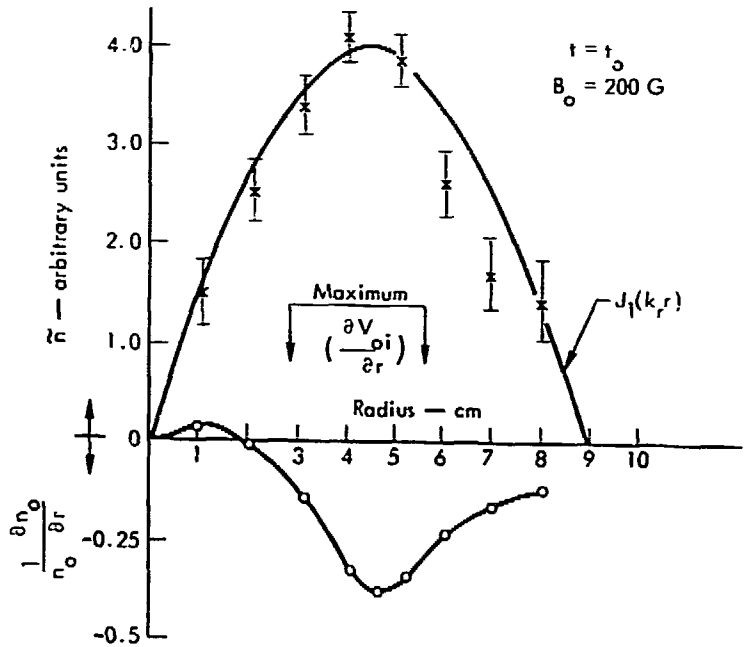

Fig. 27a. Radial profiles of $\tilde{n}$ and $\partial n_o/n_o\partial r$ compared with the Bessel function $J_1(k_r r)$ at $t = t_o$ and $B_o = 200$ G; $\tilde{n}$ shows only one maximum which coincides with those for J_1 and $\partial n_o/n_o\partial r$ in the column.

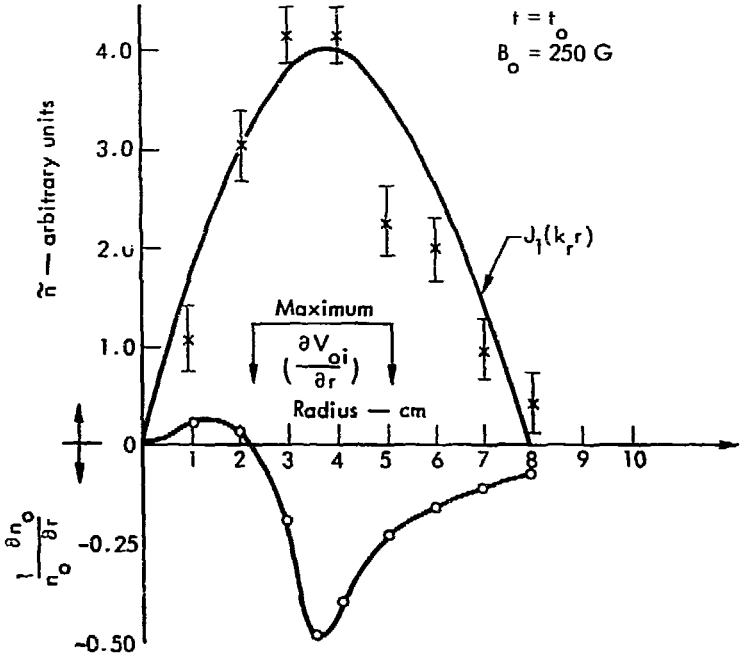

Fig. 27b. Repeat of the measurements in Fig. 27a with $B_o \approx 250$ G; the results are similar to those with $B_o \approx 200$ G with a smaller value of k_r in the plasma.

shown in Fig. 27. The amplitude and period are adjusted for the "best fit" to the data recorded at $t = t_o$. This method is justified for the radial eigenfunctions of localized wave modes in many Q-machine experiments.[64] For $B_o = 200$ G, the data indicates that $k_r = 0.43/\text{cm}$, while $k_r = 0.48/\text{cm}$ for $B_o = 250$ G. For the m=1 mode in the vicinity of the maximum wave amplitude, $k_\perp = \sqrt{k_r^2 + 1/r^2} = k_r$ presents a good approximation to the perpendicular wave number; the ratio $k_\perp/k_\parallel = 50.0$ in the present experiment.

Figure 28 shows frequency spectrum measurements of the frequency f_m (m=1) as a function of B_o for r=3, 4, and 5 cm. The solid line in the figure represents an average of the measured data and shows a slope of approximately 1.25 kHz/100 G. The fact that f_m increases with B_o indicates that $f_m \propto (E_{ro}/B_o)$ increases with B_o in the plasma column. In Fig. 28, the solid bars represent the calculated magnitudes of $V_p/2\pi r$ from Fig. 25 at $B_o = 200$ G and $B_o = 250$ G. These measurements of the frequency f_m are used later in this chapter for comparison with the predictions based on an assumed model for the instability.

If the source of the m=1 mode is some form of the well-known gravitational interchange instability, the driving force could be provided by either centrifugal forces on the column or to the magnetic field line curvature in the plasma. Using the expression $\rho V_{oi}^2/r$ for the centrifugal force density and the expression $\rho V_{Ti}^2/R_m$ for force density due to the magnetic field line curvature,[65] the ratio of the two expressions is $(V_{oi}/V_{Ti})^2 (R_m/r)$ where R_m is the radius of curvature along the magnetic field lines in the plasma. Since $R_m \gg$ column radius in the present

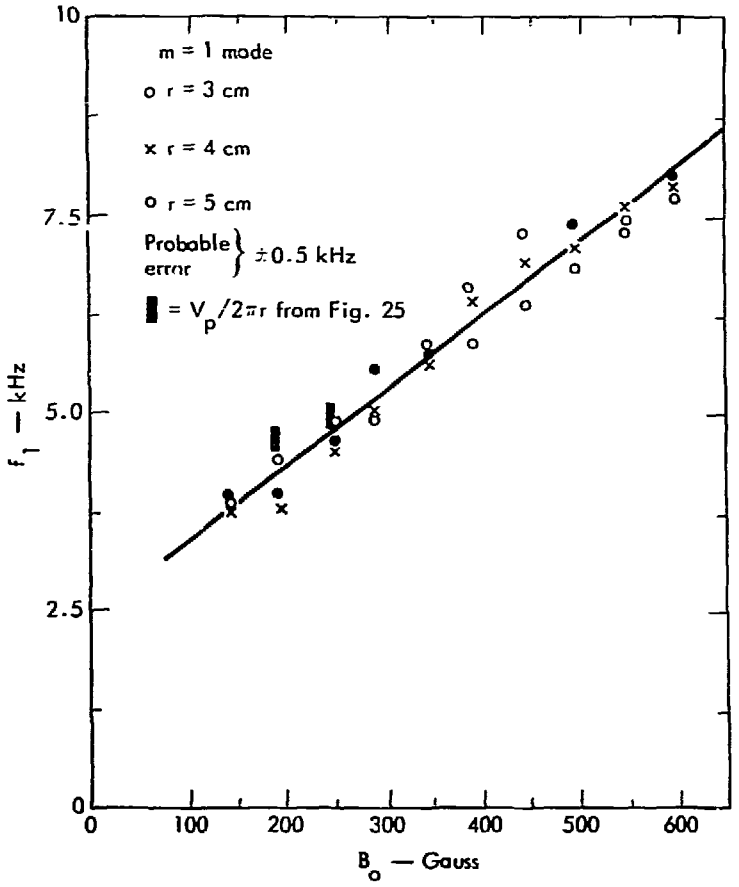

Fig. 28. Measured variation of f_1 as a function of B_o for r = 3, 4, and 5 cm in the column at B_o = 200 G and 250 G; data with V_p is plotted for comparison with the results.

experiment, the centrifugal forces are expected to be dominant in the plasma unless the condition $V_{oi} \ll V_{Ti}$ is satisfied; this condition exists external to the high-velocity annulus in the column. Thus, it appears theoretically possible for the magnetic field line curvature to cause instability in the column interior simultaneously with the centrifugal instability in the high-velocity annulus. However, Fig. 27 indicates that the m=1 mode amplitude peaks in the high-velocity annulus and is distributed throughout the column so that it appears improbable that waves from the two possible sources are separable.

Since $V_{oi} > V_{Ti}$ in the high-velocity annulus, the effect of the magnetic curvature on the existence of the periodic time-growth of the m=1 mode is expected to be negligible. A test of this prediction is provided by setting B_o between 150 and 300 G with $n_{oo} > 10^{11}/cm^3$ and studying the periodic time-growth as a function of the ratio $b_m = B_m/B_o$ where b_m is the magnetic mirror ratio and the term B_m is the magnetic field at the hotplate. Figure 29a shows some measurements at $B_o = 200$ G for $b_m = 2.0$ and 4.0; the time-growth of the m=1 mode at these two values of b_m is approximately unchanged. Similar results are found for all values of b_m between 1.5 and 5.0 in the experiment. Figure 29b shows the same type of measurement for $B_o = 300$ G; the time-growth is absent for all b_m between 2.0 and 4.0. Therefore, these results appear to indicate that the time-growth of the m=1 mode is independent of the magnetic curvature, at least within the experimental range of b_m, and that the time-growth depends primarily upon the magnitude of B_o. Figure 29c shows the onset of the m=1 mode time-growth at $b_m = 3.0$ as B_o changes from 300 to 150 G.

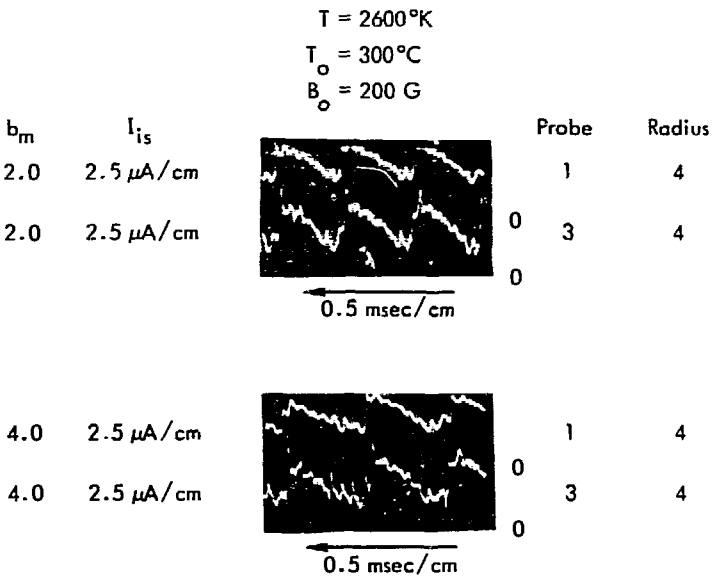

Fig. 29a. Study of the occurrence of the periodic time-growth of the m=1 mode amplitude as a function of $b_m = B_m/B_o$ and $|B_o|$; for $|B_o| = 200\ G < 300\ G$, the periodic time-growth is present for $b_m = 2.0$ and $b_m = 4.0$.

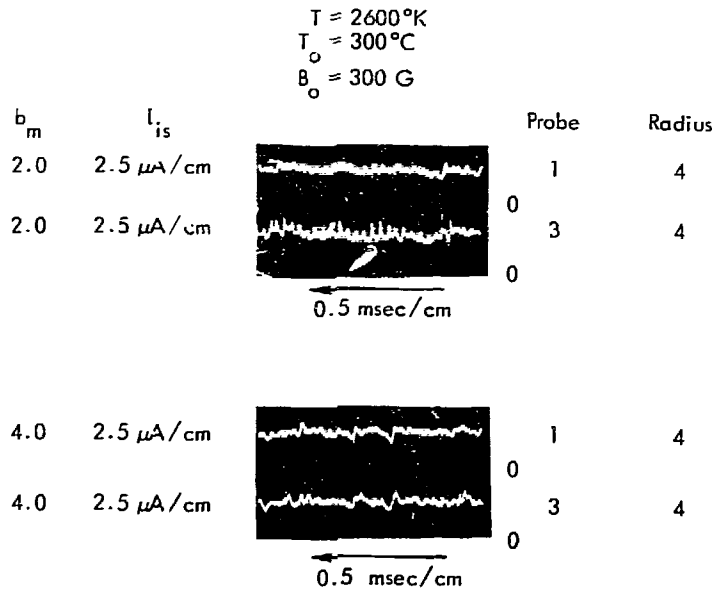

Fig. 29b. Repeat of the measurements in Fig. 29a with $|B_o|$ = 300 G; for b_m = 2.0 and 4.0, the periodic time-growth of the m=1 mode is absent.

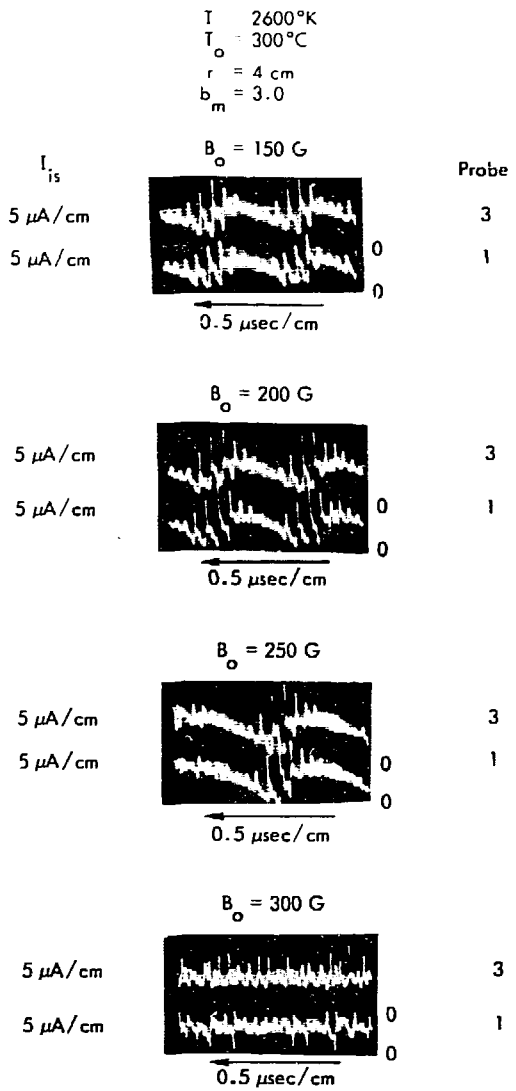

Fig. 29c. Study of the occurrence of the time-growth of the m=1 mode amplitude as a function of $|B_o|$ for $b_m \simeq 3.0$; the time-growth is present for $|B_o| < 300$ G and absent for $|B_o| \gtrsim 300$ G in the column.

Therefore, within the high-velocity region in the column, the onset of the periodic time-growth in the m=1 mode appears to be independent of b_m, but the onset depends on the magnitude of B_o being between 150 G and 300 G at the plasma midplane. The possible origin of this unstable range of B_o is discussed later in this section.

Studies of the onset of the periodic time-growth in the m=1 mode also appear to indicate the existence of a lower density threshold in the column. The time-growth of the m=1 waves first appears when the second hotplate temperature T_2 is raised toward the source hotplate temperature T_1. Figure 30 shows the onset of the periodic instability at B_o = 200 G as T_2 increases toward T_1 = 2600°K. The instability appears for an increment of approximately 100°K in T_2 and remains nearly unchanged in form for further increases in T_2. The abrupt onset of the instability in Fig. 30 could be caused by either a change in the sheath condition at the second hotplate, or by an increase in the time-average density of the plasma, or by both conditions at the same time. However, after the onset of the unstable condition in Fig. 30, the waves appear to decay in amplitude when the total density decreases below a threshold, and this result suggests the existence of a marginal stability density criterion for the m=1 mode that is only a function of n_o.

One possible explanation for the results in Fig. 30 is that the onset of the periodic instability is triggered by a switch in the sheath polarity at the hotplates. Calculations with Eq. 5 predict that ϕ_s changes sign for T between 2300 and 2400°K with n_o between 3.0 and 10.0 $\times 10^{10}/cm^3$, in accord with the measured data. However, it appears more probable that the onset of the

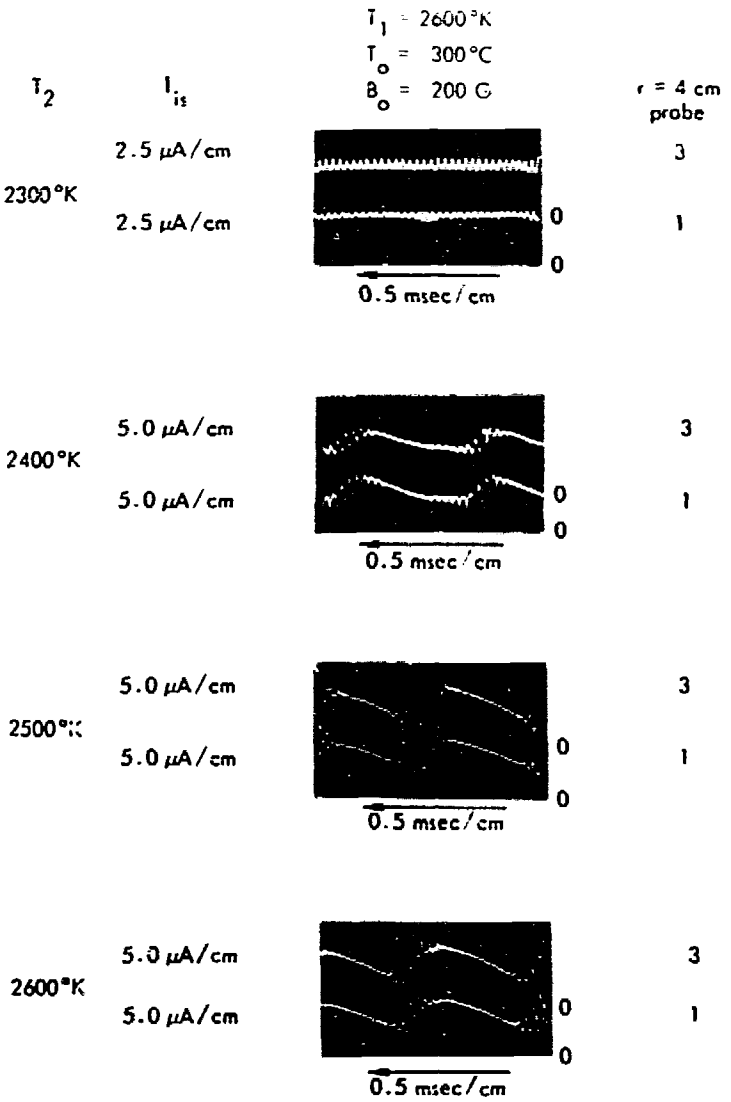

Fig. 30. Study of the onset of the periodic time-growth of the m=1 mode amplitude as a function of the second hotplate temperature T_2 with T_1 = 2600°K, T_o = 300°C, and B_o = 200 G; between T_2 = 2300°-2400°K the onset occurs and coincides with the calculated switch in the sheath potential from positive to negative.

instability is due to changes in E_{ro} at the column edge as T increases. If $|E_{ro}|$ increases with T, n_o increases from better ion confinement, and V_{oi} increases from larger $\underline{E}x\underline{B}$ rotation. Therefore, the results in Fig. 30 are in accord with both rotationally unstable waves and a threshold for n_o.

Figure 31 shows the increase in n_{oo} as a function of T_2 for several values of B_o with T_1 held constant at 2600°K. At B_o = 150 G, n_{oo} increases approximately by a factor of 5/2, while at B_o = 600 G, n_{oo} increases by the factor 5/3. In an ideal mirror magnetic field with a single hotplate, both the particle and magnetic flux are conserved along the field lines;[48] if the variation of the flow velocity is neglected, then $n_h = b_m n_{oo}$ where n_h is the plasma density on the axis of the hotplate.[53] With the addition of a second hotplate, thermal equilibrium along the field lines is possible, and the density is predicted to be constant along B_o. Therefore, as T_2 increases in Fig. 31, n_{oo} should theoretically increase by the factor b_m over that of the single hotplate case. For B_o = 600 G, b_m is measured to be nearly 3/2, in accord with the data and indicating thermal equilibrium along B_o. For B_o = 150 G, b_m = 9/2 which is double the value shown in Fig. 31. The discrepancy suggests that thermal equilibrium along B_o is absent at B_o = 150 G in accord with the presence of anomalous radial plasma losses for B_o between 150 G and 300 G.

The results shown in Fig. 30 show that once the second hotplate sheath potential is negative, the m=1 instability occurs until the large amplitude waves cause a decrease in the column

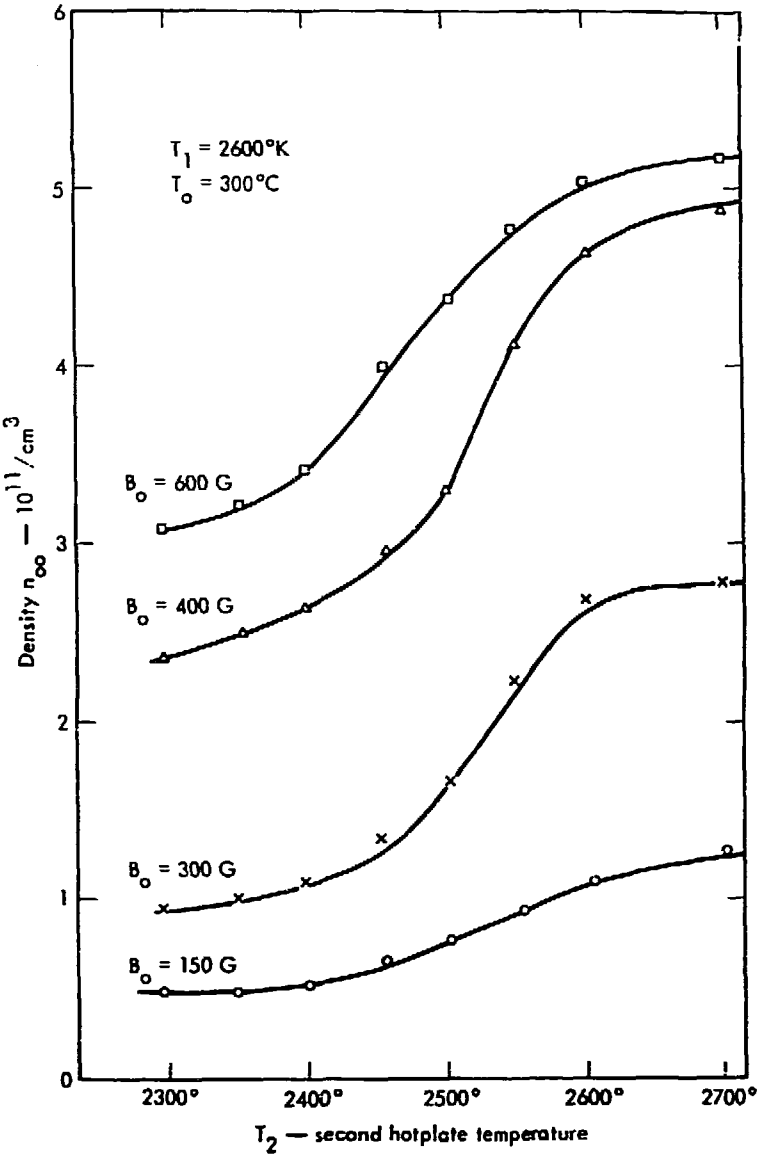

Fig. 31. Measured variation of n_{oo} as a function of T_2 and B_o with T_1 = 2600°K and T_o = 300°C; the density increases with T_2 and the amount of the increase is related to b_m in the column.

density; at this point, the instability is rapidly quenched, and the density increases to repeat the cycle. Thus, it appears that the time-growth of the m=1 mode depends on the column density exceeding a lower limit. A measure of this lower density threshold at r = 4 cm and B_o = 200 G is found by holding n_o constant at a time $t = t_o$ which ensures a negative sheath potential at the second hotplate, and varying T_2 from 2400° to 2700°K. Since Fig. 30 suggests that once the sheath is electron-rich, the m=1 instability is nearly independent of T_2, the existence of the instability depends only on the value of n_o. Figure 32a shows data at $t = t_o$ with $n_o = 8.0 \times 10^{10}/cm^3$; the m=1 mode is unstable at all of the values of T_2 shown. In contrast, Fig. 32b shows the results with $n_o = 1.2 \times 10^{10}/cm^3$; the m=1 waves are present in low-level form, together with some of the group I waves, but the periodic time-growth of the m=1 waves is entirely absent in the plasma. These results clearly indicate that the local density threshold n_c for the case shown is between 10^{10} and $10^{11}/cm^3$. By repeating the measurements for other densities in the above range, the marginal stability threshold at B_o = 200 G and r = 4 cm is estimated to be $n_c = 5.0 \times 10^{10}/cm^3$; Fig. 32c shows the m=1 waves as a function of T_2 with $n_o = n_c$, and the mode is just beginning to show instability for $T_2 \approx 2600°K$. The physical origin of n_c is discussed later in this section.

If the source of the time-growth in the m=1 mode amplitude in the present experiment is a centrifugally-driven gravitational instability, the waves should be reduced to a saturated form by a reduction in the $\underline{E} \times \underline{B}$ rotation of the plasma column. Figure 33 presents one method for creating a controllable E_{ro} in the column.

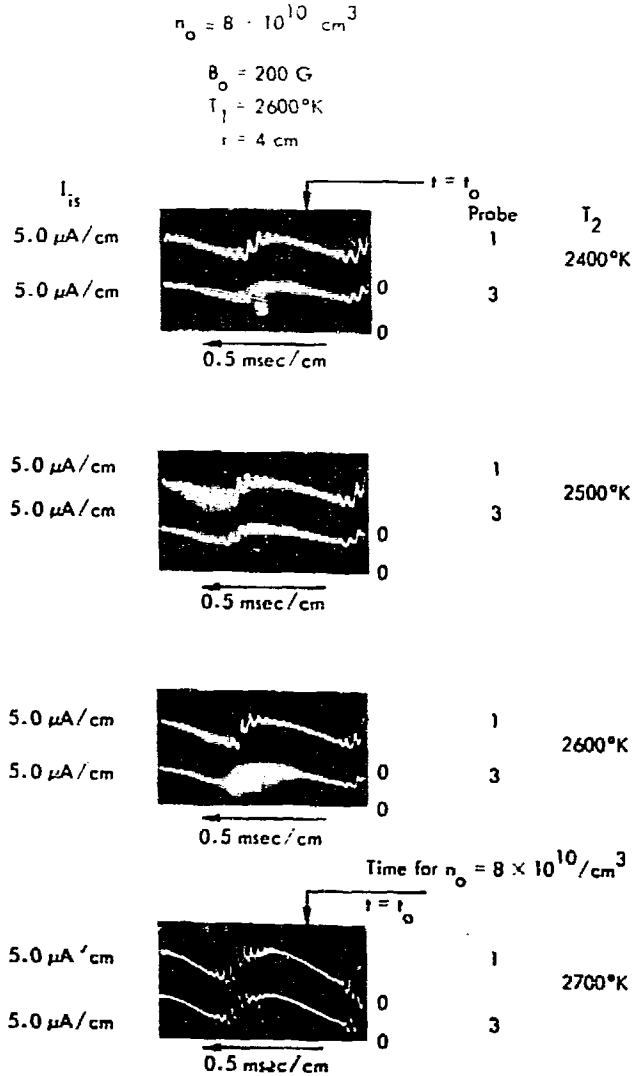

Fig. 32a. Variation in the periodic time-growth of the m=1 mode amplitude with changes in T_2 for B_o = 200 G, T_1 = 2600°K, T_o = 300°C, the probe at r = 4 cm, and $n_o = 3 \times 10^{10}$ cm^3 at $t = t_o$; between T_2 = 2400°-2700°K, the time-growth is always present.

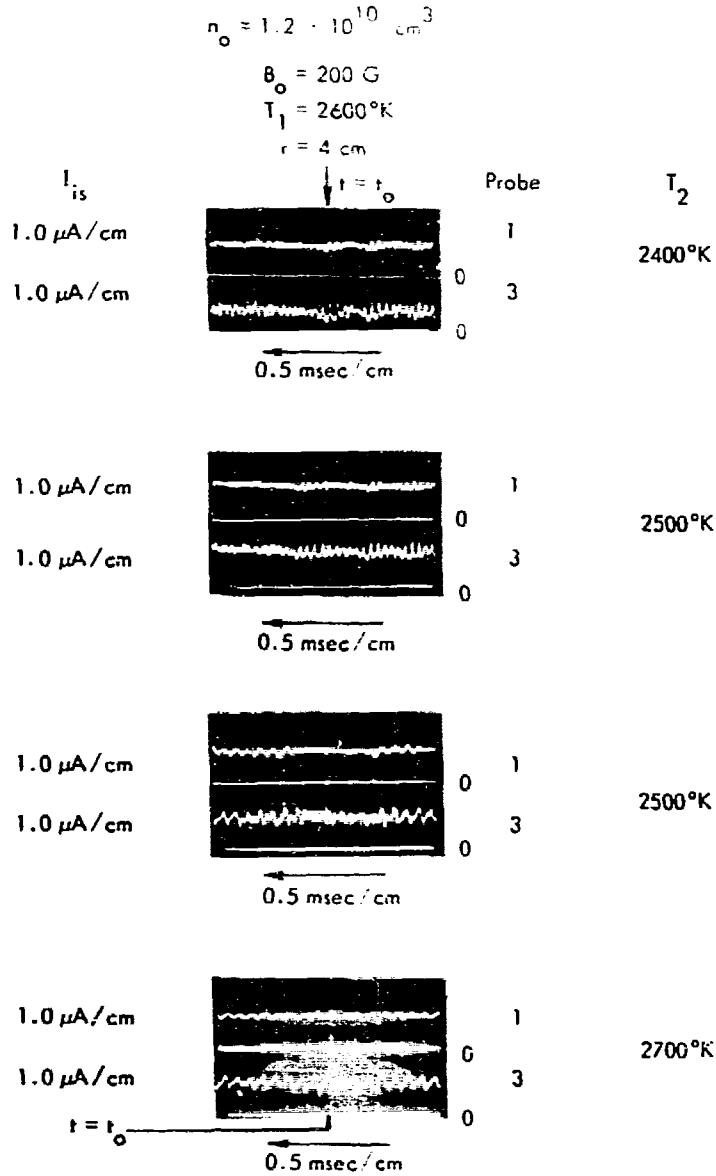

Fig. 32b. Repeat of the measurements in Fig. 32a with $n_o = 1.2 \times 10^{10}$ cm^{-3} at t = t_o; between T_2 = 2400°-2700°K, the periodic time-growth of the m=1 mode amplitude is always absent.

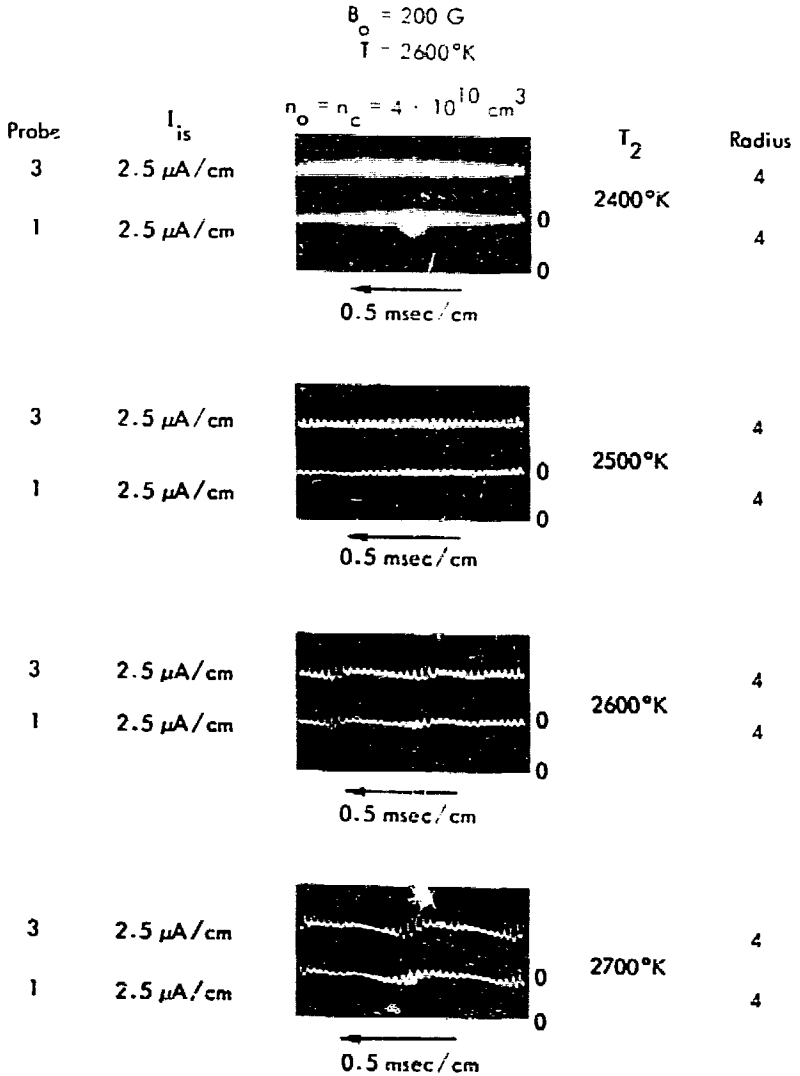

Fig. 32c. Detailed study of the onset of the periodic time-growth in the m=1 mode amplitude as a function of T_2 and n_o: for $n_o = n_c = 4 \times 10^{10}$/cm^3 at r = 4 cm and B_o = 200 G, the onset of the instability appears to be nearly independent of T_2.

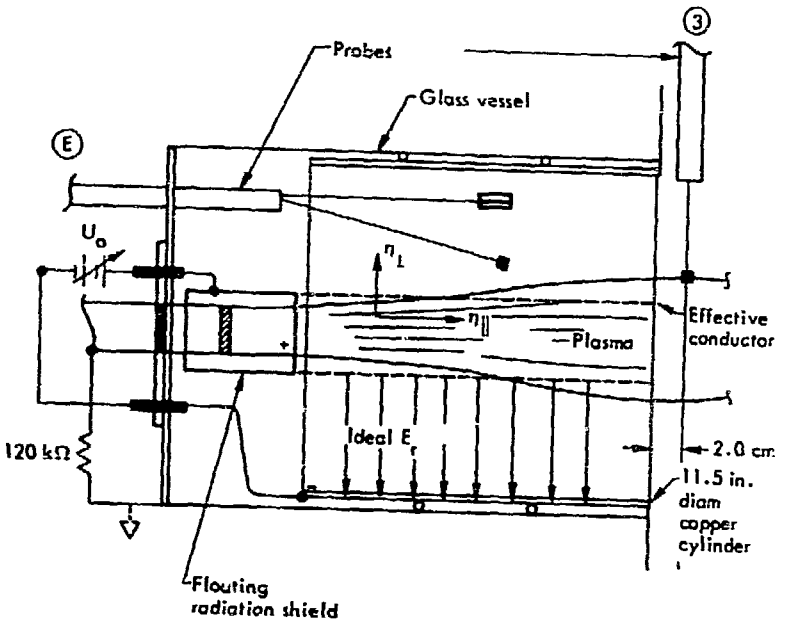

Fig. 33. Modified experimental apparatus for the creation of a controllable E_{ro} in the plasma column.

The technique requires that the voltage drop in the plasma be primarily radial for any voltage applied between the second hot-plate heat shield and the large coaxial copper electrode.

Using the plasma model of Chapter III, the ratio $|E_{ro}/E_{zo}|$ can be estimated as follows. The current density j_z is related to j_r by the current continuity equation, and j_r is determined by Eq. 10; approximating E_{zo} by ηj_z where η is the Spitzer form[53] for the parallel resistivity in a fully ionized plasma and using Eq. 12 for calculating E_{ro}, the ratio $|E_{ro}/E_{zo}|$ is generally much greater than unity for the present experimental conditions. Therefore, the electric field created by the electrode system in Fig. 33 is expected to be primarily radial in direction.

Figure 34a shows the measured E_{ro} at the column midplane for an applied voltage U_o between -50V and 20V at B_o = 200 G. E_{ro} is calculated from radial profiles of the probe floating potential ϕ_m which are recorded at the center of the high-velocity annulus in the column. For $U_o < 0$, the effective E_{ro} in the column is reduced, while for $U_o > 0$, the E_{ro} appears to increase until an $\underline{E}x\underline{B}$ reflex discharge or P.I.G discharge occurs.[66] The results in Fig. 34a indicate that only about 5% of the applied voltage penetrates the plasma-electrode sheath and produces an E_{ro} in the column; the remaining 95% of U_o is dropped at the sheath of both electrodes.

Using the directional Langmuir probe, a direct measure of V_{oi} for B_o = 200 G and r = 4 cm is shown in Fig. 34b as a function of U_o. The results show that a decrease in E_{ro} does produce a corresponding decrease in the V_{oi} of the plasma. Using Eq. 12 to compute V_{oi}, a numerical comparison between the data for E_{ro}

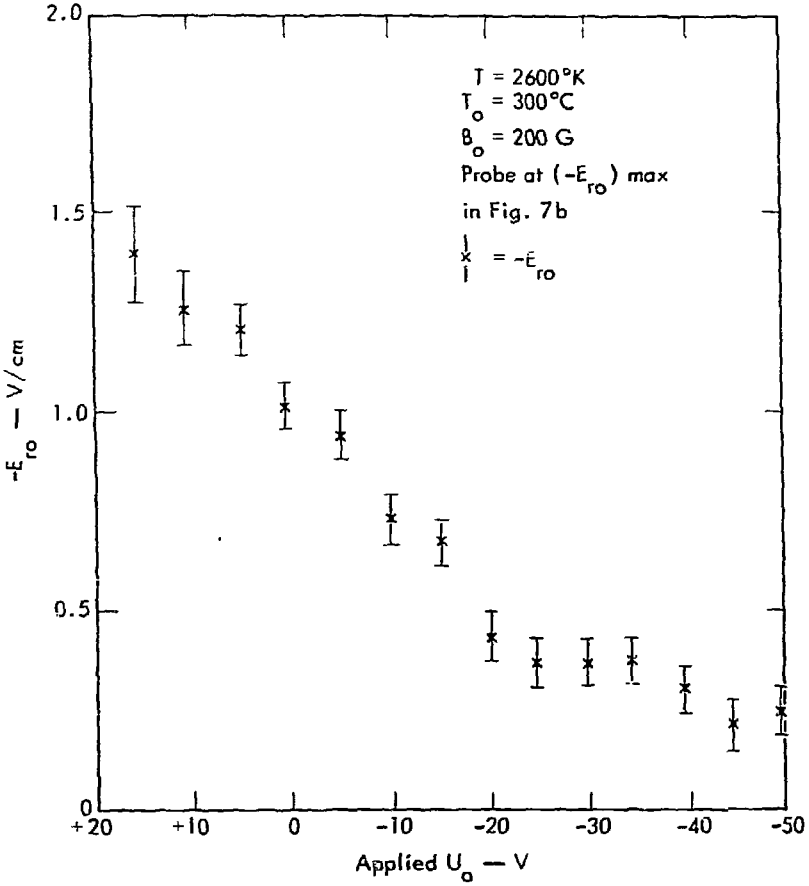

Fig. 34a. Variation of the measured $-E_{ro}$ in the column as a function of U_o between the electrodes; for $U_o < 0$, the $\vec{E}x\vec{B}$ rotation of the column is reduced, while for $U_o > 0$, the rotation is increased.

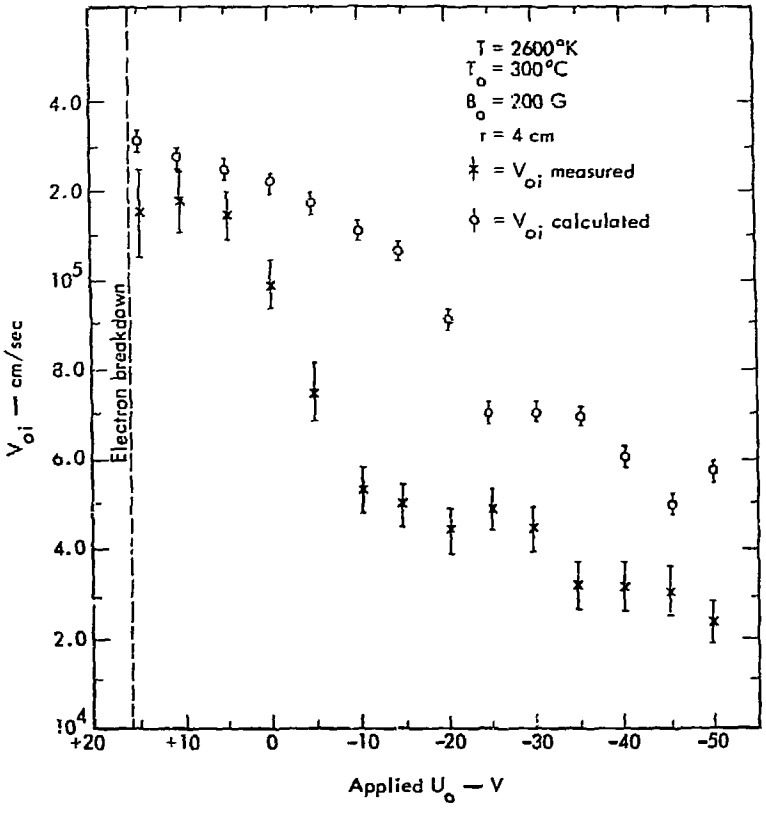

Fig. 34b. Comparison of the V_{oi} computed from the data in Fig. 34a and the V_{oi} measured at r = 4 cm with the directional Langmuir probe. Compensating for the different probe locations in the two cases, the results indicate similar magnitudes and variation with U_o.

at the center of the high-velocity annulus and the data for V_{oi} at r = 4 cm is also shown in Fig. 34b; the functional variation of both the computed and measured V_{oi} with U_o is similar in form. From Fig. 7b, the measured E_{ro} at r = 5.5 cm is approximately 2.5 times that at r = 4 cm for B_o = 200 G. Therefore, the computed V_{oi} in Fig. 34b should be reduced by a factor of 2.5 for comparison with the measured V_{oi} shown, and the two results then indicate close numerical agreement.

Using the above results, the periodic variation of the m=1 mode amplitude is studied as a function of U_o. Figure 35a shows the effect of decreasing V_{oi} for B_o = 200 G; the probe is located in the center of the high-velocity annulus. Figure 35b shows the effect of increasing V_{oi} under the same conditions as in Fig. 35a. The decrease in V_{oi} reduces the total density fluctuation in the column and eventually removes the periodic time-growth of the m=1 mode completely at U_o = -50V. The apparent stabilization could be due to either a balance between a reduced m=1 growth rate and dissipative processes in the plasma or the propagation of a negative energy wave in the plasma column; the experimental results are unable to distinguish between the two cases. Due to the P.I.G discharge for $U_o \geq 15$ V, the effect of increased $\underline{E}x\underline{B}$ rotation on the m=1 mode amplitude is obscured by electrical noise at the probe, and no clear evidence is available for consideration in the present work.

The experimental measurements of the m=1 mode characteristics are summarized as follows: 1) The wave phase velocity V_p is nearly synchronous with the ion drift velocity in the plasma rest-frame. 2) $\tilde{n}$ leads $\tilde{\phi}$ in time by a phase angle ψ near 20° and

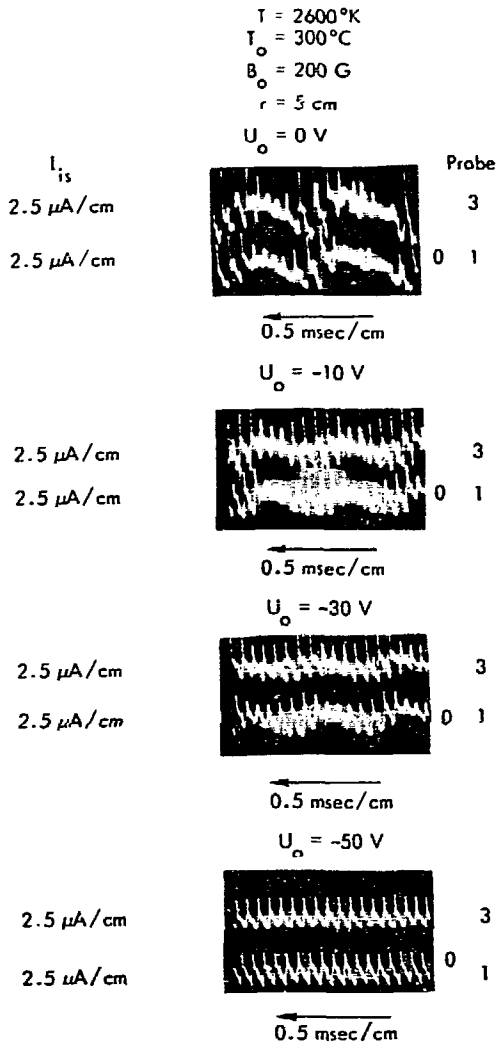

Fig. 35a. Variation of the time-growth in the m=1 mode amplitude as a function of $U_o < 0$ for $T \simeq 2600°K$, $T_o \simeq 300°C$, $B_o \simeq 200$ G, and the probe at $r \simeq 5$ cm; decreasing the $\vec{E}x\vec{B}$ plasma rotation leads to removal of the periodic time-growth of the waves.

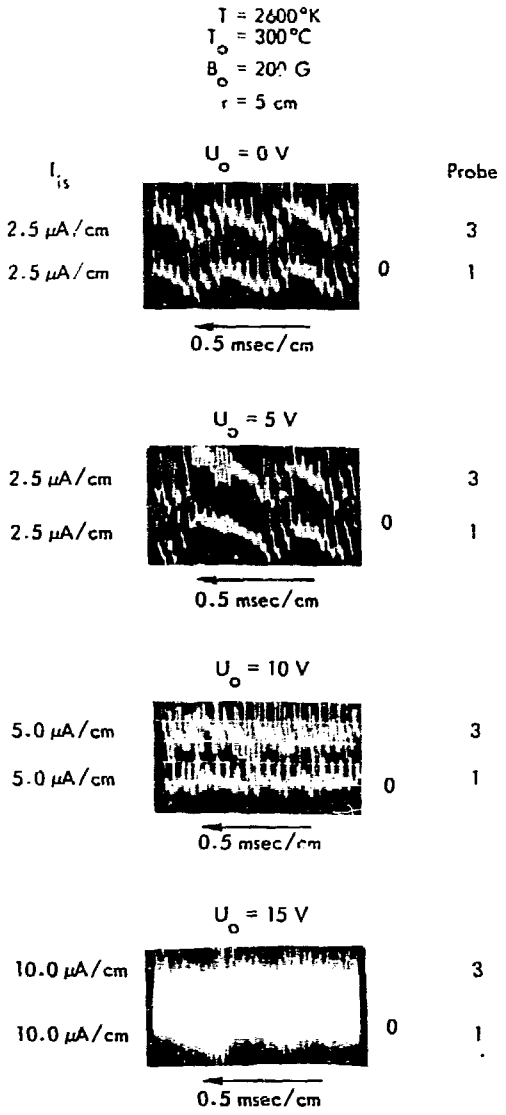

Fig. 35b. Repeat of the measurements in Fig. 35a with $U_o > 0$; the onset of a P.I.G discharge in the plasma obscures the effects of increased $\underline{E}x\underline{B}$ column rotation on the wave stability.

is in the proper phase relation to produce a radial plasma convection. 3) The ratio $\tilde{n}/n_o$ is comparable in magnitude with the ratio of $e\tilde{\phi}/KT$ in the waves. 4) $a_i \gtrsim \lambda_c$ is satisfied for 150 G $\lesssim B_o \lesssim$ 300 G. 5) The wave amplitude $\tilde{n}$ shows only a single maximum in the vicinity of the maximum magnitude of n_o'/n_o in the column. 6) Measurements of $k_{||}$ in the column show a parallel wavelength $\lambda_{||} \gtrsim 6L$ due to standing waves between the hotplates. 7) The time-growth of the m=1 mode amplitude occurs only in the range, 150 G $\lesssim B_o <$ 300 G, and when the local density exceeds a lower threshold between 10^{10} - $10^{11}/cm^3$. 8) The time-growth of the m=1 waves is suppressed by reducing the local density and by reducing the local column rotation V_{oi} below a minimum threshold.

The result 1) appears to eliminate the electron drift instability as the source of the m=1 waves; the results 2), 3), and 5) appear to eliminate the transverse Kelvin-Helmholtz instability as the wave source;[32] results 7) and 8) indicate that the wave source is probably the centrifugally driven flute instability with lower threshold cutoffs in n_o and V_{oi} in the range of B_o between 150 G and 300 G; result 6) shows that the flute mode is probably line-tied by the electron-rich sheath potential at the hotplates;[63] and result 4) indicates that finite Larmor radius terms are probably unimportant in determining the wave instability in the plasma. All of the observations are consistent with a centrifugally-driven interchange instability with a finite $k_{||}$ due to partial "line-tying" at the hotplates.

A theoretical analysis of the plasma wave stability for the present experimental conditions does not appear to be available in the literature. The closest plasma model to that of the present

work appears to be that of Chu et al.[63] which presents approximate calculations for a uniformly rotating plasma cylinder in a uniform magnetic field; the model includes the effects of ion collisional viscosity, finite Larmor radius, finite $k_{\|}$, and the $\underline{E}x\underline{B}$ column rotation on the wave stability. The ion pressure tensor employed in the calculations is strictly valid in the limit with $\lambda_c \gg a_i$, but for $a_i \gg \lambda_c$, the tensor components reduce to the usual Navier-Stokes form with small corrections.[54] Since the finite Larmor radius (FLR) corrections are clearly distinguishable from the collisional terms in the analysis, the work of Chu et al. should also be valid in the collisional limit.

From the discussion in Chapter III, the plasma rotation V_{oi} may be assumed to be approximately constant in the high-velocity annulus and negligible otherwise; the effect of velocity shear is ignorable in the case of the m=1 mode and is assumed to help in the radial localization of the waves, in accord with the assumption of Chu et al. In addition, measurements of B_o along the column axis indicate that B_o is nearly constant for a distance of approximately 15 cm on either side of the vessel midplane. Therefore, the model in Chu et al. should provide qualitative explanations for most of the experimental observation in the present work, but numerical agreement between the theory and the experiment is not expected.

The final dispersion relation derived in the work of Chu et al. is given in the form[63]

$$(m + y + 2i\bar{\Sigma})(yb + iB) - i\bar{\Sigma}(m - y) = (ma_i^2/r_o^2)\left[(y + i\bar{\Sigma})(1 - 2\phi_o) - \phi_o^2(m + i\bar{\Sigma})\right] \qquad (26)$$

where $\bar{\Sigma} = \sigma\,(\Omega_i/2\nu_{ii})$ and $\sigma = 0.84\,(k_\parallel r_o)^2\sqrt{(m_i/m_e)}$ is due to the electron resistivity along B_o, $y = (\omega - m\omega_{D})\phi_o)/\omega_{D}$ is the normalized wave frequency in the laboratory with $\omega_{D} = \left(2KT/eB_o r_o^2\right)$ as the diamagnetic frequency in the plasma, a_i is the ion gyroradius, r_o is the radial scale-length of $n_o(r)$, and ϕ_o is the plasma potential normalized to KT/e. The analysis leading to Eq. 26 assumes that $n_o(r) \sim \exp(-r^2/r_o^2)$, and that all perturbed quantities vary as $\exp(-i\omega t + ik_\parallel z + im\theta)$. The terms b and iB are the approximate contributions of quadratic forms for FLR and ion viscosity, respectively.

Using the approximations $b = (k_\perp a_i)^2/2$ and $k_\perp = 2m/r_o$, Chu et al. studied the marginal stability of Eq. 26 and showed that the centrifugal instability occurred whenever $\phi_o > \phi_{oc}$ where

$$\phi_{oc} = (1/2)\left[1 \pm \sqrt{2\,(1 + 8\sigma)}\right] \qquad (27)$$

is the finite $k_\parallel$ modification of the centrifugal stability limit found by Rosenbluth et al.[58] and by Chen.[64] Measurements of ϕ_o in the present experiment indicate that ϕ_o varies between 5.0 and 10.0 in the column, while for $\lambda_\parallel$ between 200 and 600 cm, ϕ_{oc} at B_o = 150 G is predicted to range between 2.0 and 5.0. Therefore, on the basis of Eq. 27, the m=1 mode in the present experiment is probably unstable to centrifugal forces in the plasma column.

The result in Eq. 27 predicts that the waves are unstable for $\phi_o > \phi_{oc}$ independently of the parameters $\bar{\Sigma}$ and B in the plasma; but the experimental observations indicate that the periodic time growth of the m=1 waves is a function of both B_o and n_o. The work of Chu et al. predicts just such a dependence on n_o and B_o for

the case of the ion diamagnetic waves with $\phi_o < \phi_{oc}$. In terms of physical quantities, the waves are unstable when

$$(\Sigma/B) = t_\perp/2t_\parallel \propto B_o^4/n_o^2 < \text{constant} \sim 1.0 \qquad (28)$$

where $B = b(\nu_{ii}/\Omega_i)$ with $b = (k_\perp a_i)^2/2$, $t_\perp = 2B$ is the effective time required for an ion to diffuse a distance $1/k_\perp$ transverse to B_o, and $t_\parallel = \nu_{ei}/(k_\parallel V_{Te})^2$ is the time required for an electron to move a distance $1/k_\parallel$ along B_o in the column.[15] Physically, Eq. 28 predicts that the ion diamagnetic wave is unstable for $\phi_o < \phi_{oc}$ whenever the ions establish a charge separation transverse to B_o in a time that is short compared with that required for the electrons to flow along B_o and neutralize the resulting electric field. Increasing B_o retards the ion motion, while decreasing n_o accelerates the electrons, and both results can lead to $t_\perp > t_\parallel$ and wave stabilization, in accord with experimental observations.

In the present case, the condition $\phi_o > \phi_{oc}$ appears to be satisfied for all measurements, and the m=1 mode exists in two distinct forms. Therefore, based on the above discussion, a possible explanation for the onset of the periodic time-growth in the m=1 mode is as follows. When $\phi_o > \phi_{oc}$ but $t_\perp > t_\parallel$, the m=1 mode growth-rate is low enough to be balanced by the mode losses in the plasma, and the waves propagate with a saturated amplitude. However, when $\phi_o > \phi_{oc}$ and $t_\parallel > t_\perp$, the mode growth-rate is large enough to overcome the corresponding mode losses and produces the large amplitude time-growth that is observed. In the case where $\phi_o < \phi_{oc}$ with $t_\parallel > t_\perp$, the mode again propagates with a saturated amplitude. The foregoing hypothesis is

thus able to qualitatively account for the existence of two forms of the m=1 mode, and for the vanishing of the periodic time-growth when $B_o > 300$ G, when $n_o < n_c$ for B_o between 150 and 300 G, and when V_{oi} is reduced below a minimum value in the column.

To provide detailed numerical comparisons with the data, Eq. 26 is split into real and imaginary components with the definition that $y = X + iY$, and the results are written in the form

$$X^2 + Q_1 X + Q_3 = Y^2 + Q_2 Y \tag{29}$$

$$Y(2X + Q_1) + (Q_2 X + Q_4) = 0 \tag{30}$$

where the Q-parameters are defined as follows:

$$Q_1 = 1 + a_i^2/br_o^2 \quad (2\phi_o - 1) \tag{31a}$$

$$Q_2 = B/b + (\bar{\Sigma}/b)(1 + 2b) \tag{31b}$$

$$Q_3 = \left(a_i^2/br_o^2\right)\phi_o^2 - \alpha \tag{31c}$$

$$Q_4 = B/b - (\bar{\Sigma}/b)\left[1 - (a_i/r_o)^2\left(\phi_o^2 + 2\phi_o - 1\right)\right] \tag{31d}$$

Equation 27 is derived by setting $Y = 0$ in Eq. 29 and requiring that X have real solutions. Equations 29 and 30 can be combined to form a biquadratic in X

$$(X + Q_1/2)^4 + M^2(X + Q_1/2)^2 - W^2 = 0 \tag{32}$$

where $M^2 = Q_3 + Q_2^2/4 - Q_1^2/4 > 0$ and $W = (Q_2/2)(Q_1/2 - Q_4/Q_2)$. Equation 32 is used to compute X and Eq. 30 is used to compute the corresponding value of Y. Note that b is now arbitrary and $k_\perp \neq 2m/r_o$.

Equations 29 and 30 can be graphically represented as two hyperbolas as shown in Fig. 36; the case illustrated has an unstable solution in the range $-Q_4/Q_2 < X < -Q_1/2$.

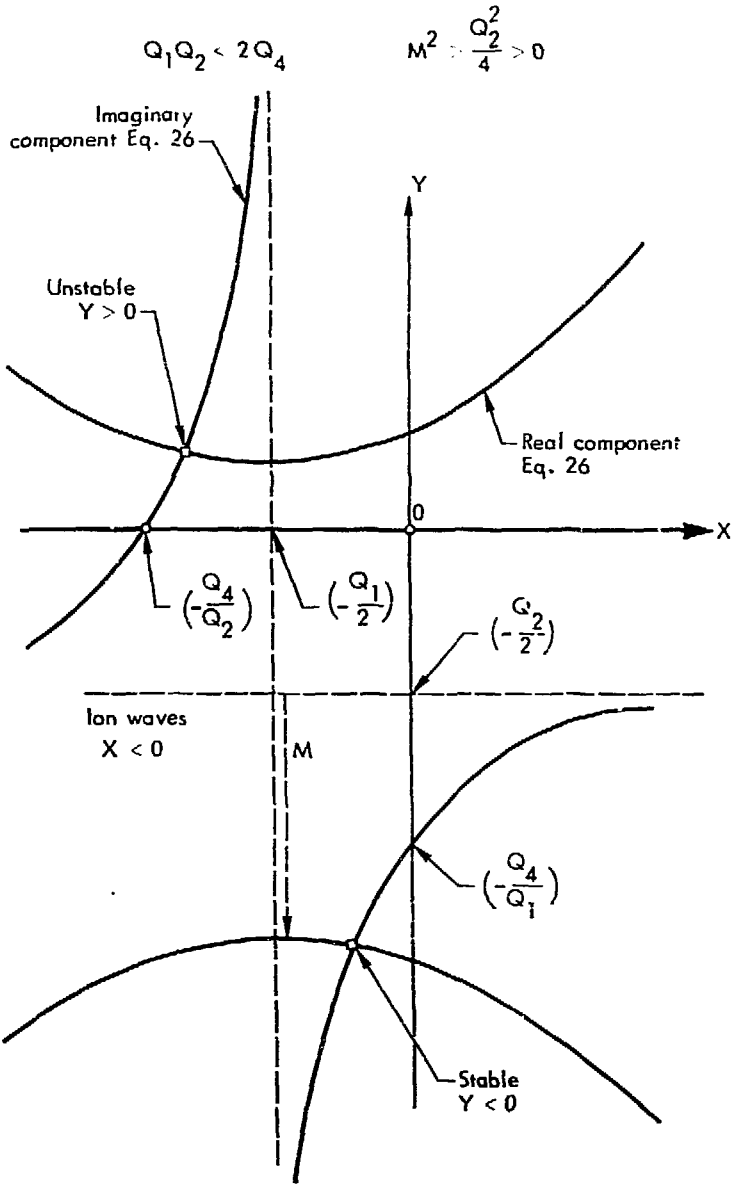

Fig. 36. Graphical representation of Eqs. 29 and 30 and their solution for the conditions $M^2 > Q_1^2/4 > 0$ and $Q_1Q_2 < 2Q_4$; the results indicate an unstable ($Y > 0$) root for $X < 0$.

Figure 37 presents the results of numerical computations for X and Y as a function of $\lambda_{\parallel}$ at B_o = 150 G and for three selected values of ϕ_o in the column. The data point in Fig. 37a shows the mean of six independent measurements for the m=1 mode frequency f_1 in the high-velocity annulus, and the error bars indicate the variation about the mean value. The corresponding data point in Fig. 37b is found from measurements of the time-growth of the m=1 mode amplitude.

The theoretical predictions in Fig. 37a show that $X < 0$ (ion waves) and increases with $\lambda_{\parallel}$ for all three values of ϕ_o shown; for a fixed value of $\lambda_{\parallel}$, $-X$ increases with ϕ_o. The measured point corresponds to $\phi_o \approx 10.0$ at $\lambda_{\parallel} \approx 600$ cm, in good agreement with the $\phi_o = 8.9$, computed from measurements of r_o and E_{ro} at B_o = 150 G. The predicted value of Y shows a maximum that depends on the value of ϕ_o, and the value of $\lambda_{\parallel}$ for which the maximum occurs appears to vary inversely with ϕ_o. The measured growth-rate shows a value comparable in magnitude with $\omega_D(Y = 1)$, but appears to correspond to $\phi_o = 6.0$. Considering the assumptions necessary in applying Eq. 26 to this present experiment, the agreement shown in Fig. 37 between theory and experimental data is much better than expected.

Considering the good agreement between theory and the data indicated in Fig. 37, additional numerical calculations are meaningful. Figure 38a shows the numerical fit of the calculated values of $-X$ to the data in Fig. 37 by adjusting the parameters $k_\perp r_o$ and ϕ_o with $\alpha = 0.36$ at B_o = 150 G; Fig. 38b presents a comparison between the required theoretical values of both $k_\perp r_o$ and ϕ_o with

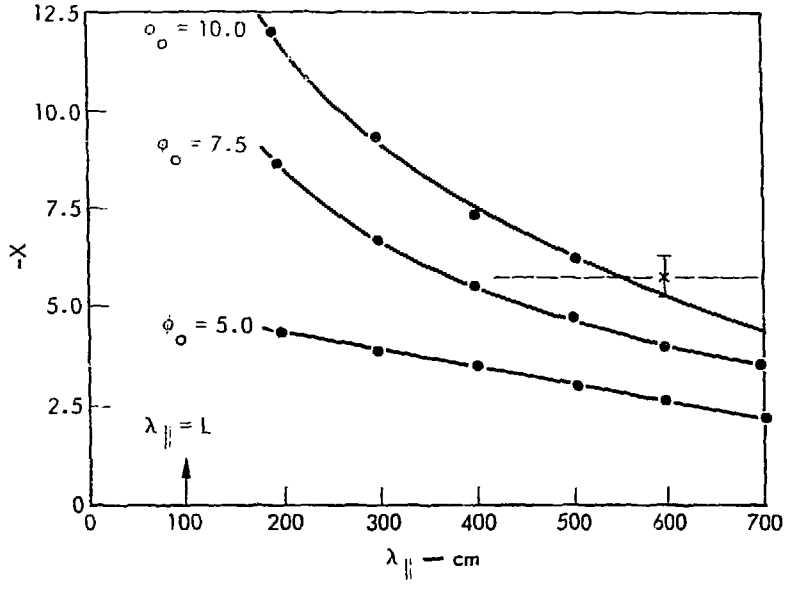

Fig. 37a. Calculated values of -X as a function of $\lambda_{\parallel}$ and ϕ_o compared with measured data at B_o = 150 G in the present experiment; the data point shows that ϕ_o = 10.0 and -X = 6.0.

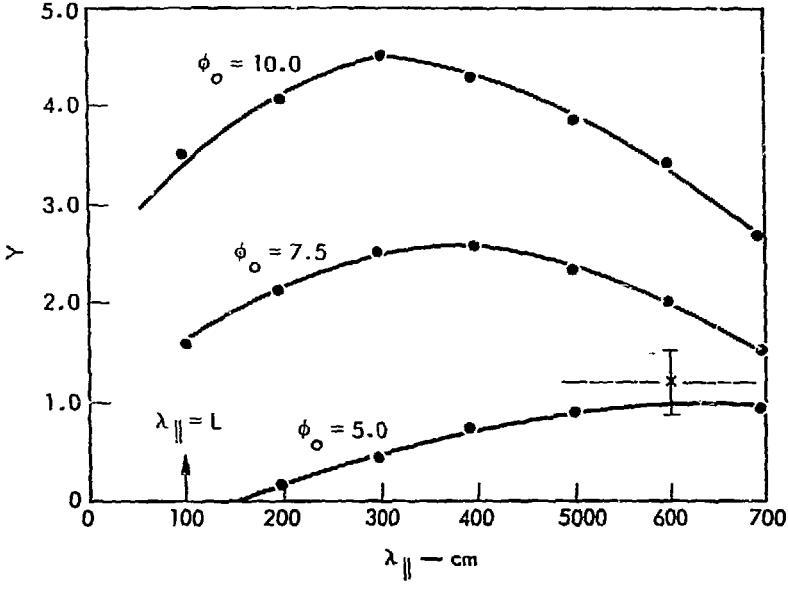

Fig. 37b. Calculated values of Y for the same conditions as in Fig. 37a; the data point shows ϕ_o = 6.0 and Y = 1.0.

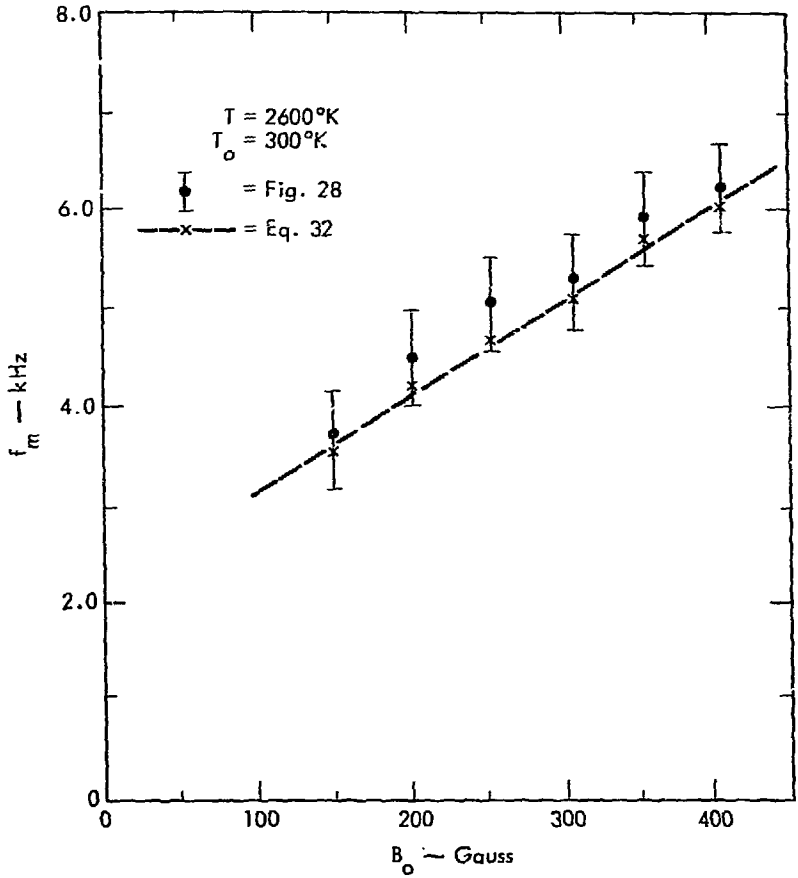

Fig. 38a. Calculated fit of -X from Eq. 32 for the data in Fig. 28 in the form of -X as a function of B_o; the calculations are made by varying the required values of $k_\perp r_o$ and ϕ_o.

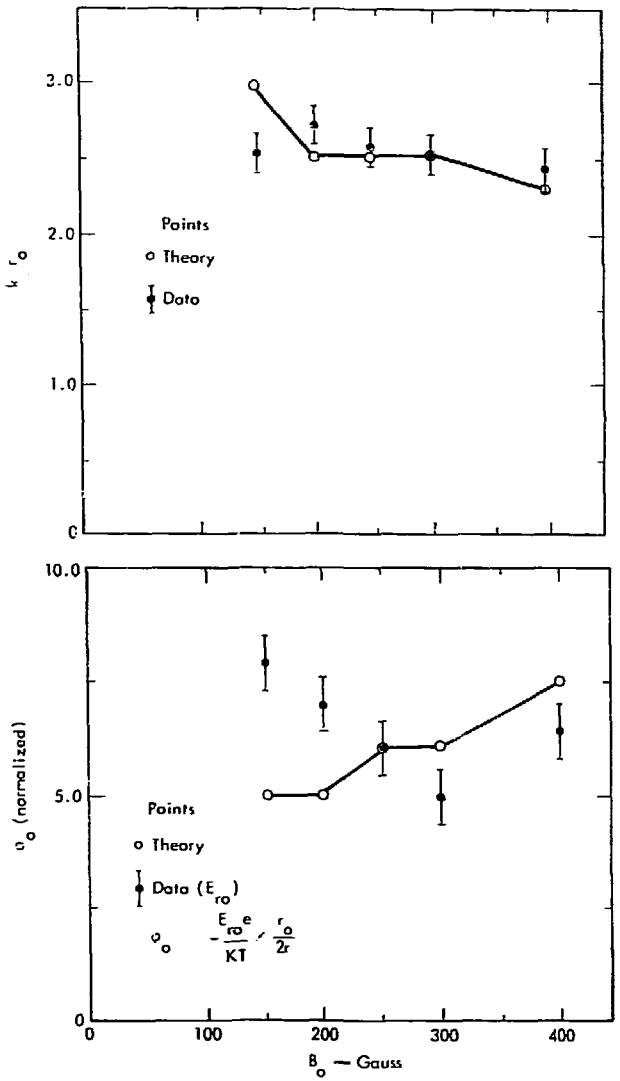

Fig. 38b. Comparison between the values for $k_\perp r_o$ and ϕ_o required to fit the data in Fig. 38a and the corresponding measured values; the results are more sensitive to values of ϕ_o than to the variations in $k_\perp r_o$.

the corresponding experimental values, and the results show good agreement between theory and the data. Therefore, the theory of Eq. 26 can account for both the linear increase of f_1 with B_o and the variations in $k_\perp r_o$ and ϕ_o that are necessary for matching the data with theory.

A qualitative prediction of the linear increase of f_1 with B_o is obtained from Eq. 32 as follows. The general solution for X is written in the form

$$X = -Q_1/2 \pm \sqrt{-M^2/2 \pm \sqrt{(M^4/4 - W^2)}} \qquad (33)$$

For the present experiment, the condition $b\tilde{\Sigma}/B \ll 1$ is satisfied and, for $\phi_o \gg 1$ and $b \simeq 2a_i^2/r_o^2$, leads to the inequality $M^4 \gg 4W^2$; the resulting approximate solution to Eq. 33 is given by

$$X \simeq -\phi_o(1 + \alpha\Omega_i/4\nu_{ii}) \qquad (34a)$$

which indicates that $f_1 \simeq -\omega_D X/2\pi$ is proportional to $V_E = \omega_D\phi_o$ in the plasma and increases linearly with $\Omega_i \propto B_o$, in accord with the data shown in Fig. 38a. For the same conditions as in Eq. 34a, the corresponding solution for $\gamma = \omega_D Y$ is given in the approximate form

$$\gamma \simeq V_{Ti}^2\phi_o/2\Omega_i r_o^2 + (a_i/r_o)^2\nu_{ii}/2 \qquad (34b)$$

which shows that the value of γ decreases with both increasing B_o and decreasing values of ϕ_o; γ also decreases as n_o decreases, but the effect is small unless ϕ_o is sufficiently small. These results are in accord with the physical explanation for the onset of the time-growth in the m=1 mode that is discussed earlier.

Using the data in Fig. 38a for -X, the corresponding γ are calculated from the full Eq. 30 and plotted in Fig. 39 as a

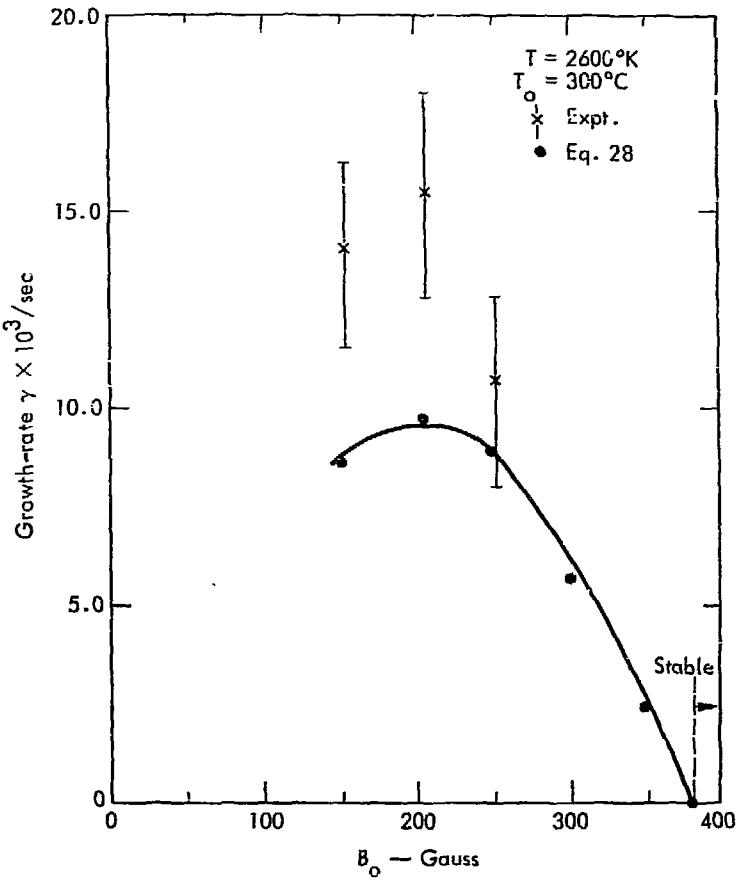

Fig. 39. Comparison between the calculated and measured growth-rates as a function of B_o for the corresponding values of -X in Fig. 38a; the theory of Eq. 30 predicts the B_o for the maximum γ and the variation of γ with B_o.

function of B_o; measured data for γ are evaluated from measurements of the linear time-growth for the m=1 mode amplitude. Comparison of the two results indicates that the theoretical curve shows the same type of functional dependence on B_o as the measured data; both results show a maximum γ at $B_o \approx 200$ G, but the theory predicts instability for B_o between 300 and 400 G, while the data shows stability.

A final comparison between the theory of Chu et al. and the present data involves the phase relation between $\tilde{n}$ and $\tilde{\phi}$ of the waves. Using their[63] Eq. 11 with $y = X + iY$ and separating the real and imaginary components, the phase angle ψ between $\tilde{n}$ and $\tilde{\phi}$ is given by

$$\mathrm{Tan}(\psi) = (\bar{\Sigma} - (Y + \bar{\Sigma})/X)(1 + (Y + \bar{\Sigma})/X)^{-1} \qquad (35)$$

In the present work, the relation $|X| >> |Y + \bar{\Sigma}|$ is satisfied so that to a good approximation, $\mathrm{Tan}(\psi) \approx \bar{\Sigma}$; since $\bar{\Sigma}$ is typically between 0.15 and 0.3 for B_o between 150 and 300 G, ψ is predicted to be between 9 and 10°, in close accord with the $\psi \approx 20°$ which is estimated from Fig. 24.

The results presented in the last several paragraphs show that the theoretical dispersion equation that is based upon a plasma model with a uniform rotation in a uniform magnetic field provides useful quantitative and qualitative information about the present experiment that consists of a non-uniform plasma rotation in a mirror magnetic field. In particular, Eq. 26 provides qualitative explanations for 1) the observed dependence of the periodic time-growth in the m=1 mode amplitude upon the physical parameters n_o, B_o, and $\phi_o \propto V_{oi}$, 2) the existence of two forms for the m=1

mode in the plasma, and 3) the observed linear increase of f_1 with increasing B_o. Furthermore, Eq. 26 predicts numerical values for the stability thresholds, frequency, and growth-rate that are much closer to the measured data than is likely to be expected on the basis of physical reasoning. Considering the assumptions and approximations inherent in the application of the Eq. 26 dispersion relation to the present experiment, the close numerical agreement between the theory and the data is either fortuitous or indicates a hidden correspondence between the two systems which is not physically apparent. The full answer to this problem involves a non-linear stability analysis of both systems and is presently beyond the state of mathematical development in theoretical plasma physics.

V. MEASUREMENTS OF ANOMALOUS PLASMA LOSSES

The previous chapter dealt with the mode identification of the unstable plasma waves, while the present chapter is concerned with the correlation between these unstable oscillations and the appearance of large periodic radial plasma losses from the column. The equilibrium plasma measurements in Chapter III indicate that the time-average plasma losses are due primarily to the combination of the purely classical losses from resistive diffusion and ion recombination at the hotplates, but such processes are entirely inadequate to account for the periodic loss of more than half of the total column density. The origin of such losses is the subject to be studied in the following paragraphs.

If the anomalous losses are correlated with the m=1 waves, the plasma detected at the column exterior should sharply decrease when the waves are stabilized to a saturated amplitude in the column interior. Figure 40 shows the effect of decreasing the plasma column rotation on both the time-growth of the waves and the plasma detected outside the column. At $U_o \simeq 0V$, the density spikes detected at $r \simeq 8$ cm ($a \simeq 5$ cm) are strongly correlated with the total density oscillations at $r \simeq 4$ cm; however, for $U_o \simeq -50$ V, both the time-growth of the waves and the density at the column edge have all but vanished. Therefore, not only are the unstable waves excited by the centrifugal forces in the column, but the plasma losses are directly correlated to the presence of time-growth in the m=1 mode amplitude.

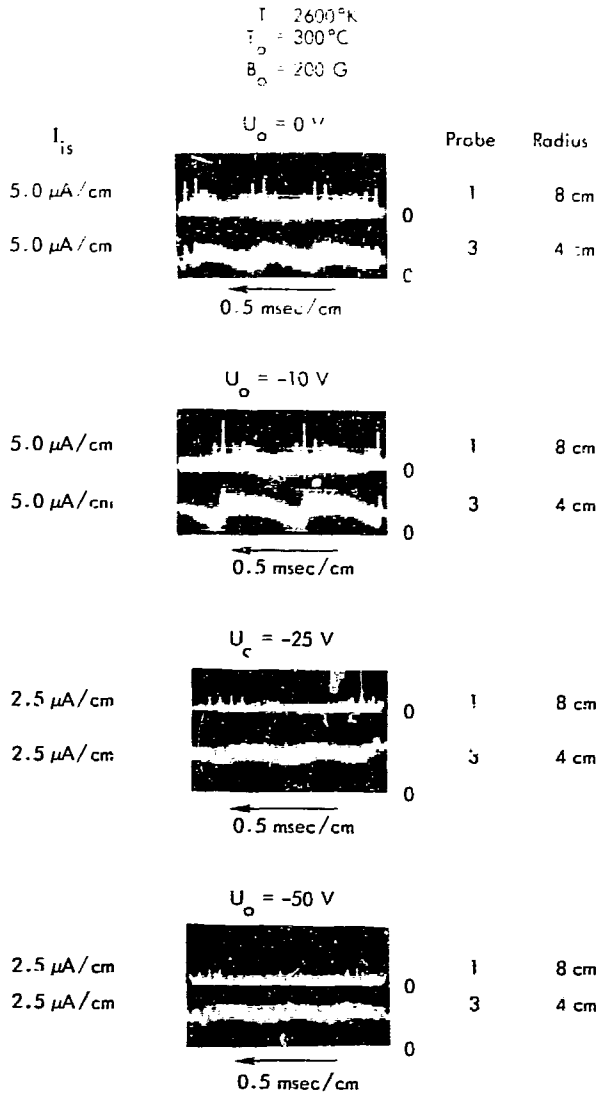

Fig. 40. Measured correlation between the periodic time-growth of the m=1 mode amplitude and the periodic losses at the column edge as a function of $U_o < 0$ at $B_o \simeq 200$ G, $T \simeq 2600°K$, and $T_o = 300°C$; the results show that the wave time-growth and radial losses decline as the column rotation decreases.

Figure 40 also shows that the period of the total density fluctuation decreases as the column rotation is reduced until it eventually vanishes near $U_o \simeq -50$ V. One possible explanation for the period decrease is that reducing the column rotation correspondingly reduces the wave growth-rate; for a constant plasma fill-rate, the waves are less effective in convecting the plasma from the column, and it therefore takes a longer time for the waves to produce sufficient plasma loss to lower the total column density. By the same type of reasoning, an increased plasma fill-rate coupled with a constant wave growth-rate in the column should produce a corresponding decrease in the total density fluctuation period.

Figure 41 shows the change in the total density fluctuation period for T held constant at 2600°K and T_o varied between 200°C and 400°C at the oven. For $T_o \simeq 200$°C, the m=1 mode time-growth is absent or sufficiently small to prevent measurable amplitude growth. For T_o near 250°C, the onset of the mode time-growth occurs, and the total density fluctuation period decreases by 50% as T_o increases from 250°C to 400°C. The mode time-growth may be absent at $T_o \simeq 200$°C because the plasma waves are sufficiently weak to be shorted by the electron-rich hotplate sheath before they attain measurable amplitudes. Since the plasma fill-rate, $I_o/e \propto j_o(T_o)$, increases rapidly with T_o, the decrease in the total density fluctuation period in Fig. 41 is probably due to an increase in the plasma fill-rate to the column.

A similar decrease in the total density fluctuation period is also observed when T is varied. Figure 42 shows the results

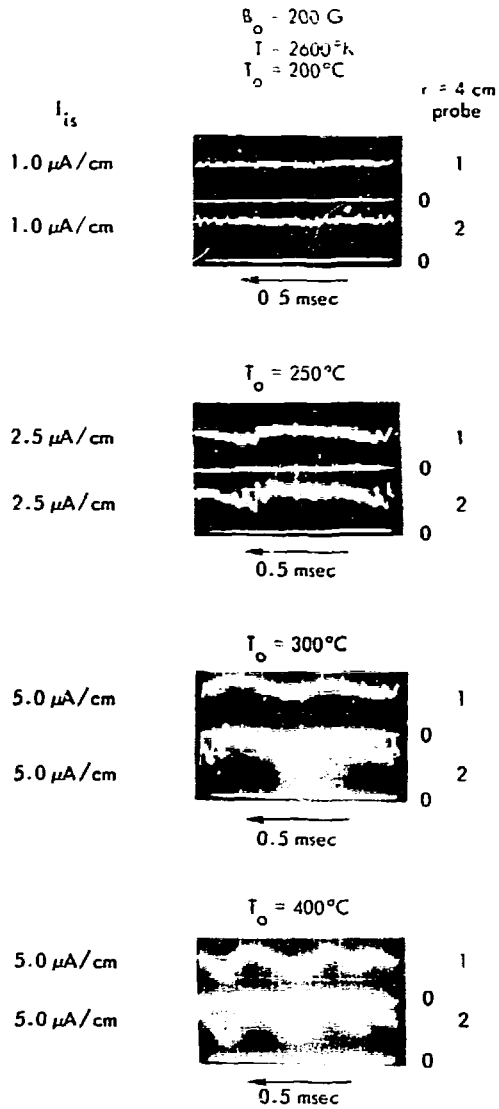

Fig. 41. Study of the onset of the periodic time-growth of the m=1 mode amplitude as a function of T_o at B_o = 200 G and T = 2600°K; the period change is related to increased plasma fill-rates for increases in T_o.

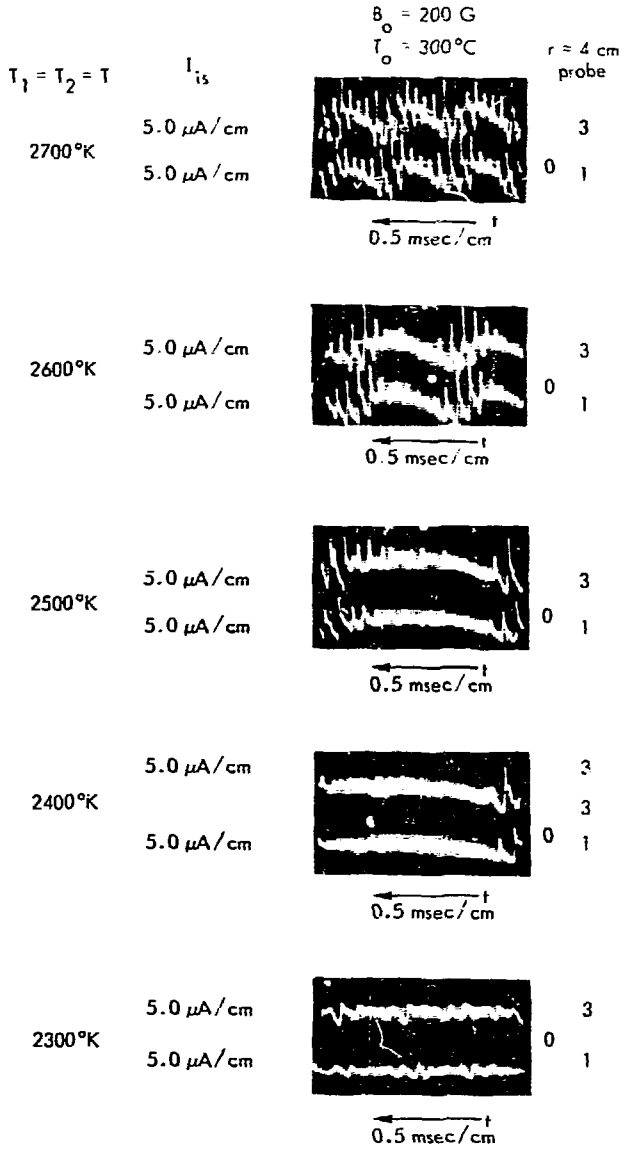

Fig. 42. Study of the onset and period change for the periodic time-growth of the m=1 mode amplitude with increases in T and $B_o \approx 200$ G, $T_o \approx 300°C$, and the probe at r = 4 cm; the period decrease with increasing T is caused by a reduction in the radial losses from the plasma.

when T_o is held constant at 300°C and T varied between 2300°K to 2700°K. The onset of the m=1 mode time-growth occurs close to the temperature where the hotplate sheath becomes electron-rich. Increasing T from 2500°K to 2700°K causes a 3:1 decrease in the total density fluctuation period in Fig. 42, and the rate of total density increase at the center of the fluctuation period increases with T. Since the plasma fill-rate I_o/e is nearly independent of T for a change of only 200°K, the increase in the rate of the total density build-up indicates that the radial plasma losses decrease with increasing values of T.

There are at least two possible ways that the radial plasma losses could decrease as T increases. The first method involves the possible radial redistribution of the plasma in the column so that there is less plasma density in the region of the maximum wave amplitude at the column edge. The second method involves the possible increase in the ion-confining electric field at the column edge.

Comparisons between the radial density profiles recorded at $B_o \simeq 200$ G for $T \simeq 2500$ to 2700°K indicate that the density increases in the column center as T increases, but there is little indication of any significant density reduction at the column edge. Therefore, it is improbable that the radial plasma losses are significantly reduced by plasma redistribution in the column.

An increase in the value of $-E_{ro}$ at the column edge with increasing T appears plausible because the potential difference between the interior and exterior of the plasma column increases with T. In addition, some measurements indicate that the plasma

rotation may increase with T, in accord with an $\underline{E}x\underline{B}$ origin of the plasma rotation. Therefore, the probable explanation for the total density fluctuation period decrease in Fig. 42 is that independently of the wave growth-rate, the radial electric field at the plasma edge increases with T and reduces the radial plasma losses from the column. In the presence of a constant plasma fill-rate, the rate of the total density build-up increases, and the plasma losses increase rapidly, resulting in a decrease in the period between the maximum plasma losses.

The results in Fig. 40 show that the density spikes at the column edge are strongly correlated with the time-growth of the m=1 mode amplitude, and $\underline{E}x\underline{B}$ radial convection by the unstable waves is the most probable cause for the observed plasma losses. However, the convective losses can only lead to wave saturation at an amplitude where the total plasma losses are balanced by the plasma input to the column. Therefore, the large observed decrease in the column density can only be caused by some type of nonlinear plasma loss.

One possible nonlinear mechanism that could explain the large plasma losses indicated in Fig. 40 is described as follows. The $\underline{E}x\underline{B}$ radial convection transports negatively charged plasma from the column interior into the region of the ion-rich sheaths at the cold endplates. The endplate sheaths require a finite time in which to charge the plasma positively in accord with the ion-rich sheaths. If the characteristic radial transport time $\tau_{\perp}$ from the convection is small in comparison with the charge compensation time $\tau_{\parallel}$, the ion potential well at the column edge

may be sufficiently weakened to produce a large radial plasma loss.

In the present experiment, $\tau_\perp$ is approximated by the time required to convect the plasma across the width of the high-velocity annulus; for $B_o = 150$ G, the result is $\tau_\perp \simeq 0.2$ msec, based upon $\underline{E}\times\underline{B}$ flux measurements and results from Chapter III. An estimate of the magnitude of $\tau_\parallel$ is obtained as follows. For curl $(B_o) = 0$, the sum of the conduction and displacement currents is zero. Using Eq. 5 to calculate the potentials, the current flow in the sheath adjustment is well approximated by j_{er} flowing into the cold endplates: j_{er} is the thermal electron current defined in Chapter II. Since $\omega < \Omega_i$ in the present work, a fully ionized plasma exhibits an effective dielectric constant (normal to B_o) of $\epsilon_\perp \simeq 1 + (a_i/\lambda_D)^2 >> 1$ which leads to a radial displacement current $\epsilon_o \epsilon_\perp (\partial E_{ro}/\partial t)$ with $\epsilon_o \simeq 8.85 \times 10^{-14}$ farads/cm; the axial displacement current is neglected at the column midplane. Using the above results, the estimated time for the current flow j_{er} into the cold endplates to restore the ion potential well is given by $\tau_\parallel \simeq \epsilon_o (L/\delta)(a_i/\lambda_D)^2 (E_{ro}/j_{er})$; at $B_o = 150$ G, $L/\delta \simeq 25$, $a_i/\lambda_D \simeq 10^3$, and $j_{er} \simeq 0.012$ a/cm^2 for $n_o = 2 \times 10^{10}$/cm^3 so that $\tau_\parallel \simeq 0.2$ msec, which is comparable to $\tau_\perp$. Therefore, based on the above simple arguments, some reduction in $-E_{ro}$ is possible within a time period less than 0.5 msec, in qualitative agreement with the observed plasma loss period. Other nonlinear effect such as large-scale eccentric rotation of the plasma column may also contribute to the losses.

Due to nonlinear effects such as those just considered, detailed study of the plasma loss dynamics must be experimental. The radial losses are studied with a series of spacial distributions of the total density and the perturbed $\underline{E}x\underline{B}$ plasma flow at the four selected times that are indicated on the density trace in Fig. 43. At $t = t_1$, the m=1 mode propagates at a low-level saturated amplitude, the total column density is linearly increasing, and the losses are due to resistive diffusion. At $t = t_2$, both the m=1 mode amplitude and the total column density are linearly increasing, and the radial losses are still determined mainly by resistive diffusion. At $t = t_3$, the mode amplitude has saturated in the nonlinear regime, the total column density is nearly a maximum, and the radial losses are greater than those from resistive diffusion. At $t = t_4$, the mode amplitude is decreasing while the total column density is again increasing, and the radial losses have subsided to a level comparable to resistive diffusion.

For each of the four times shown in Fig. 43, the spacial density distribution is computed within an individual cycle of the m=1 mode plasma oscillation. Using radial and azimuthal density correlations, the density at about forty individual spacial positions within a 16 cm-diam cross section is plotted, and approximate constant-density contours drawn as shown in the series of Fig. 44.

Figure 44a shows the constant-density contours at $t = t_1$. The m=1 perturbation is present as an eccentrically rotating density maximum of approximately $8.0 \times 10^{10}/cm^3$ near r = 5 cm in the column. Most of the contours appear to close within the column cross section shown and indicate that at $t = t_1$, the outer

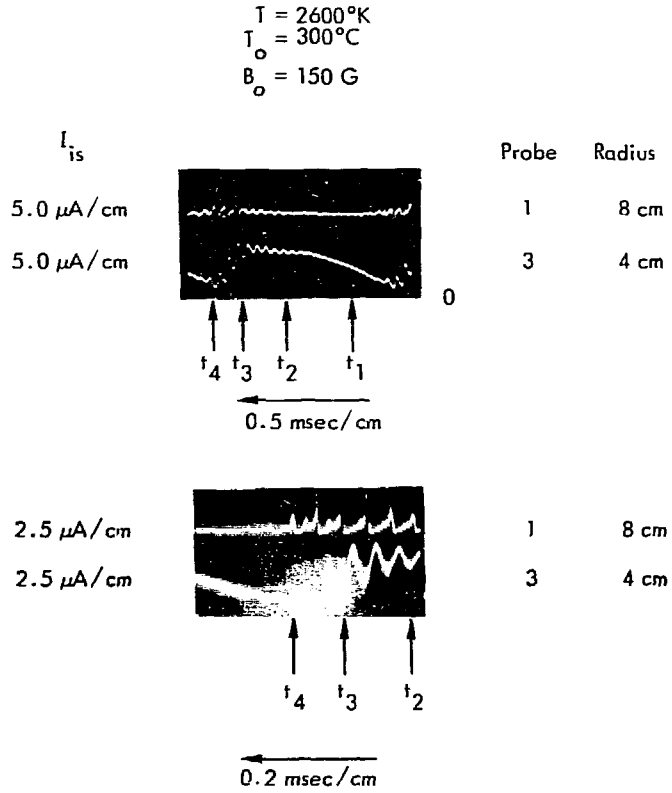

Fig. 43. Position of the four times used in the non-linear plasma studies in relation to the period of the column density fluctuation.

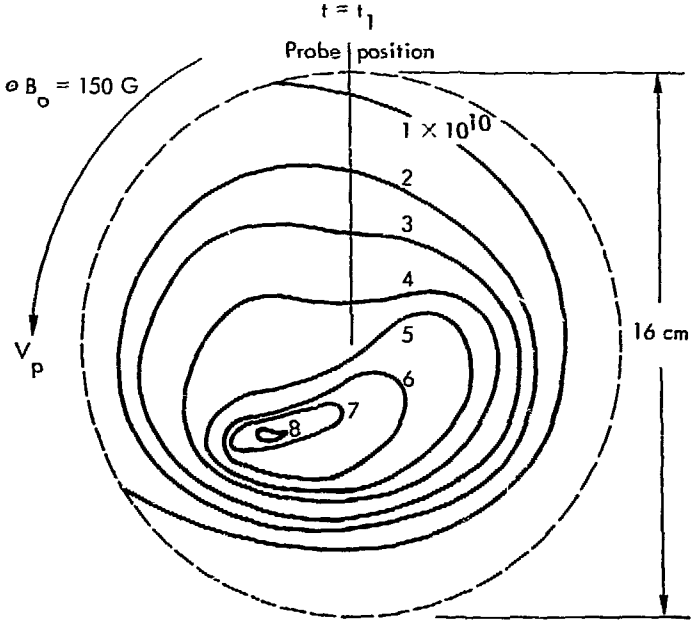

Fig. 44a. Constant-density contours in the column mid-plane cross section for $B_0 = 150$ G and $t = t_1$ in Fig. 43; most of the plasma remains confined to the column.

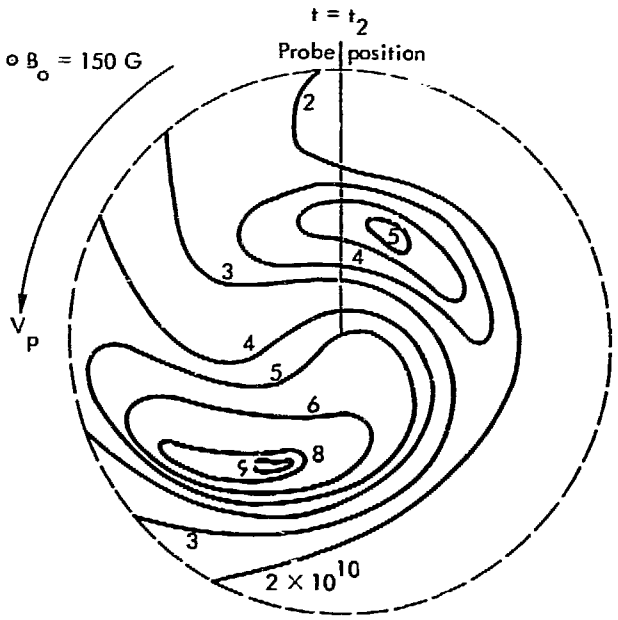

Fig. 44b. Constant-density contours in the column midplane cross section for B_o = 150 G and $t = t_2$ in Fig. 43; radial plasma drift out of the column is apparent.

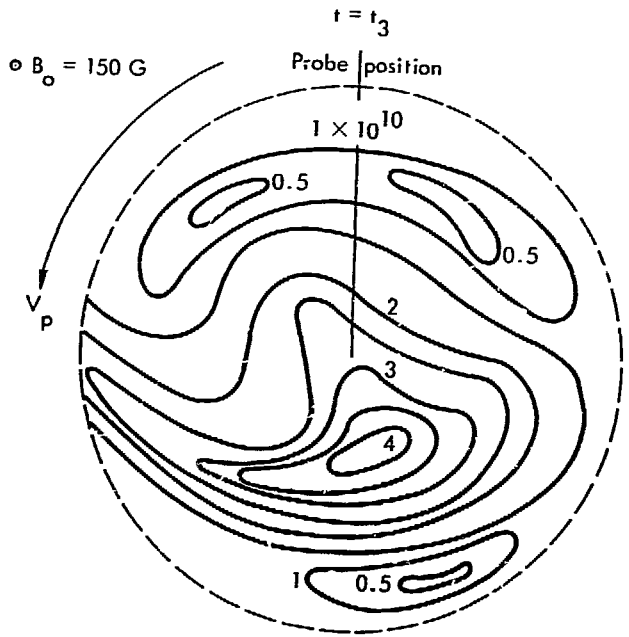

Fig. 44c. Constant-density contours in the column midplane cross section for B_o = 150 G and $t = t_3$ in Fig. 43; the m=1 wave amplitude is large and considerable $\underline{E}x\underline{B}$ radial plasma convection is shown.

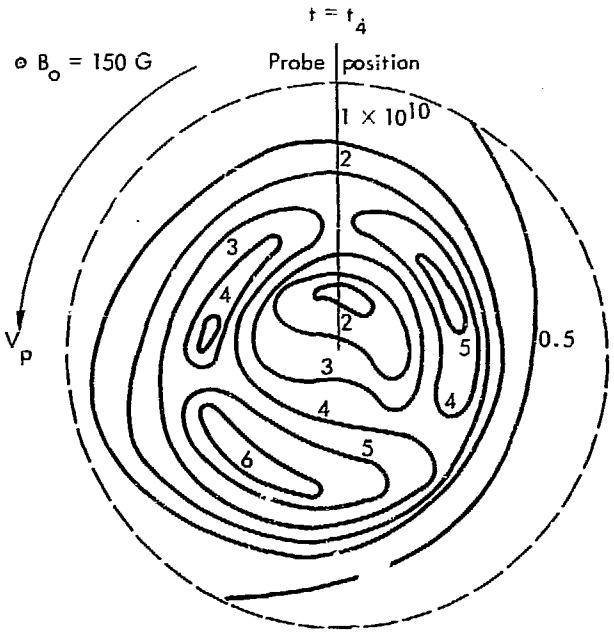

Fig. 44d. Constant-density contours in the column midplane cross section for B_o = 150 G and $t = t_4$ in Fig. 43; the greatest plasma loss has occurred and the column density is increasing.

region of the plasma is lagging spacially behind the inner region of the column. Plasma density also appears to be collecting at the leading edge of the perturbation as the contours are closely spaced, and there appears to be only the beginning of a possible radial drift out of the column.

Figure 44b shows the constant-density contours calculated for the time $t \simeq t_2$ in Fig. 43. The primary density maximum has now increased to approximately $9.0 \times 10^{10}/cm^3$ and is accompanied by a weaker maximum density of $5.0 \times 10^{10}/cm^3$ that is 180° out of phase in the spacial distribution. The two maxima could indicate the possible formation of an m=2 mode in the column. Fewer density contours are closed than at $t \simeq t_1$, and the contours show the early stages of a pronounced radial plasma drift across B_o. The outer region of the plasma is still lagging in space behind the inner plasma region as before.

Figure 44c shows the constant-density contours for the time $t \simeq 1\ t_3$ in Fig. 43 when the greatest decrease in the column density occurs. The contours show a large radial drift of plasma across B_o and out of the column. The plasma drift appears as a long curved "tongue" that trails out of the column as it rotates. At the time $t \simeq t_3$, the "tongue" has convected over one-half of the total plasma density out of the column interior. Due to the fact that the constant-density contours shown are actually an artistic smoothing based upon a rough grid of measured points, the internal structure of the column can only be qualitative in nature, and the subsidiary maxima in Fig. 44a may or may not be real. However, the gross features indicating the

column density has decreased and a large radial drift of plasma is present are in accord with other measurements and physical predictions. The contours are a convenient way of graphically illustrating the plasma convection.

Figure 44d presents the approximate constant-density contours at $t \simeq t_4$ in Fig. 43 and show that the large radial plasma drift has largely subsided. The internal column structure shown is only an estimate of the real contours, but the total density appears to have increased, and the m=1 plasma perturbation is less pronounced that at $t \simeq t_3$. The contours show a much more symmetric plasma density distribution than at the peak of the radial plasma loss.

An estimate of the spacial distribution of the perturbed $\underline{E}x\underline{B}$ drift contours in the column is provided by calculations of the constant-potential contours. Since $\tilde{E} \simeq -\nabla\tilde{\phi}$, the electric field contours are everywhere normal to the equi-potential lines in the column. Using the relation $\underline{\tilde{V}}_E \simeq -\underline{\nabla}\tilde{\phi} \times \underline{B}_o/B_o^2$, the lines of perturbed flow are tangent to the equi-potential lines in the column, and the velocity flow pattern in the column can be studied from a plot of the lines of constant $\tilde{\phi}$.

The series in Fig. 45 shows the perturbed $\underline{E}x\underline{B}$ velocity flow spacial distribution for each of the four times indicated in Fig. 43. The equi-potential lines are based upon a grid of approximately thirty calculated values of $\tilde{\phi}$ using radial and azimuthal correlation data at B_o = 150 G. The lines shown are estimates and are only meant to present a qualitative pattern of the perturbed plasma flow in the cross section shown. Figure 45a

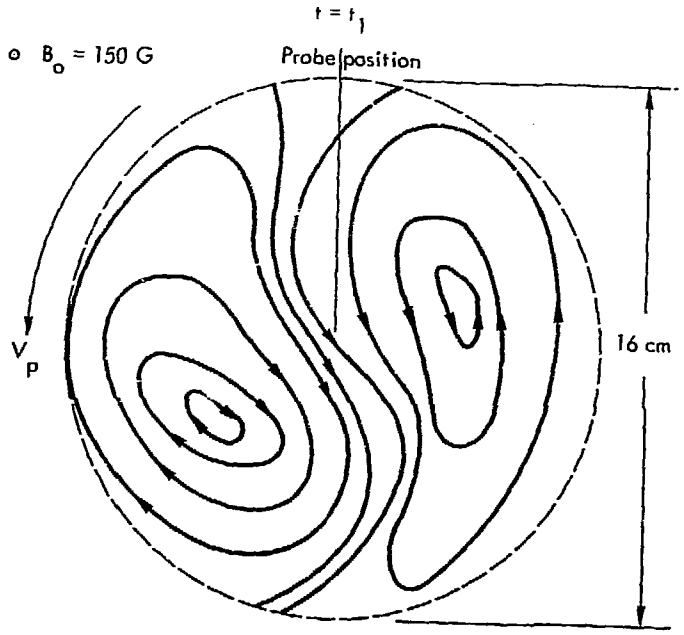

Fig. 45a. Perturbed $\underline{E}x\underline{B}$ velocity flow contours corresponding to the data in Fig. 44*a*; the plasma circulates within the column cross section and indicates only small radial flow.

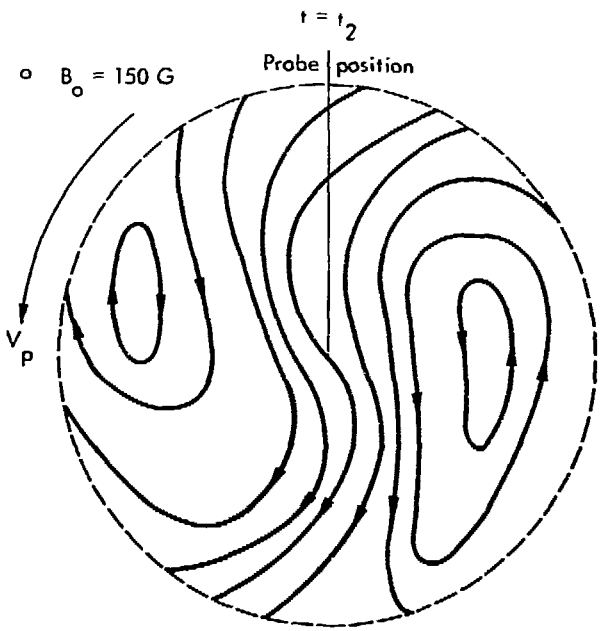

Fig. 45b. Perturbed ExB velocity contours corresponding to the data in Fig. 44b; increased radial flow out of the column occurs near increased density regions.

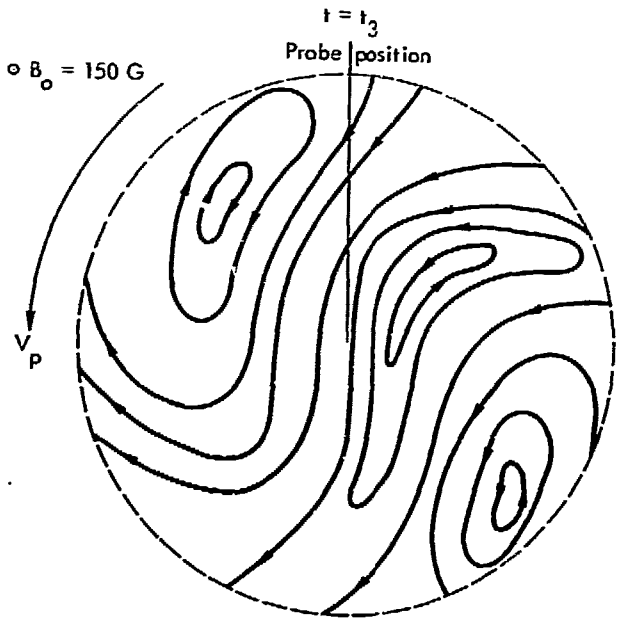

Fig. 45c. Perturbed ExB velocity flow contours corresponding to the data in Fig. 44c; the regions of large radial flow coincide with those where large radial plasma drift occurs.

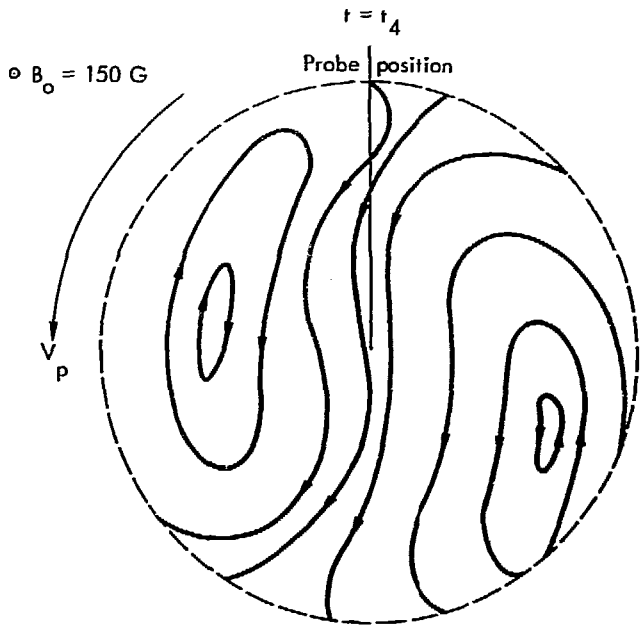

Fig. 45d. Perturbed ExB velocity flow contours corresponding to the data in Fig. 44d; the plasma is circulating primarily within the column cross section and indicates only small radial flow.

shows the velocity flow pattern at $t \simeq t_1$; the constant potential lines do not show the flow speed. The plasma appears to be circulating within the cross section, and little radial drift out of the column is present. Comparing the spacial pattern of Fig. 44a with that in Fig. 45a, the plasma appears to be confined within the cross section shown.

Figure 45b shows the spacial distribution of $\tilde{V}_E$ at $t \simeq t_2$. Fewer of the flow lines are closed within the cross section, and the plasma appears to be flowing in at the top right and flowing out of the column at the lower left of the figure. Comparing with the corresponding density distribution in Fig. 44b, the plasma is drifting radially out the column and is probably lost.

Figure 45c shows the contours of $\tilde{V}_E$ for the time $t \simeq t_3$ in Fig. 43. The flow pattern has shifted clockwise with respect to the pattern at $t \simeq t_2$, and the maximum radial drift occurs in the same region as the greatest density loss, indicated in Fig. 44c. The plasma appears to flow into the column from the right side of Fig. 45c and flow out at the left. Since the outward flux exceeds the inward flux in Fig. 44c, there is a large loss of plasma from the column, in accord with the measured losses at the column edge.

At $t \simeq t_4$ in Fig. 43, the $\tilde{V}_E$ flow pattern is shown in Fig. 45d. The flow pattern has shifted counter-clockwise to nearly the same spacial position as that shown in Fig. 45a, and the enhanced radial velocity flow of the perturbed plasma from the column has greatly subsided in comparison with that shown in

Fig. 45c. Most of the perturbed plasma appears to again be circulating about the column cross section.

The data represented in the series of spacial distributions shown in Figs. 44 and 45 present a comprehensive qualitative picture of both the spacial and temporal development of the $\underline{E}x\underline{B}$ plasma convection that is caused by the unstable m=1 waves in the column. In the absence of significant wave amplitude such as at $t = t_1$ in Fig. 43, most of the perturbed plasma appears to circulate about the column with little net radial loss; however, when there is significant wave amplitude, a large radial drift of plasma occurs that momentarily is sufficient to lower the total density in the column. Therefore, the outward radial flux is related to the total column density by the global equation of continuity that is written in the form

$$\partial\tilde{N}/\partial t + 2\pi rL\int_o^{2\pi} F_E(\theta)d\theta = \langle S\rangle \simeq I_o/e - 2\pi rLF_c - \pi r^2 L\partial F_r/\partial z - \partial N/\partial t \qquad (36)$$

where

$$\tilde{N} = 2\pi\int_o^r\int_o^L \tilde{n}(r,z)rdrdz$$

represents the total number of perturbed plasma particles within a column of radius r, $F_E = \tilde{n}(\theta)\tilde{u}_r(\theta)$ with $\tilde{u}_r = \tilde{E}_\theta/B_o$ defines the

local $\tilde{E}x\underline{B}_o$ radial flux, $\langle S \rangle = 0$ is the equilibrium continuity equation in the absence of the waves, and the remaining parameters are defined in Chapter III. At equilibrium, $\langle S \rangle$ is theoretically zero, and the data in Chapter III verify this to within a factor-of-two in Fig. 14b at $r \simeq a$. Therefore in Eq. 36, $\langle S \rangle = 0$ for the calculations to follow.

A numerical evaluation of Eq. 36 is made with data at $r = a$ and $B_o \simeq 150$ G which corresponds with that shown in Figs. 44 and 45. At each of the four times indicated in Fig. 43, $F_E(\theta)$ is computed from correlation data between $\tilde{n}$ and $\tilde{\phi}$ for the m=1 mode. The results are plotted in Fig. 46 as a function of θ in each case. The shape of $F_E(\theta)$ is roughly sinusoidal when the mode amplitude is small; as the amplitude increases, $F_E(\theta)$ is seen to become more peaked in angle, in accord with the data shown in Figs. 44c and 45c.

The important quantity in the evaluation of Eq. 36 is the net radial flux through the column perimeter. Integrating the results in Fig. 46 over a full period of θ at each of the four times leads to the results shown in Fig. 47. The net radial losses are seen to increase from below the equivalent classical diffusion flux at $t = t_2$ to nearly the level predicted by the so-called "Bohm" diffusion flux $F_B \simeq -(KT/16eB_o)(\partial n_o/\partial r)$ at $t = t_3$, and then decrease to the value shown at $t = t_4$. The Bohm diffusion[38] is often quoted in the literature as a convenient measure of the anomalous plasma losses and is used here as a convenient standard.

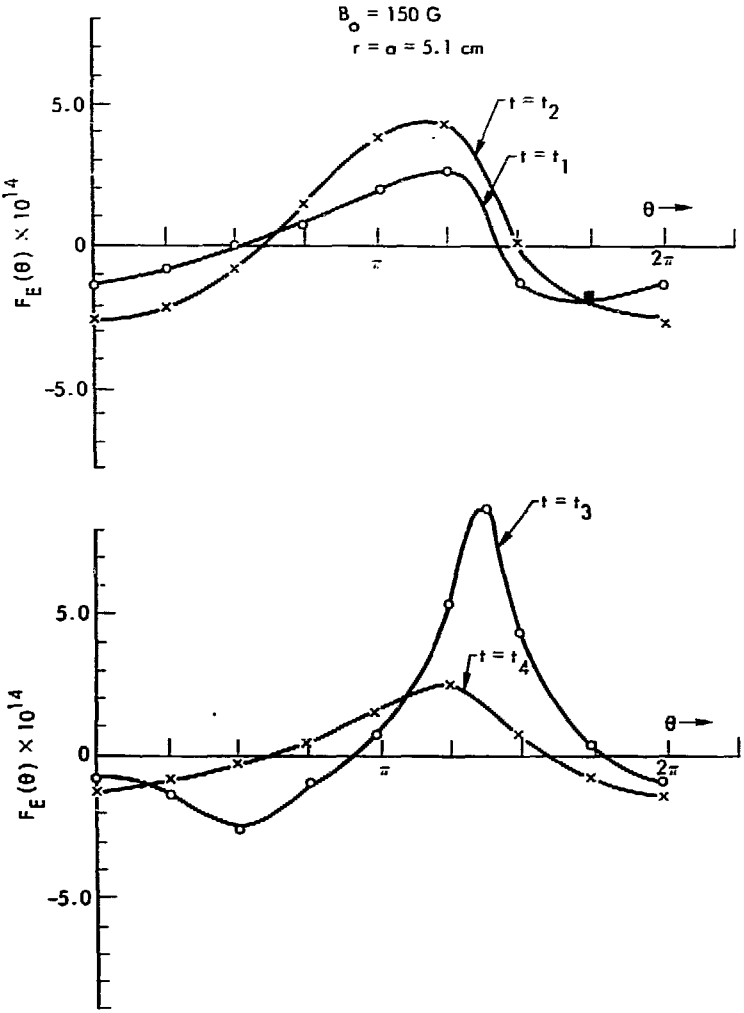

Fig. 46. Azimuthal distribution of the calculated ExB radial wave convection for each of the four times in Fig. 43; the loss flux is nearly sinusoidal in θ for $t = t_1$ and t_4, while for $t = t_3$, the loss flux is sharply peaked in amplitude.

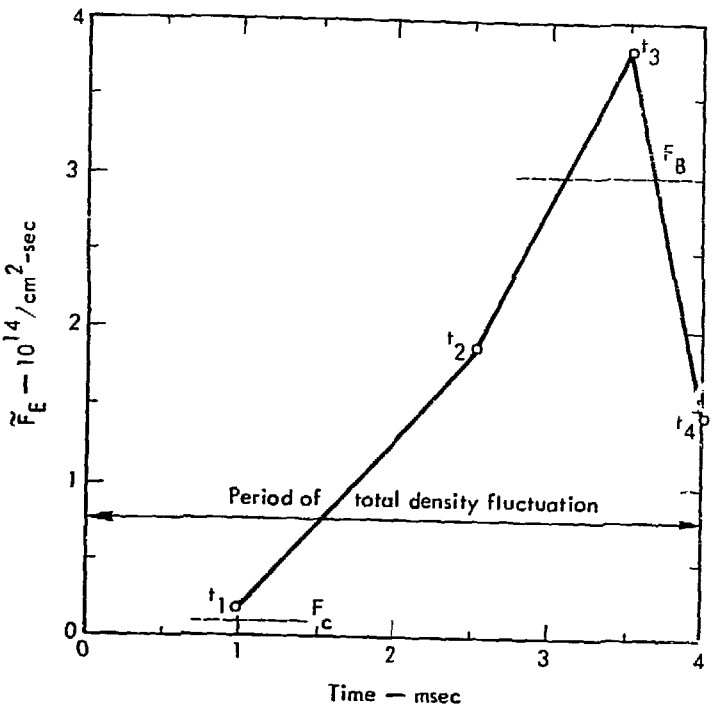

Fig. 47. Calculated net radial loss flux for each of the four times indicated in Fig. 43; for $t = t_1$, the net radial loss flux is comparable to the classical diffusion flux F_C, while for $t = t_3$, the net loss flux is comparable to the "Bohm" diffusion flux F_B.

In order to numerically evaluate Eq. 36, some estimate is necessary for the term $\partial\tilde{N}/\partial t$. Figure 27 shows that $\tilde{n}(r)$ is closely approximated by the Bessel function $\tilde{n}(r) = \tilde{n}_m J_1(k_r r)$. If a further assumption is made that a radial distribution of $\partial\tilde{n}/\partial t$ is similar to that for n(r), then $\partial\tilde{N}/\partial t$ can be calculated, and Eq. 36 reduces to

$$\partial\tilde{n}_m/\partial t = \left[- k_r a / a J_o(k_r a)\right] \int_0^{2\pi} F_E(\theta) d\theta \qquad (37)$$

which indicates that the perturbed density decreases with time for a net outward plasma flux from the column. For B_o = 150 G, $k_r a = 2.0$ and $J_o(2.0) \approx 0.22$ so that $\partial n_m/\partial t = -1.8\tilde{F}_E$ where $\tilde{F}_E$ is the net outward flux throughout the column surface.

Using the data in Fig. 46 to evaluate $\tilde{F}_E$ from the column, the predicted value of $\partial\tilde{n}_m/\partial t$ at each of the times is plotted in Fig. 48 and compared with the measured data at B_o = 150 G and r = 4 cm (position of the maximum, $\tilde{n}_m$, in the column). Considering the nature of the measurements and the probable errors in the measurements of the $\partial\tilde{n}_m/\partial t$ in the column, the agreement between Eq. 37 and the data is better than expected and clearly shows that plasma is being convected out of the column by the unstable m=1, large amplitude waves.

The results presented in this chapter point to the origin of the anomalous radial losses from the plasma column in the time-growth of the unstable m=1 mode that was shown in the last chapter to be caused by the centrifugally-driven gravitational interchange instability. The unstable mode creates

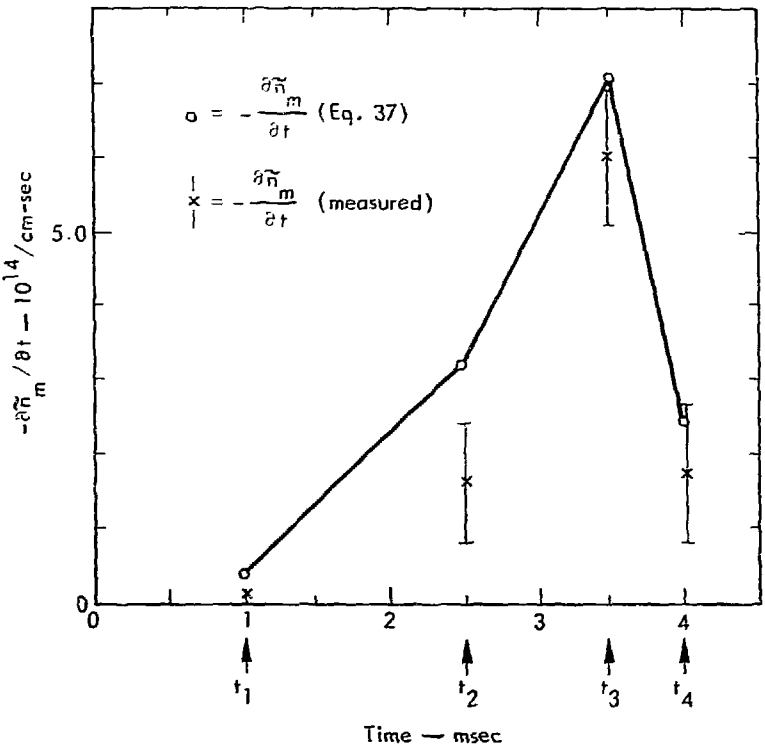

Fig. 48. Comparison between the measured and calculated perturbed density loss rate for the four times in Fig. 43; the calculated values are made with Eq. 37 and the measured data are determined from the slopes indicated in Fig. 43 at the specified times.

a periodically large $\underline{E}x\underline{B}$ plasma convection from the column and produces the total density fluctuation in the column density. The period of this fluctuation is shown to be dependent primarily on the balance between the magnitude of the radial losses and the plasma fill-rate to the column. The spacial and temporal development of the plasma loss is shown at B_o = 150 G and is in accord with numerical calculations of the density continuity at the column edge. The plasma losses are shown to originate in the column interior and appear as a net radial plasma flux out of the plasma column. Numerical calculations of the convective flux at the time of the greatest plasma loss are in accord with the so-called "Bohm" diffusion flux that has often been used to characterize the anomalous losses from a plasma.

VI. SUMMARY AND CONCLUSIONS

In Chapter III, data for ϕ_s shows that the hotplate sheaths are electron-rich, but the magnetic field lines for $r > a$ terminate on a cold surface with an ion-rich sheath. The resulting thermoelectric potential discontinuity produces a localized radial electric field that creates an $\underline{E}x\underline{B}$ rotating high-velocity annulus and confines the ions in the plasma column. Radial profiles of $-E_{ro}$ and V_{oi} in the column are in accord with predictions from an isothermal model of the plasma equilibrium that includes ion viscosity, electron resistivity, and rotational inertia effects. Through collisions with electrons, the ions are transported radially in sufficient numbers to account for resistive diffusion losses and to broaden the radial profile of n_o beyond that expected on the basis of thermal equilibrium. The total measured plasma losses are in accord with a combination of resistive diffusion and ion recombination at the hotplates and indicate that two different types of equilibrium can exist, depending on the value of B_o in the column.

For $B_o > 300$ G, the density n_o is nearly constant with time except for low-level waves. Measured wave parameters are presented in detail in Section B of Chapter IV and indicate that the waves are probably a form of the transverse Kelvin-Helmholtz instability from velocity shear at the edge of the high-velocity annulus. Comparisons of the predicted stability conditions, frequency, centrifugal force, and $\tilde{n}$-$\tilde{\phi}$ correlations in the "velocity jet" model of Perkins and Jassby with data shows good agreement for all the modes observed. The waves do not appear to

enhance the radial plasma losses significantly beyond those due to resistive diffusion.

When B_o is between 150 and 300 G, the total column density is observed to fluctuate between two levels in the general shape of a sawtooth wave with sinusoidal modulation. In the last section of Chapter IV, the data indicate recurrent time-growth in an azimuthally propagating m=1 mode whose marginal stability depends on both thresholds in n_o and V_{oi}. For a V_{oi} above the threshold, the m=1 mode amplitude shows a linear time-growth for $n_o > n_c$, but the amplitude decays to a low-level saturated form when $n_o < n_c$. Comparisons of the predicted stability threshold, frequency, growth-rate, and phase shift between $\tilde{n}$ and $\tilde{\phi}$ for the model of Chu et al. with data indicates that the m=1 mode is probably ion diamagnetic waves that are driven unstable by a combination of resistive and centrifugal effects in the column. The model dispersion relation is able to qualitatively account for the observed stability thresholds of n_o, B_o, and V_{oi} as well as the linear increase of frequency with B_o.

Data in Chapter V indicate that the origin of the periodic fluctuation of the total column density is primarily due to the $\underline{E}x\underline{B}$ radial convection by the unstable m=1 waves. However, qualitative arguments indicate that the bulk of the plasma loss is due to some nonlinear process such as the momentary weakening of the ion-confining $-E_{ro}$ by radial plasma transport. Studies of the nonlinear temporal and spacial distributions of density and perturbed velocity flow show the development of large radial loss-flux that is comparable in magnitude with the "Bohm"

diffusion flux in the column. Using the density continuity equation, predicted density loss-rates are in accord with experiment and the measured $\underline{E}\times\underline{B}$ flux from the column.

The measurements in the present experiment provide substantial evidence to support the following conclusions:

1) The plasma equilibrium is determined primarily by the sheath conditions present both radially and axially. The hotplate sheaths determine the radial density profile in conjunction with the thermoelectric potential discontinuity at the hotplate edge; the ion potential well formed also determines both the steady plasma loss and the $\underline{E}\times\underline{B}$ column rotation.

2) The radially localized electric field at the column edge produces sufficient transverse velocity shear to cause a Kelvin-Helmholtz that appears to be the source of the group I modes in the column and does not lead to anomalous radial plasma losses.

3) The radially localized electric field at the column edge also produces sufficient centrifugal force to create a rotational instability in the lowest-order mode of the ion diamagnetic drift waves. In conjunction with the electron resistivity, the centrifugal instability is believed to provide the origin of the time-growth for the m=1 mode in the experiment; the observed anomalous radial plasma loss which accompanies the instability is then in accord with the $\underline{E}\times\underline{B}$ convection of plasma by the unstable mode.

4) The periodic nature of both the anomalous plasma loss and the total column density is due to a combination of nonlinear processes such as the possible flux weakening of the ion-confining

E_{ro} and the mode self-suppression as the column density decreases below a critical threshold; in the absence of the $\underline{E}x\underline{B}$ losses from the m=1 mode instability, the total column density increases to repeat the cycle.

ACKNOWLEDGMENTS

I wish to express my thanks to Charles Hartman for providing support during the performance of this work, to Professor Wulf Kunkel for several helpful discussions, and to Professor Charles Birdsall for suggesting the experimental method of controlling the radial-electric field. I also wish to express my thanks to Nathan Lindgren for advice and criticism in the early stages of this work.

This work was performed under the auspices of the U.S. Atomic Energy Commission.

REFERENCES

1. L. Spitzer Jr., Phys. Fluids 3, 659 (1960).
2. L. I. Rudakov and R. Z. Sagdeev, Sov. Phys. Dokl. 6, 415 (1961).
3. W. E. Drummond and M. N. Rosenbluth, Phys. Fluids 5, 1507 (1962).
4. F. F. Chen, Phys. Fluids 8, 912 (1965).
5. T. H. Dupree, Phys. Fluids 10, 1049 (1967); Phys. Fluids 11, 2650 (1968).
6. S. Yoshikawa and D. J. Rose, Phys. Fluids 5, 334 (1962).
7. F. Boeschoten, Phys. Fluids 6, 339, (1964).
8. D. L. Morse, Phys. Fluids 8, 516, 1339 (1965).
9. N. D'Angelo and S. von Goeler, Nucl. Fusion 5, 279 (1965).
10. K. I. Thomassen, Phys. Fluids 9, 1836 (1966).
11. J. H. Noon, H. A. Schmidt, and E. H. Holt, Plasma Phys. 12, 477 (1970).
12. K. C. Rogers, N. S. Wolf, C. Courville, and R. Motz, in Proc. of Conf. on Physics of Quiescent Plasmas (Frascatti, Italy 1967) Pt. 1, p. 259.
13. S. von Goeler and R. Motely, in Proc. of Conf. on Physics of Quiescent Plasmas (Frascatti, Italy, 1967), Pt. 1, p. 243.
14. J. A. Decker, P. J. Freyheit, W. D. McBee, and L. T. Shepard, Phys. Fluids 10, 2442 (1967).
15. H. W. Hendel, T. K. Chu, and P. A. Politzer, Phys. Fluids 11, 2426 (1968).

16. Y. Tanaka and M. Otsuka, J. Phys. Soc. Japan 24, 1146 (1968).

17. R. Aldridge and B. Keen, Plasma Phys. 12, 1 (1970).

18. M. Hashmi, A. J. Van Der Houven Van Oordt, and J. G. Wegrowe, Nucl. Fusion 10, 163 (1970).

19. W. Bernstein, Princeton Univ., Project Matterhorn, Technical Memoradom 108, Sept. 1960.

20. J. C. Woo and D. J. Rose, Phys. Fluids 10, 893 (1967).

21. N. Rynn and N. D'Angelo, Rev. Sci. Inst. 31, 1326, (1960).

22. N. D'Angelo and N. Rynn, Phys. Fluids 4, 275 (1961); Phys. Fluids 4, 1303 (1961).

23. R. C. Knechtli and J. Y. Wada, Phys. Rev. Lett. 6, 215 (1961).

24. N. D'Angelo and R. W. Motely, Phys. Fluids 5, 663 (1962); Phys. Fluids 6, 422 (1963).

25. J. A. Decker, J. Appl. Phys. 35, 497 (1964).

26. H. Lashinsky, Phys. Rev. Lett. 12, 121; 13, 47 (1964); Phys. Rev. Lett. 14, 1064 (1965).

27. N. Bucheinikova, Sov. Phys. JETP 19, 775 (1964); Sov. Phys.-Tech. Phys. 10, 53 (1965).

28. C. W. Hartman and R. H. Munger, Bull. Amer. Phys. Soc. 10, 213 (1965).

29. B. J. Eastlund, K. Josephey, R. F. Leheny, and T. C. Marshall, Phys. Fluids 9, 2400 (1966).

30. C. W. Hartman and R. H. Munger, in Proc. of Conf. on Physics of Quiescent Plasmas (Frascatti, Italy 1967), Pt. 1, p. 49.

31. T. K. Chu, H. W. Hendel, and P. A. Politzer, Phys. Rev. Lett. 19, 1110 (1967); Phys. Fluids 12, 203 (1969).

32. F. W. Perkins and D. L. Jassby, Phys. Fluids 14, 102 (1971).

33. J. Laframboise, Univ. of Toronto Institute for Aerospace Studies, Report. 100 (1966).

34. F. F. Chen, C. Etievant, and D. Mosher, Phys. Fluids 11, 811 (1968).

35. Handbook of Chemistry and Physics (Chemical Rubber Publishing Co., Cleveland, Ohio, 1970).

36. V.S. Formenko, Handbook of Thermionic Properties, G. V. Samsonev, Ed. (Plenum Press, N.Y. 1969).

37. S. von Goeler, Phys. Fluids 7, 463 (1964).

38. D. Bohm, Characteristic of Electrical Discharges in Magnetic Fields, A. Guthrie and R. K. Wakerling, Eds. (McGraw Publishing Co., 1949).

39. R. Bickerton and A. von Engel, Proc. Phys. Soc. 69, 468 (1954).

40. F. F. Chen, J. Nucl. Energy Part C 7, 47 (1966).

41. C. L. Brundin, Institute of Engr. Res., Univ. of Calif. Rept. AS-64-9 (1964).

42. E. Guilino, Phys. Fluids 13, 1855 (1970).

43. S. von Goeler and R. W. Motely, Phys. Fluids 10, 1360 (1967).

44. N. D'Angelo, D. Eckhartt, G. Grieger, E. Guilino, and M. Hashni, Phys. Rev. Lett. 11, 525 (1963).

45. N. D'Angelo and S. von Goeler, Nucl. Fusion 6, 135 (1966).

46. D. Eckhartt, G. Grieger, E. Guilino, and M. Hashni, Max-Planck-Institut Rept. MPI-PA-20 (1964).

47. S. von Goeler and R. W. Motely, in Proc. of Conf. on the Physics of Quiescent Plasmas (Frascatti, Italy 1967), pt. 1, p. 243.

48. G. Schmidt, Physics of High Temperature Plasmas, (Academic Press, New York, 1966).

49. T. E. Stringer, in Conf. on Plasma Physics and Controlled Fusion, (I. A. E. A., Vienna), vol. 1.

50. G. Grieger, Max-Planck-Institut Rept. MPI-PA 12/64; PA 15/64; PA 16/64.

51. F. F. Chen, Phys. Fluids 9, 2534 (1966).

52. N. Rynn, Phys. Fluids 9, 165 (1966).

53. L. Spitzer, Physics of Fully Ionized Gases, (Interscience Publishers Inc., New York, 1956).

54. S. Chandrasekhar, Hydrodynamic and Hydromagnetic Stability (Oxford Univ. Press, London, 1961), chap. I.

55. S. I. Braginskii, Reviews of Plasma Physics (Consultants Bureau, New York, 1965, vol. 1), chap. II.

56. M. Lapp and L. P. Harris, J. Appl. Phys. 34, 3622 (1968).

57. G. I. Kent, N. C. Jen, and F. F. Chen, Phys. Fluids 12, 2100 (1969).

58. M. N. Rosenbluth, N. A. Krall, and N. Rostoker, Nucl. Fusion Supp. 1, 243 (1962).

59. F. F. Chen, Phys. Fluids 8, 912 (1965).

60. N. A. Krall and T. K. Fowler, Phys. Fluids 10, 1526 (1967).

61. P. G. Drazin and L. N. Howard, Advances in Applied Mechanics, G. Kuerti, Ed. (Academic Press, N.Y., 1966), p. 1.

62. H. Lashinsky, Non-Linear Effects in Plasmas, G. Kalman and M. Felix, Eds. (Gorden and Breach Pub., N.Y., 1967), p. 451.

63. T. K. Chu, B. Coppi, H. W. Hendel, and F. W. Perkins, Phys. Fluids 12, 203 (1969)

64. F. F. Chen, Phys. Fluids 9, 965 (1966).

65. J. D. Jukes, Reports on the Progress in Physics (Phys. Soc. of London, 1967) pt. I, 30, 333; pt. II, 31, 305.

66. J. Backus, Characteristics of Electrical Discharges in Magnetic Fields, A. Guthrie and R. K. Wakerling, Eds. (McGraw Publishing Co., New York, 1949), chap. II.